Magnetoacoustic Tomography with Magnetic Induction for Electrical Conductivity based Tissue imaging

A DISSERTATION
SUBMITTED TO THE FACULTY OF THE GRADUATE SCHOOL
OF THE UNIVERSITY OF MINNESOTA
BY

Leo Mariappan

IN PARTIAL FULFILLMENT OF THE REQUIREMENTS
FOR THE DEGREE OF
DOCTOR OF PHILOSOPHY

Dr. Bin He, Adviser

August, 2014

Acknowledgements

I would like to thank Dr. Bin He, my advisor, for his guidance and constant support during this research. His generous help and insightful advice has allowed for steady progress towards this dissertation. I also would like to thank my committee members Dr. Emad Ebbini, Dr. Shai Ashkenazi, Dr. Taner Akkin for their time, support and stimulating discussions.

I would also thank the current and some former members of Biomedical Functional Imaging and Neuorengineering lab. The creative and supportive research environment in the lab made my research possible. I want to thank Dr. Xu Li for all the help and discussions at the beginning of this research. I'm very grateful to Dr. Gang Hu for his efforts in developing the MR MAT-MI experiment. I would also like to thank Dr. Xiatong Zhang, Mr. Kai Yu, and Mr. Jiaen Liu for the very useful and stimulating discussions. I would like to thank Dr. Pierre-Francois Van de Moortele and Dr. Kamil Ugurbil for help in conducting the MR MAT-MI experiment. I would also like to thank Dr. John Bishop, Qi Shiao, and Chunlan Jiang for their efforts in making the mouse tumor experiments possible. I would like to thank Dr. John Ballard and Dr. Andrew Casper for their help with ultrasound system development.

Dedication

This dissertation is dedicated to my lovely wife Amy and my parents. The blessing of their constant support gives me ongoing strength.

Abstract

Electrical conductivity imaging of biological tissue has attracted considerable interest in recent years owing to research indicating that electrical properties, especially electrical conductivity and permittivity, are indicators of underlying physiological and pathological conditions in biological tissue. Also, the knowledge of electrical conductivity of biological tissue is of interest to researchers conducting electromagnetic source imaging and in design of devices that apply electromagnetic energy to the body such as MRI. So, the need for a non-invasive, high resolution impedance imaging method is highly desired. To address this need we have studied the magnetoacoustic tomography with magnetic induction (MAT-MI) method. In MAT-MI, the object is placed in a static and a dynamic magnetic field giving rise to ultrasound waves. The dynamic field induces eddy currents in the object, and the static field leads to generation of acoustic vibrations from Lorentz force on the induced currents. The acoustic vibrations are at the same frequency as the dynamic magnetic field, which is chosen to match the ultrasound frequency range. These ultrasound signals can be measured by ultrasound probes and are used to reconstruct MAT-MI acoustic source images using possible ultrasound imaging approaches .The reconstructed high spatial resolution image is indicative of the object's electrical conductivity contrast. We have investigated ultrasound imaging methods to reliably reconstruct the MAT-MI image under the practical conditions of limited bandwidth and transducer geometry. The corresponding imaging algorithm, computer simulation and experiments are developed to test the feasibility of these different methods. Also, in experiments, we have developed a system with the strong static field of

an MRI magnet and a strong pulsed magnetic field to evaluate MAT-MI in biological tissue imaging. It can be seen from these simulations and experiments that conductivity boundary images with millimeter resolution can be reliably reconstructed with MAT-MI. Further, to estimate the conductivity distribution throughout the object, we reconstruct a vector source image corresponding to the induced eddy currents. As the current source is uniformly present throughout the object, we are able to reliably estimate the internal conductivity distribution for a more complete imaging. From the computer simulations and experiments it can be seen that MAT-MI method has the potential to be a clinically applicable, high resolution, non-invasive method for electrical conductivity imaging.

Table of Contents

Contents

List of Figures

Chapter 1

Introduction

Electrical property of tissue, referred to as bioimpedance, includes the electrical conductivity and permittivity. These parameters are an indicator of underlying physiological and pathological conditions in the body. For example, the measurement of thorax impedance is useful in monitoring cardiac and pulmonary functions such as stroke volume (Bache *et al* 1969) and lung ventilation (Baker and Geddes 1970). Bioimpedance reconstruction, especially with a high resolution imaging technique, could also have use in diagnosing and monitoring the structural changes in tissue. As such, this method could have application in early detection through screening for breast cancer, which has been shown in studies to have significantly higher conductivity than surrounding normal tissue (Surowiec *et al* 1988, Jossinet 1998), and early detection of breast tumors when the size is under 5 mm has been seen in clinical studies to lead to a survival rate reaching 96.2% (Carter *et al* 1989).

In addition to being applicable as a diagnostic tool, bioimpedance also plays an important role in other areas of biomedical research as a physical parameter necessary in the modeling of a biological system. For example, an accurate volume conductor model of the body is useful for studying the electrical activity of excitable tissue such as the heart and the brain (Malmivuo and Plonsey 1995). This could be used to improve the accuracy of imaging the source of this electrical activity in the excitable organs through surface recordings of the resultant electrical signals, as in electroencephalograms (EEG)

and electrocardiograms (ECG) (He 2004). A bioimpedance model of the body is also useful in understanding the interactions of the electromagnetic stimulations applied to the tissue as a part of a diagnostic or therapeutic system. Such modeling could be used to design and manage the application of electromagnetic energy to the tissue, as in a high field MRI system or with electrical neural stimulation systems like transcranial magnetic stimulation (TMS). Therefore, a high resolution, cost-effective and non-invasive imaging modality that can give accurate estimation of the electrical properties of biological tissue is highly desired.

Several techniques have been explored over the past few decades to address the need for estimating the electrical property distribution in biological tissue. These techniques involve inducing some form of electromagnetic field in the tissue being studied. Some components of this field are measured and are used to estimate the impedance distribution of the tissue. This is especially complicated due to the nonlinear dependence of the electromagnetic fields and the impedance. Various techniques used for imaging tissue impedance include electroamagnetic methods such as electrical impedance tomography (Barber and Brown 1984), magnetic resonance electrical impedance tomography (Khang *et al* 2002), magnetic induction tomography (Griffiths *et al* 1999), and microwave imaging (Maeney *et al* 2000). However, so far none of these methods have gained broad clinical applications due to their limitations either in spatial resolution or in the need of large current injection. Other than these electromagnetic methods, some hybrid methods that use electromechanical coupling have also been used which include magnetoacoustic tomography (Towe and Islam 1988), hall effect imaging (Wen *et al*

1998) and the recently proposed magnetoacoustic tomography with magnetic induction (He 2005).

1.1 Motivation

The magnetoacoustic tomography with magnetic induction (MAT-MI) technique is being developed to fulfill the need for a high resolution bioimpedance imaging method. This dissertation research aims to further develop and evaluate the MAT-MI method for bioimpedance imaging (Xu and He 2005).

In MAT-MI, ultrasound is generated in the object to be imaged by placing it in a dynamic and a static magnetic field. Eddy currents are induced in the object due to the dynamic field. The static field leads to generation of acoustic vibrations from Lorentz force on the induced currents. The acoustic vibrations are at the same frequency as the dynamic magnetic field which is chosen to match the ultrasound frequency range. This allows us to reconstruct the acoustic source distribution in the object using possible ultrasound imaging approaches. The conductivity distribution of the object can then be reconstructed from the obtained acoustic source map.

As compared to the other impedance imaging methods, MAT-MI has the following advantages. In MAT-MI, magnetic fields are used to induce currents in the object which can penetrate through tissue, especially under the 10 MHz frequency range (Wang and Eisenberg 1994) which is the frequency range used in MAT-MI, for high resolution imaging. This gives rise to uniform sensitivity throughout the object and overcomes the “shielding effect” due to low conductive outer layers (Wen 2000) experienced in methods that use surface electrodes to inject currents in the object. The

resolution of the image reconstruction with the MAT-MI method is governed by the resolution of the ultrasound imaging system. This depends on the bandwidth of the ultrasound system and the scanning aperture, and it can be in the mm range in the hundreds of kHz ultrasound frequency range or sub mm in the MHz frequency range. Additionally, the use of an ultrasound system can reconstruct the MAT- MI sources throughout the imaging object which leads to a well posed inverse problem while estimating the conductivity distribution. This is unlike some other methods that have ill posed inverse problems (Malmivuo and Plonsey 1995) due to the use of surface measurements of the globally integrated source fields. Also, the use of ultrasound imaging combined with magnetic fields that do not have to be strictly homogeneous over the entire object volume makes the MAT-MI method able to have relatively low cost, especially in comparison to systems that use MRI.

1.2 Scope of the dissertation

In chapter 2, introduction to bioimpedance and possible applications are presented. Then the methods for bioimpedance based imaging that have been studied over the last few decades have been surveyed.

In chapter 3, the description of the forward and inverse problem of MAT-MI acoustic source imaging is presented. Two methods for acoustic source imaging are described based on different ultrasound receiver transducers and corresponding scanning setups. Simulation methods for MAT-MI imaging with practical ultrasound setups are presented. These simulations are comparable to the experiment imaging. We then present our MAT-MI validation studies with biological tissue using experiment systems

consisting of stronger magnetic fields from the static field of an MRI machine and a strong magnetic pulser. Using a system with the strong magnetic pulser, we perform small animal tumor imaging with a mouse model.

In chapter 4, the vector source reconstruction method for MAT-MI imaging is presented. We present the imaging algorithm through the analysis of the acoustic pressure measured in MAT-MI generated by the vector current source, and the corresponding inverse imaging algorithms are developed. We have validated the vector source method for conductivity imaging in MAT-MI computer simulations, and in the numerical simulations we study the spatial resolution of the image reconstruction with the estimation of the full width half maximum of the point spread function based on the Rayleigh criterion. We have further performed experiments with gel phantoms, biological tissues and ex-vivo liver tumor tissue to validate the conductivity imaging method.

In chapter 5, the major conclusions and contributions of the present dissertation research are summarized and possible future works are also discussed.

Chapter 2

Background

2.1 Bioimpedance Overview

The concept of electrical impedance has been used since the late 1800's to describe the response of a material in the presence of electromagnetic fields. In terms of bioimpedance, it is the measure of the electrical properties of biological tissue. The electrical properties that most vary between tissues are conductivity σ (or resistivity $\rho = 1/\sigma$) and permittivity ϵ. The bulk impedance of a material corresponding to these electrical properties can be measured through the resistance and capacitance which can be combined to give the complex impedance of the material (Foster and Schwan 1989, Brown *et al* 1999). Empirical models have been developed in terms of resistances and capacitance to represent the tissue impedance, especially the variation of impedance with frequency (Cole and Cole 1941, Brown *et al* 1999).

The electrical properties of biological tissue are determined by their constituents. Any tissue is formed by extracellular fluid and cells. The extracellular fluid (ECF) usually denotes all bodily fluid outside of cells. This medium which surrounds the cells contain proteins and ions and can be divided into plasma (20% of ECF) and interstitial fluid (80% of ECF). On the other hand, the cell is constituted by a lipid bi-layer plasma membrane. Inside this cell membrane is an intracellular fluid, also known as cytosol, organelles and the nucleus of the cell. Due to free ions contained in the extracellular and intracellular fluid, any biological tissue can be considered as an electrolyte. Additionally, the tissue also behaves as a dielectric due to its constituents with the major contribution

to the dielectric behavior coming from the plasma membrane of the cell structure. This membrane is a lipid bi-layer structure with a very poor intrinsic electrical conductance. Thus, tissues exhibit the properties of both the conductors and dielectrics due to the presence of both free and bound (fixed) charges. The conductivity term (σ) accounts for the movement of free charges, and the permittivity term (ϵ) accounts for the movement of bound charges in the dielectric due to an applied electrical field.

It is also well known that the electrical properties of biological tissues are temperature and frequency dependent. The temperature coefficients for both conductivity and permittivity, however, are also tissue type and frequency dependent and have not been generalized from the limited amount of data from literature. The highest temperature coefficients are around 1-2 % C-1 (Gabriel *et al* 1996a).

The frequency dependence of tissue conductivity has been seen to be due to various components of tissue behaving differently with changing frequency. Both relative permittivity and conductivity are found to be a function of frequency with the relative permittivity decreasing with frequency and the conductivity increasing with frequency. This change with frequency is categorized into three main subdivisions called α, β and γ dispersions. The α dispersion happens at low frequencies, 10 Hz – 10 kHz. This is attributed to three causes: the conductivity of endoplasmic reticulum, the channel proteins present in the plasma membrane and the interaction of ions on the charged cellular surface. The range of the β-dispersion is approximately from 10 kHz to MHz range (Ivorra *et al* 2005). It is caused by the non-conductive, capacitive properties of the cell membrane and other internal membranes with their interactions with the extra and intra-

cellular electrolytes. The γ dispersion, happening in the GHz region, is due to the polarization of water molecules (Foster and Schwan 1989, Gabriel *et al* 1996a). Additionally, a weak dispersion called δ dispersion occurs in the 300 MHz to GHz range between the β and γ dispersion. This dispersion is caused by the rotation of amino acids, partial rotation of charged side groups of proteins, and proteins bonded to water.

Also, many biological tissues are highly anisotropic; that is, the conductivity in different directions is not the same. Anisotropy can be represented by three principal conductivities in three mutually perpendicular directions as determined by the structure of the material (Foster and Schwan 1989). For example, skeletal muscle is found to be anisotropic with the conductivity along the fiber axis (longitudinal) much higher than in a perpendicular direction (Plonsey *et al* 1969). So, tissue impedance depends on its structure and geometry. The anisotropy of myocardial tissue has also been investigated by using two perpendicular linear arrays of four electrodes (Steendijk *et al* 1993). In this work, the measured conductivity is related to the direction θ of the fibers and then used to calculate the conductivities in the parallel and perpendicular directions:

$$\sigma(\theta) = \sqrt{(\sigma_L Sin\,\theta)^2 + (\sigma_T\, Cos\,\theta)^2} \qquad (1.1)$$

where $\sigma(\theta)$ is the conductivity at angle θ, σ_L is the conductivity in the parallel direction, and σ_T is the conductivity in the perpendicular direction.

This equation was determined by considering tissue impedance measurements using point electrodes. In practice, electrodes have a finite diameter and large errors can arise when equation 1.1 is used. In addition, the accuracy of tissue impedance measurements are limited by the immediate electronics involved in the measurements.

Variables such as temperature, current density, electrode/tissue interface impedance and type of electrode are also relevant factors. In the following section, the methods for direct measurement of tissue impedance are discussed.

Direct Bioimpedance measurement

The methods involved in measuring the bulk impedance of tissue use electrodes to apply known currents and measure the resulting voltage. The resultant voltage can be measured by using the same electrodes which were used for current injection (bipolar technique), or a separate pair of electrodes can be used for potential measurement (tetrapolar technique). Additionally, impedance spectroscopy can also be performed by varying the frequency of the applied currents and measuring the voltages. A diagram of the bipolar impedance technique can be seen in figure 1.

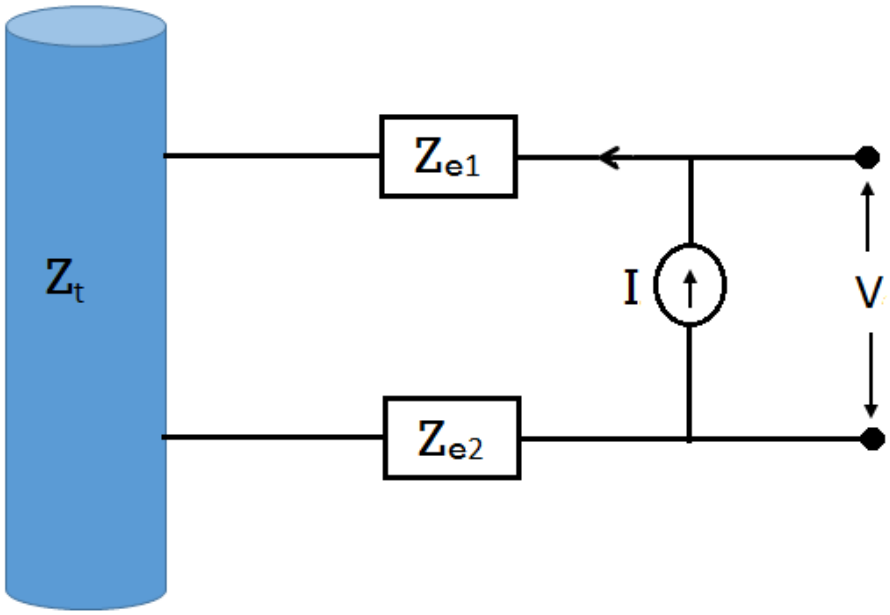

Fig. 1, Two electrode (bipolar) impedance measurement cell

The measured voltage impedance in this case can be described as follows :

$$Z = \frac{V}{I} = 2Z_e + Z_t$$

where Z is the total impedance of the circuit and V is the voltage measured at the electrode, I is the current injected into the tissue, Z_e is the impedance of each electrode (on assuming $Z_{e1} = Z_{e2}$), Z_t is the tissue impedance. So, in this technique the electrode impedance needs to be accounted for in determining the tissue impedance.

Additionally, frequency dependent polarization impedance on the electrode-tissue interface and the contact impedance which is largely capacitive also occur in series with the electrode impedance. The polarization impedance can be reduced by using carefully chosen electrode material (Gabriel *et al* 1996b) or through certain compensation methods (Schwan 1963). In the β dispersion range, the contact impedance with the skin is in the range of 2-10 times the tissue impedance (Rosell *et al* 1988), and then in order to obtain values of electrical impedance that can be used to provide information about the tissue, the contribution of the skin impedance must be removed. On the other hand, the tetrapolar measurement technique is less sensitive to the effects of electrodes or contact impedance on the measurement. A diagram of the tetrapolar technique can be seen in figure 2. When the output impedance of the current generator Z_s and the input impedance of the differential amplifier Z_v are large as compared to the sum of the electrode and tissue impedances, the measured impedance is less sensitive to the errors caused by electrode impedance as follows:

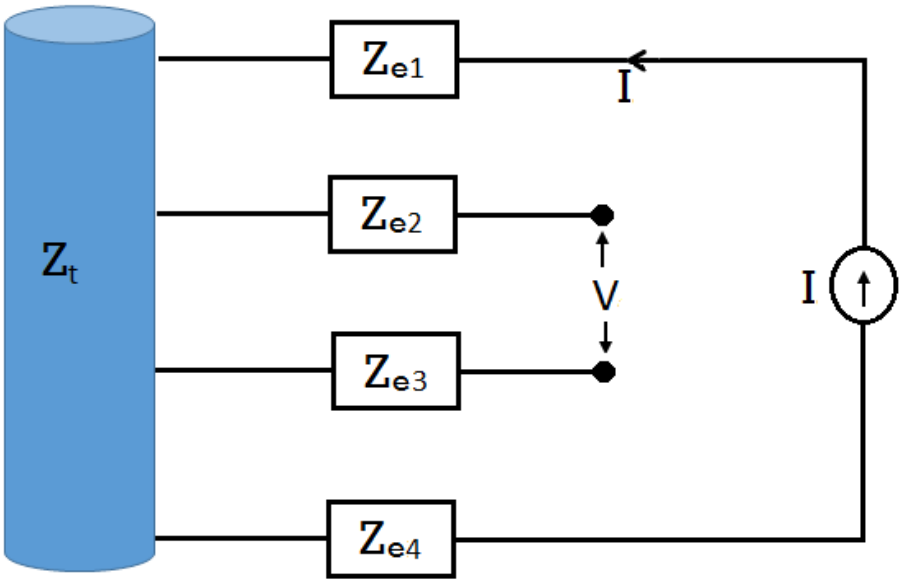

Fig. 2, Four electrode (tetrapolar) impedance measurement cell

$$Z = \frac{Z_t}{1+Z_t\cdot\left(\frac{4Z_e+Z_v+Z_S}{Z_v\cdot Z_S}\right)+2Z_e\cdot\left(\frac{2Z_e+Z_v+Z_S}{Z_v\cdot Z_S}\right)} \approx Z_t$$

where the electrode impedances $Z_{e1} = Z_{e2} = Z_{e3} = Z_{e4} = Z_e$, Z is the equivalent impedance and Z_t is the tissue impedance under measure. Additionally, when the contact impedance which occurs in series where the electrode impedance is present, it's contribution is also negligible (Ragheb *et al* 1992).

In practice, calibration of the electrode constant is required and is often done using standard solutions with known conductivity. However, as the electrode constant is determined by the object's geometry, electrode configurations and the relative position of the electrodes in the tissue, an ideal calibration which has the minimum measurement error may be hard to obtain (Tsai *et al* 2000). For in vitro measurements, if the tissue

sample is homogeneous it is easy to derive the conductivity or resistivity value of the sample as the current density inside the measurement cell is generally uniform (Baker 1989). For in-vivo measurements, because most tissue samples are inhomogeneous, sometimes anisotropic and have complex geometry, the injected current flow pattern is generally unknown, and it is difficult to derive tissue conductivity directly. However in a multi-layer tissue, when the tissue extent is large such as the myocardial tissue (Fallert *et al* 1993, Cinca *et al* 1997, Tsai *et al* 2000, Paulson et al 2004), these measurements can be applied. Theoretically, the inter electrode spacing needs to be smaller than one-third of the thickness of the tissue layer in order to accurately derive tissue conductivity (Robillard and Poussart 1979).

2.2 Bioimpedance applications

Several studies have been performed to measure the impedance tissue in normal and disease states (Gabriel *et al* 1996a, Gabriel *et al* 1996b, Geddes and Baker 1967, Stuchly and Stuchly 1980, Duck 1990). It is seen in the measurements that different tissue types have different electrical impedances. So impedance based imaging can be used to reconstruct tissue structures. Also, from the measurements it is seen that electrical properties are sensitive to physiological and pathological changes in tissue due to the change in cell structure (Zou and Guo 2003). For example, in cases of cancer such as in breast tumors, it is seen that cancerous tissue has significantly different electrical properties or impedance spectrum parameters than normal breast tissue or benign tumors (Surowiec *et al* 1988, Jossinet 1998, Jossinet 1996, Jossinet and Schmitt 1999, Morimoto *et al* 1990, Zou and Guo 2003, Kerner *et al* 2002, Poplack *et al* 2007). Significant

electrical conductivity differences have also been found between liver tumors and normal liver tissue (Haemmerich *et al* 2003, Haemmerich *et al* 2009). There is also evidence showing that the electrical properties of prostate cancer tissue and skin basal cell carcinoma are significantly different than the benign or normal prostate and skin tissue respectively (Halter *et al* 2009, Beetner *et al* 2003). Also, most bodily fluids have quite different conductivity and permittivity than most other soft tissues (Fallert *et al* 1993, Cinca *et al* 1997), so impedance of tissues under conditions of ischemia, hemorrhage or edema can be very different. This can be used in brain imaging such as with a stroke (Clay and Ferree, 2002), for detection and monitoring of pulmonary edema, for monitoring cardiac function or for peripheral blood flow measurement (Brown *et al* 1985, Dawids 1987, Holder 2002) . Also, studies have been conducted to image brain activity and hemodynamic responses associated with neural actictivities (Klivington and Galambos 1967, Klivington and Galambos 1968, Galambos and Velluti 1968, Holder *et al* 1996, Tidswell *et al* 2001, Bagshaw *et al* 2003, Gilad *et al* 2009a, Gilad *et al* 2009b).

The knowledge of electrical conductivity distribution is useful in the study of the interaction of electromagnetic energy with tissue. This is especially useful in the study of sources of body electrophysiological signals such as electrocardiograms (ECG) (heart signals). Some studies have shown that the accuracy of the volume conductor model in terms of geometry and tissue conductivity values could have influence on the signal modeling of body surface potentials generated by neural or cardiac sources (Haueisen *et al* 1997, Rudy *et al* 1979, Klepfer *et al* 1997, Awada *et al* 1998). This influences the inverse source localization with these signals, so researches have tried different ways in

order to get a more accurate estimation of the tissue conductivity properties (Rush and Driscoll 1968, Lai *et al* 2005, Zhang *et al* 2006).

Electromagnetic energy interaction with biological tissue is capable of causing nerve stimulation and heating. These effects need to be taken into consideration while designing systems that apply EM energy to tissue (Sadlier *et al* 2010) for efficient and safe use. The reconstructed tissue electric property distribution can be used to estimate the electric fields and the induced currents, which in turn can be used to predict the energy deposition. This can be seen in improving the safety and accuracy of MRI system design by the estimations of the specific absorption rate (SAR) and field inhomogeneity in high field MRI (Yang *et al* 2002, Katscher *et al* 2009b, Zhang *et al* 2010). Such estimates of the induced field can also be used in therapeutic systems such as transcranial magnetic stimulation, transcranial direct current stimulation (tDCS) (Sadleir *et al* 2010, Bikson *et al* 2009, Datta *et al* 2009, Datta *et al* 2010) and in RF induced ablation of tissue (Solazzo *et al* 2005).

2.3 Bio-impedance Imaging

Given the potential applications for the estimation of bioimpedance distribution, several imaging techniques have been explored in the last few decades. These can be classified based on the types of stimulation and measurements used for the image reconstruction. Here, we have characterized them into two broad categories: electromagnetic methods, which use electromagnetic fields including electric and magnetic fields to probe the tissue impedance, and hybrid methods, which use electromagnetic fields in combination with other forms of energy coupled through an

energy transfer mechanism to reconstruct the tissue impedance. The electromagnetic methods explored include electrical impedance tomography (EIT), magnetic induction tomography (MIT), magnetic resonance electrical impedance tomography (MREIT), magnetic resonance electrical property tomography (MREPT) and microwave imaging of tissue. All these modalities use electromagnetic stimulations such as current injection, magnetic induction or electromagnetic wave stimulation and perform the corresponding electromagnetic measurements such as electrical voltage sensing through electrodes or magnetic sensing through coils or microwave measurement. The hybrid methods that are considered here use a Lorentz force based coupling mechanism between electromagnetic energy and acoustic/mechanical energy. These hybrid methods include magnetoacoustic tomography (MAT), Hall effect imaging (HEI) and magnetoacoustic tomography with magnetic induction (MAT-MI). A more detailed review of these techniques is presented in the following sections of this chapter.

2.4 EIT

Electrical impedance tomography (EIT) is one of the earliest bioimpedance imaging methods to be developed. In this method, surface electrodes are used to inject currents into the object region Ω, and the resultant surface voltages are measured. Using a set of measured voltages, corresponding to different injection current patterns, the impedance image can be reconstructed (Barber and Brown 1984, Brown *et al* 1985, Metherall *et al* 1996, Jossinet *et al* 2002, Brown 2003). These injected currents and voltages can be described by the following Poisson's equation:

$$\nabla \cdot \left(\gamma(r)\nabla\varphi(r)\right) = 0, in\ \Omega$$

$$\nabla\varphi(r) \cdot \boldsymbol{n} = 0\ \ , at\ \ \Gamma_1\ d\Omega$$

$$\int \nabla\varphi(r) \cdot \boldsymbol{n} = \pm I\ \ , at\ \ \Gamma_2\ d\Omega$$

where $\varphi(r)$ is the electrical potential in the conductive object volume Ω, $\gamma(r) = \sigma(r) + j\omega\epsilon(r)$ is the complex admittivity, $\boldsymbol{n}$ is the surface normal, $\pm I$ corresponds to the current flowing in and out of the medium, Γ_2 is the region of the surface where the current injection electrodes are placed and Γ_1 corresponds to rest of the object surface region. For a known conductivity distribution σ and current injection pattern, the above forward problem can be solved in the domain Ω for the electric potential φ using methods such as the finite element method (FEM) modeling. The inverse problem on the other hand involves estimating the impedance from the voltages measured on the surface. Due to the limited number of unique points on the surface at which the voltages can be measured, the EIT inverse problem suffers from ill-posedness. This results in the low spatial resolution impedance images that can be obtained by the EIT method. If there are N electrodes used in EIT, the number of independent measurements possible are $\frac{N(N-1)}{2}$. Though, theoretically, a large number of electrodes can be used to improve the condition number during the inverse solution, in practice this is hard to implement due to the complexity of instrumentation and the increasing correlation between individual measurements (Malmivou and Plonsey 1995). In spite of its low spatial resolution, the EIT technique has its advantages of low cost, safety and high speed.

Several image reconstruction algorithms have been explored for EIT, which include methods based on linearization of the forward problem (Mithrall *et al* 1996) or iterative methods (Woo *et al* 1992). Among the different methods, as the iterative methods account for non-linearity in the signal generation process, they are more accurate. However, real time applications of EIT require a faster image reconstruction method. Two types of reconstructed images have been considered in EIT applications. The first is known as difference imaging, where a change in ratio or percentage represents some physiological parameter like blood volume or cell size. The earliest lung images were produced using this method. The images are obtained by measuring two data sets at different times or frequencies at the boundary of the object. This is then subtracted and divided by a reference data set. The second is absolute imaging which produces an image of the absolute conductivity or permitivity. This method of imaging is technically more difficult than the difference method, as the contact impedance of the electrodes cannot be accurately characterized when making clinical measurements. The methods of injecting current into the domain under investigation are also varied based on the application. They can be classified into adjacent, opposite, and optimum injection. However, the different designs using different patterns of current injection and voltage measurement have different imaging sensitivity patterns. The neighboring method has better sensitivity at peripheral regions but has degraded sensitivity in the object's center. Adaptive method on the other hand has more uniform but lower sensitivity over the space if a similar amount of current is injected into the body. Additionally, the current injection pattern also depends on the complexity of the hardware, possibly increasing the error in

each channel. FEM based methods have been used to study the optimum current injection pattern for different applications (Bayford *et al* 1995). The impedance measurements can also be performed at several frequencies called electrical impedance spectroscopy (EIS). This method has been seen to be able to better quantify the tissue (Kerner *et al* 2002, Yerworth *et al* 2003, Romsauerova *et al* 2006, Boverman *et al* 2008).

Several applications of EIT have been considered in research such as imaging ventilation and detection of blood clots in the lungs or pulmonary emboli (Brown 2003, Hampshire *et al* 1995). In addition, studies have been conducted on EIT/EIS for breast tumor imaging and head imaging (Kerner *et al* 2002, Poplack *et al* 2007, Romsauerova *et al* 2006, Boverman *et al* 2008, McEwan *et al* 2006). However, although these applications show great potential, the clinical usefulness of EIT is still under study.

2.5 MIT

Magnetic induction tomography uses magnetic fields for imaging, so it is sensitive to all three electromagnetic properties of the object, namely conductivity, permittivity and permeability. In addition, unlike methods using surface injected currents for imaging which have to deal with the ill-defined electrode skin interface, the magnetic fields are not restricted by the "shielding effect" caused by outer, low conductive tissues preventing injected currents from probing the inner tissue region (Wen 2000). In MIT, an excitation coil array is used to apply an alternating magnetic field ($\boldsymbol{B_0}$) to the conductive object that results in eddy currents in the object. This current leads to generation of secondary magnetic fields ($\boldsymbol{B}$) which are measured with receiver coils outside the object,

and several such measurements corresponding to different excitation patterns are then combined to estimate the conductivity distribution of the object.

The strength of the secondary field induced in biological tissue is much smaller than the excitation field as tissue is a weak conductor of electricity. In general, $\boldsymbol{B}$ will have real and imaginary components representing the permittivity and conductivity of the sample. For biological tissues, the conductivity (imaginary) component will normally be dominant. In an attempt to increase the size of the signals, work has been done in using higher frequencies than in industrial MIT or conventional EIT (Griffiths 2001). For a volume of a typical high water content tissue such as muscle ($\sigma = 1\ S/m$) in an MIT measurement at 10 MHz, the predicted size of the secondary signal is still only about 1% of the excitation field (Griffiths *et al* 1999). To reliably measure the secondary magnetic field cancellation of the main excitations through back off coils (Griffiths *et al* 1999), special oriented coils (Watson *et al* 2004, Scharfetter *et al* 2005, Scharfetter *et al* 2001, Karbeyaz and Gencer 2003) and gradiometers (Scharfetter *et al* 2001, Karbeyaz and Gencer 2003, Reidel *et al* 2004, Zheng *et al* 2009) have been used in order to control the dynamic range of the collected signal from the receiver coils. Other than the design of the receiver coils, modified excitation coil design has also been proposed (Stawicki *et al* 2009) to reduce the influence of the primary field in addition to shields to concentrate the primary magnetic field in the given region (Barba *et al* 2009, Yin *et al* 2010).

The magnetic excitation used in MIT is in the MHz range which leads to magnetic fields with slow time variation such that the propagation time of the field through the object is negligible. This allows the magnetic induction problem in MIT to be considered

as quasi-static. The skin depth of the corresponding MHz field in general biological tissue is at the level of meters, which is much larger than the characteristic dimension of the object, so the magnetic diffusion can be ignored. Thus, in the MIT problem description, the effect of the induced current on the primary field can be ignored and described as follows:

$$\nabla \cdot \big(\gamma(r)\nabla\varphi(r)\big) = -j\omega \boldsymbol{A}(r) \cdot \nabla\gamma(r), in\ \Omega$$

$$\big(\nabla\varphi(r) + j\omega A(r)\big) \cdot \boldsymbol{n} = 0\ \ , at\ d\Omega$$

where $\varphi(r)$ is the electrical potential in the conductive object volume Ω, $\gamma(r) = \sigma(r) + j\omega\epsilon(r)$ is the complex admittivity, and $A(r)$ is the magnetic vector potential corresponding to the primary magnetic field $\boldsymbol{B_0}$. The above equation can be solved to determine the induced currents and the secondary magnetic field ($\boldsymbol{B}$) can be estimated using Biot Savart's law. The secondary magnetic field leads to induced voltages measured in the sensing coils which are used to estimate the conductivity distribution in the object. However, similar to EIT, the number of surface excitations and measurement coils is limited, and this leads to an ill-posed inverse problem due to the limited number of independent measurements possible. Several methods have been explored to reconstruct the object impedance map in MIT. Some of these are linear methods using a sensitivity matrix based solution (Karbeyaz and Gencer 2003, Gursoy and Scharfetter 2009a, Merwa *et al* 2005) applicable to low contrast objects (Soleimani 2008). Additionally, non-linear regularized methods (Soleimani and Willuhn 2004), the use of a-priori knowledge (Casanova *et al* 2004a), and FEM based forward solvers (Chen *et al* 2010, Hollaus *et al* 2004), have all been proposed to improve the reconstruction process.

The MIT method has been explored for biomedical applications such as heart and lung imaging and monitoring and for imaging hemorrhagic stroke and edema (Gursoy and Scharfetter 2009b, Zolgharni *et al* 2009a, Zolgharni *et al* 2009b). Additionally, applications in detection of pathological change and monitoring of physiological processes are possible (Liu *et al* 2005).

2.6 MREIT

Magnetic resonance electrical impedance tomography (MREIT) is a method that is being developed to deal with the technical difficulties of EIT. In this method, an MRI machine is used to measure the magnetic flux in the object generated by externally applied currents, and this is used to reconstruct the conductivity image. MREIT combines EIT with the magnetic resonance current density imaging (MRCDI) technique which is a method capable of imaging the current density distribution in the object using an MRI scanner. For the current density imaging, a low frequency current pulse is injected into the imaging object using surface electrodes similar to EITs. The magnetic flux generated by the injected currents leads to phase shifts in the measured MRI signals. The raw MRI k-space data $S^{\pm}$ corresponding to positive or negative injected currents I^{+} or I^{-} can be described by the following equation (Woo and Seo 2008) :

$$S^{\pm}(m,n) = \iint M(x,y) e^{j\delta(x,y)} e^{\pm j\gamma_h B_z T_c} e^{j(xm\Delta k_x + yn\Delta k_y)} dxdy$$

where $M(x,y)$ is the MRI magnitude image, γ_h is the gyromagnetic ratio of proton, T_c is the duration of current injection, and $\delta(x,y)$ corresponds to systematic

phase artifacts. The B_z field can then be measured using the following equation (Woo and Seo 2008):

$$B_z(x,y) = \frac{1}{2\gamma_h T_c} \arg\left(\frac{M^+(x,y)}{M^-(x,y)}\right)$$

where $M^{\pm}(x,y)$ are the complex images obtained by taking the fourier transform of $S^{\pm}(m,n)$. Using the MRI scanner with its main magnetic field in the z direction, the MRCDI method can obtain the B_z field distribution alone. When a current $\boldsymbol{J}$ ($\boldsymbol{J_x}, \boldsymbol{J_y}, \boldsymbol{J_z}$) is present in an object, this would lead to magnetic field $\boldsymbol{B}$ ($\boldsymbol{B_x}, \boldsymbol{B_y}, \boldsymbol{B_z}$). So to obtain the current density in the MRCDI method, the $\boldsymbol{B_x}, \boldsymbol{B_y}$ components of the magnetic field would also have to be measured. This can be done by rotating the object twice inside the MRI scanner. The current distribution $\boldsymbol{J}$ can then be determined using the Ampere law: $\boldsymbol{J} = (\nabla \times \boldsymbol{B})/\mu_0$, where μ_0 is the magnetic permeability of free space (Joy *et al* 1989, Scott *et al* 1991, 1992, Scott 1993, Joy *et al* 1999, Yoon *et al* 2003, Joy 2003). In the MRCDI based impedance imaging method as proposed in current density impedance imaging (CDII) (Hasanov *et al* 2008), the estimated current density $\boldsymbol{J}$ from at least two excitations can be used to reconstruct the conductivity distribution (σ) as follows:

$$\nabla \times \boldsymbol{J} = \frac{\boldsymbol{\nabla}\sigma \times \boldsymbol{J}}{\sigma} = \nabla \ln(\sigma) \times \boldsymbol{J}$$

when $\boldsymbol{E} = \nabla\varphi$, where E is the electric field and φ is the electric potential. $\nabla \ln(\sigma)$ can be uniquely determined from the two excitation currents ($\boldsymbol{J_1}, \boldsymbol{J_2}$) when $\boldsymbol{J_1} \times \boldsymbol{J_2} \neq 0$. The conductivity can be determined non-iteratively from $\nabla \ln(\sigma)$ and boundary (S) measurement of conductivity value:

$$\ln(\sigma) = \int_v \nabla \ln(\sigma) \cdot \nabla_{\mathbf{r}'} G(\boldsymbol{r}, \boldsymbol{r}')\, d^3\boldsymbol{r}' - \oint_S \sigma(\boldsymbol{r}')\, \frac{\partial G(\boldsymbol{r}, \boldsymbol{r}')}{\partial \nu}\, ds'$$

where G is the free space green's function for Laplace operator.

The other MREIT methods of image reconstruction explored earlier also used the measured current density map $\boldsymbol{J}$ (Zhang 1992, Woo *et al* 1994, Eyuboglu *et al* 2001, Kwon *et al* 2002, Ider *et al* 2003, Oh *et al* 2003, Birgul *et al* 2003). However, in practice, the measurement of all three orthogonal components of the $\boldsymbol{B}$ field by rotating the object inside an MRI scanner is difficult to achieve. In order to avoid rotating the object, several conductivity reconstruction algorithms using the B_z field alone have been explored. The harmonic B_z algorithm (Seo *et al* 2003) is one such commonly used method, which uses the following equation to estimate the conductivity gradient: $\nabla^2 B_z = \nabla\sigma \times \nabla\varphi$ combined with two B_z measurements from different excitations. Some methods such as gradient B_z decomposition algorithm (Park *et al* 2004a), vibrational B_z algorithm (Park *et al* 2004b, Kwon *et al* 2005), and local harmonic B_z algorithm (Seo *et al* 2008) have been explored to improve the noise tolerance of harmonic B_z algorithm. Other methods explored using the B_z field include estimating J from B_z field (Seo *et al* 2003a) and using the component of current recoverable from B_z alone (Park *et al* 2007, Nam *et al* 2007).

These developed image reconstruction algorithms for the MREIT method have been used in validation studies of non-biological and biological phantoms. Further, postmortem animal imaging and in-vivo animal and human experiments have been performed (Hamamura *et al* 2006, Oh *et al* 2004, Oh *et al* 2005, Lee *et al* 2006, Sadleir *et al* 2006, Kim *et al* 2007, Kim *et al* 2009). In addition, MREIT studies with animal tumor

models have shown promising results (Muftuler *et al* 2006). From these studies, it is seen that MREIT can overcome the limited resolution imaging possible with the ill-posed EIT method by using the current density image at all the voxels inside the object space. So the reconstructed MREIT image resolution is governed by the resolution of the MRI scanner which can be in the mm or sub mm range. The current MREIT systems require a high level of current injection (up to 10 mA) for image reconstruction and ongoing research in MREIT involves using safe levels of current injection for image reconstruction applicable to general human imaging.

2.7 MREPT

MREPT is a method that uses the MRI machine for impedance imaging, and the impedance is reconstructed at the Larmor frequency of the MRI system (Katscher *et al* 2009a, Katscher *et al* 2009b, Zhang *et al* 2010). In MREPT, the perturbations to the RF field due the currents induced in the objects are measured by use of the B_1 mapping technique. This measured secondary RF field is then used to derive the conductivity and permittivity of the object. The signal detection of MREPT does not require any additional hardware than the MRI machine, as the excitation field is the MRI's intrinsically used RF stimulation and the measurements are made with the RF field measurement system already used in the MRI. As this technique does not need any surface electrode mounting or current injection, it has better flexibility than some of the other bioimpedance imaging methods when successfully developed. In addition, similar to the MREIT method, by measuring the secondary field throughout the object, the inverse problem is well posed

and the resolution of the imaging system is governed by the resolution of the MRI system. Thus, the MREPT method is capable of high resolution electrical properties imaging.

Although in its early stage of development, potential applications for brain imaging (Zhang *et al* 2012) and cancer imaging (Shin *et al* 2013) have been explored. In addition, as the electrical properties are at the frequency of operation of the MRI system, the measured impedance can be directly used to design safe excitations for MRI (Zhang *et al* 2013). However, as an emerging technique, more studies are still needed to fully demonstrate its feasibility and medical values.

2.8 Microwave Imaging

Microwave imaging is an active wave based non-invasive imaging method in which the scattering phenomena of microwave signals is used as the mechanism for probing biological tissue (Bolomey *et al* 1982, Maeney *et al* 2000). Microwave radiation comprises of a fraction of the electromagnetic spectrum in the range of ~ 1 GHz to 30 GHz. In this frequency range the electromagnetic field is non-ionizing and at safe illumination powers can penetrate into the tissue. Microwave imaging is sensitive to the variations of electric properties of the tissue (σ, ϵ) as the propagation of microwave through such an inhomogeneous medium leads to variations in amplitude, phase and polarization of the wave. The distorted fields can be measured using microwave antennas to reconstruct the electrical properties.

The wave equation based on the Maxwells equation can be used to describe the propagation of the microwave field. In case of the incident field being vertically polarized and the object properties being homogenous along the vertical z-axis, a simplified scalar Helmholtz's equation describing the time harmonic electric field can be used to describe the microwave field. This can be defined as follows:

$$(\nabla^2 + k^2)e(\boldsymbol{r}) = 0$$

where k is the wavenumber of the electromagnetic (EM) wave containing the dielectric properties of the medium of propagation, $e(r)$ is the total electric field, including interactions with an object. Several different methods can be used to implement the wave equation in the forward problem, where the geometry of the exciting antennas combined with the known electrical property of tissue can be used to solve the microwave distribution in the medium. The common methods used are based on the Method of Moments (MoM) (Maeney *et al* 2000) and Finite Element Method (FEM) in hybrid with the Boundary Element (BE) formulation, or in some cases Finite Difference Method (FDM).

The two major approaches of microwave imaging explored are the radar based approach and tomographic methods, where cross-sectional slices of the dielectric properties are generated. In the tomographic methods, the inverse scattering problem is solved numerically and can be divided into two different groups. In the first approach based on diffraction tomography, the Born approximations are used to simplify the microwave scattering to a linear process. This method is shown to be very computationally efficient in obtaining quasi real-time imaging, especially for low contrast

objects (Bolomey *et al* 1982, Pichot *et al* 1985, Joisel and Bolomy 2000, Chew and Wang 1990). However, in the case of large contrast seen in biomedical applications, this method leads to significant errors (Slaney at al 1984). Non-linear iterative approaches have also been explored for microwave imaging to improve the accuracy of reconstruction. In the radar based approach, the strong scattered fields in the object are imaged by attributing the signal to the source using the time of flight of the backscattered waves (Li et. al 2003).

Microwave imaging for biomedical applications have been studied to image breast tumors and for temperature change measurements (Li *et al* 2004, Fear *et al* 2002, Miyakawa 1993). However, the complexity of the microwave scattering process limits the accuracy of the image reconstruction method, which also degrades the imaging resolution (Liu *et al* 2002).

2.9 MAT

Magnetoacoustic tomography is a method proposed to measure current densities by electro acoustic coupling currents (Towe and Islam 1988, Islam and Towe 1988, Roth *et al* 1994). A time varying magnetic field applied to a current carrying conductor or oscillating currents in a stationary magnetic field would give rise to mechanical vibrations through Lorentz force coupling. The induced acoustic signal can then be measured through external hydrophones which can be used to determine the strength of the current source in the object. Experiments were performed with known values of external currents applied to electrolytes, tissue and small animals, and the measured acoustic signal was found to be linearly related to the strength of the current source

(Towe and Islam 1988a). A simulation study also showed that current dipole sources in a volume conductor could be reconstructed using the MAT approach (Islam and Towe 1988b).

The forward problem of signal generation for MAT consists of determining the induced pressure due to the Lorentz force in the medium. This can be described using the Navier stoke equation which has also been used to develop a model for cardiac tissue (Roth 2011, Roth *et al* 1994):

$$G\nabla^2\boldsymbol{u} - \nabla p + \boldsymbol{J} \times \boldsymbol{B} = 0$$

where G is the shear modulus of the tissue, $\boldsymbol{u}$ is the displacement, p is the pressure in the tissue and $\boldsymbol{J}, \boldsymbol{B}$ are the current density and magnetic field in the tissue giving rise to the Lorentz force $\boldsymbol{J} \times \boldsymbol{B}$.

The tissue is assumed to be incompressible ($\nabla \cdot \boldsymbol{u} = 0$), taking the divergence of eqn () gives the poisson's equation governing the pressure in the object:

$$\nabla^2 p = \nabla \cdot (\boldsymbol{J} \times \boldsymbol{B})$$

As we can see from the above equation, the ultrasound pressure that is generated is proportional to the strength of the current in the sample as also observed in the experiments (Towe and Islam 1988). However, this technique for bioelectrical current detection has not been implemented in practical experiments.

2.10 HEI

Hall effect imaging is a technique using Lorentz force based effects that can be induced in tissue. In this method the charge separation is created by ultrasound vibrations in tissue in the presence of an external magnetic field. The induced voltages from this

charge separation are measured with surface electrodes which can be used to determine the electrical properties (Wen *et al* 1998, Wen 2000, Wen 1999). In the experiments performed with this method, an ultrasound transducer is used to apply pressure waves to the tissue. The ultrasound wave pulse propagates through the sample, and the conductivity distribution of the sample along the wave is encoded in the time course of the measured voltages. For an ultrasound pulse travelling along the z direction perpendicular to the direction of magnetic field $\boldsymbol{B_0}$, the Hall effect voltage measurements can be described as follows (Wen *et al* 1998):

$$V_h(t) = \alpha W R_d B_0 \int M(z,t) \partial_z \left(\frac{\sigma(z)}{\rho(z)} \right) dz$$

where $M(z,t) = \int_{-\infty}^{t} p(z,\tau) d\tau$ is the ultrasound momentum transmitted across position z at time t, α is constant representing the portion of current collected by electrodes into the detection circuit electrode R_d, $\sigma(z)$and $\rho(z)$ are the conductivity and density distribution of the imaging object along the z direction, and ∂_z is the derivative along the z direction. It can be seen from the above equation that the Hall voltage is proportional to the derivative of the conductivity and density along the ultrasound propagation direction. When the ultrasound transducer applies a pressure signal along one line (A Scan) through the object, the time course of the measured voltage signal at the electrodes corresponds to the propagation of the pressure wave through the tissue. The measured voltage amplitude then corresponds to the conductivity boundaries along the direction of ultrasound. This can be used to reconstruct the image of the tissue boundaries

along the pressure wave line. Several such line scans can be combined to reconstruct the conductivity boundaries of the sample.

A reverse "Hall effect" imaging technique similar to MAT has also been described to image tissue conductivity (Wen *et al* 1998). In this approach, the current is driven by a voltage through surface electrodes which in the HEi imaging approach was used for measurements. This current gives rise to vibrations in the tissue (like in magnetoacoustic imaging). The generated pressure is then measured using ultrasound transducers. The pulser then generates a voltage pulse. The wave equation for this reverse effect can be described as follows (Wen and Wikswo, 1999):

$$\nabla^2 p - \frac{1}{c_s^2}\frac{\partial^2 p}{\partial t^2} = \nabla \cdot (\boldsymbol{J} \times \boldsymbol{B})$$

where p is the pressure in the medium and c_s is the speed of sound in the medium. When the pulser generates a voltage pulse across the electrodes, a current density proportional to the local apparent conductivity is induced in the sample. At interfaces of changing conductivity, the current density becomes discontinuous and so are the Lorentz forces acting on the currents. This gives rise to the source for the pressure wave in the above wave equation. In practice, this reverse mode may have some advantages in its lower noise level and its ability to use possible fast ultrasound imaging techniques for the image reconstruction (Wen *et al* 1998).

The HEI method has been shown to produce high resolution impedance images as used to image fat-muscle layers in a phantom made of bacon (Wen *et al* 1998, Grasland-Mongrain *et al* 2013). However, the use of surface electrodes for

applying/measuring an electrical field in HEI is limited by the shielding effect (Wen 2000).

2.11 MAT-MI

Magnetoacoustic tomography with magnetic induction (MAT-MI) is a technique proposed by Dr. Bin He and his colleagues. The method uses the magnetic field to generate the Lorentz force in the object, and so it is not affected by the "shielding effect" which is a factor in some of the other imaging techniques discussed earlier. A magnetic pulse $\boldsymbol{B_1}(\boldsymbol{r}, t)$ is applied to the object which induces an electric field $\boldsymbol{E}(\boldsymbol{r}, t)$ in the object. For a conductive sample, this gives rise to eddy currents $\boldsymbol{J}(\boldsymbol{r}, t) = \sigma(\boldsymbol{r})\boldsymbol{E}(\boldsymbol{r}, t)$ in the object. The magnetic pulse used in MAT-MI is generated using approximately microsecond long currents through coils which lead to magnetic fields with slow time variation such that the propagation time of the field through the object is negligible. This allows the magnetic induction problem in MAT-MI to be considered quasi-static. The skin depth of the corresponding MHz field in general biological tissue is at the level of meters which is much larger than the characteristic dimension of the object, so the magnetic diffusion can be ignored (Wand and Eisenberg 1994). This allows the applied magnetic field to be uniquely determined by the coil setup, which can be designed to penetrate uniformly into the object.

In addition, the microsecond long magnetic stimulation also leads to the displacement current being much weaker than the ohmic current due to the fact that $\sigma >> \omega\epsilon$ in biological tissue in the 1 MHz range (Xu and He 2005), where ω is the angular

frequency of the stimulating field and ϵ is the permittivity of the object. After applying the above approximations, the induced current in MAT-MI can be described by the following equations:

$$\begin{cases} \nabla \cdot \left(-\sigma \frac{\partial \boldsymbol{A}}{\partial t} - \sigma \nabla \phi\right) = 0 \; in \Omega \\ \boldsymbol{J} \cdot \mathbf{n} = 0 \text{ on } \partial\Omega \end{cases}$$

where Ω denotes the domain in which the object is present, $\boldsymbol{A}$ is the magnetic vector potential corresponding to magnetic stimulation $\boldsymbol{B_1} = \nabla \times \boldsymbol{A}, \nabla \cdot \boldsymbol{A} = 0$ and ϕ is the electrical scalar potential; n is the unit vector normal to the boundary surface $\partial\Omega$. The quasi-static condition in MAT-MI allows estimating the magnetic vector potential $\boldsymbol{A}$ directly from the configuration of the coils and the currents applied to them. For a known conductivity distribution σ and vector potential $\boldsymbol{A}$, the above magnetic induction problem can be solved in the domain Ω for the electric potential ϕ using the finite element method (FEM) simulations. The electric field can then be obtained as

$$\boldsymbol{E} = -\frac{\partial \boldsymbol{A}}{\partial t} - \nabla \phi$$

Now in the presence of a static magnetic field $\boldsymbol{B_0}$, the induced eddy current is subject to Lorentz force $\boldsymbol{J} \times \boldsymbol{B_0}$, and the time-varying Lorentz force gives rise to a traveling acoustic wave. In MAT-MI the divergence of the Lorenz force $\nabla \cdot (\boldsymbol{J} \times \boldsymbol{B_0})$ acts as the source of the acoustic wave. Now the static magnetic field $\boldsymbol{B_0}$ in MAT-MI is generated from external sources outside the conductive object, so its spatial distribution can be determined by the setup generating the magnetic field. The field from the permanent magnets used in the current study can be approximated to $\boldsymbol{B_o} = \mathrm{B}\,\hat{k}$, where B is a constant and $\hat{k}$ is the unit vector in the Z direction. This leads to $\nabla \times \boldsymbol{B_0}$ being

negligible inside the object space and the acoustic source can be further simplified as $\nabla \times (\boldsymbol{J}) \cdot \boldsymbol{B_0}$. Now, the induced eddy current $\boldsymbol{J}$ is a smooth function that vanishes outside the object space with its first derivative, so it can be decomposed into a rotational part $\boldsymbol{J_c}$ and an irrotational part $\nabla\theta$ (Joseph 2006). The current $\boldsymbol{J}$ can be written as:

$$\boldsymbol{J} = \boldsymbol{J_c} + \nabla\theta$$

Of these two components, the term $\boldsymbol{J_c}$ acts as the source for the acoustic wave, as $\nabla \times \boldsymbol{J} = \nabla \times \boldsymbol{J_c}$ **,** and the MAT-MI acoustic source can then be written as $\nabla \cdot (\boldsymbol{J_c} \times \boldsymbol{B_0})$. The generated acoustic waves can be described by the following equation (Roth *et al* 2004):

$$\nabla^2 p - \frac{1}{c_s^2}\frac{\partial^2 p}{\partial t^2} = \nabla \cdot (\boldsymbol{J_c} \times \boldsymbol{B_0})$$

where p is the pressure and c_s is the acoustic speed in the medium. The generated pressure wave is in the ultrasound frequency range due to the MHz magnetic pulse. This allows us to reconstruct the acoustic source distribution in the object using possible ultrasound imaging approaches. The conductivity distribution of the object can then be reconstructed from the obtained acoustic source map (Xu and He 2005, Li *et al* 2007).

Computer simulation and experiement studies have been performed with MAT-MI. The basic imaging theory and image reconstruction based on acoustic source estimation have been described in preliminary study (Xu and He 2005). Simulation studies with analytical solutions for the electromagnetic forward problem with simple spherical models (Li *et al* 2007) and finite element model based forward solver for complex geometry (Li *et al* 2008, Zhou *et al* 2011) have been performed to validate

MAT-MI based imaging. In addition to the acoustic source reconstruction based methods, vector source and potential energy based image reconstruction methods have also been developed and validated in computer simulations (Xia *et al* 2009, Xia *et al* 2010).

Experiment systems with a homemade, low power pulsed magnetic field have been used in preliminary MAT-MI studies for conductivity based imaging of saline gel phantoms and tissue phantoms (Li *et al* 2006, Xia *et al* 2007). In order to improve imaging quality, a commercial, high power magnetic pulser based system was used in imaging studies with low conductivity saline phantoms (< 1 S/m), biological tissue phantoms (Hu *et al* 2010) and ex-vivo human liver tumor imaging (Hu *et al* 2011). It is shown in these studies that using the single-excitation MAT-MI approach, we can non-invasively image the conductivity boundaries of tissue object with spatial resolution close to ultrasound imaging (Hu and He, 2011). In order to obtain stronger MAT-MI tissue signals, experiment systems using a high magnetic field from a magnetic resonance imaging (MRI) scanner for human study has been developed, which is shown to obtain the MAT-MI signal from conductivity boundaries in a single channel ultrasound data (Mariappan *et al* 2014). Further, we have developed an MAT-MI imaging system for performing small animal experiments using permanent magnets with a circular scanning setup around the object's space. This system is being used to currently perform imaging of hind limb tumors in a mouse model.

In order to obtain complete reconstruction of the object conductivity under the limited bandwidth imaging system available for MAT-MI, we use vector source imaging (Mariappan and He 2013, Mariappan *et al* 2014). In this method, the vector current

source which is more uniformly present throughout the object and gives rise to the MAT-MI pressure signal is reconstructed. This vector source is reliably estimated under practical experiment setup and the reconstructed vector field is then combined with the knowledge of the stimulating magnetic field to obtain the conductivity distribution in the object. Computer simulations and phantom experiments are performed to demonstrate conductivity reconstruction through vector source imaging in a circular scanning geometry with a limited bandwidth, finite size piston transducer. The results demonstrate that the MAT-MI approach is capable of conductivity reconstruction in a practical physical setting.

Chapter 3

Bio-impedance Contrast Imaging

3.1 Introduction

The MAT-MI pressure signal is generated by the Lorentz force acting on induced eddy currents. The acoustic source giving rise to the signals is determined by the divergence of the Lorentz force. In an object with variable conductivity this source is seen to be very strong at the conductivity boundaries where the Lorentz force changes rapidly. The measured ultrasound signal can be used to reconstruct the distribution of the acoustic source with high resolution reflective of the conductivity boundaries in the object. This is seen in the previous experiments and simulations performed on MAT-MI (Li *et al* 2006, Li *et al* 2007, Xia *et al* 2008, Hu *et al* 2010, Hu *et al* 2011). The acoustic source can then be further used to estimate the conductivity distribution of the object (Xu and He 2005, Li and He 2010). A reliable imaging of the acoustic source distribution from the measured transducer signal is desired in MAT-MI. Based on the forward modeling of the signal received at the transducer, two scanning setups with corresponding reconstruction algorithms are implemented for MAT-MI: the point receiver based system with scanning performed on a continuous aperture and a focused transducer based system with sector scan at discrete locations.

To evaluate different MAT-MI ultrasound system designs, we have developed a simulation protocol that can take into account different transducer designs and scan schemes for MAT-MI imaging. It is shown in our computer simulations that the conductivity boundary MAT-MI images are reliably reconstructed with the limited

bandwidth ultrasound setup. Also, as compared to the point receiver approach, the MAT-MI system using B-scan with a focused transducer allows MAT-MI imaging at a closer distance with improved system sensitivity using a discrete number of scanning locations which can greatly increases the applicability of the MAT-MI approach (Mariappan *et al* 2011).

We have performed experimental validation of the MAT-MI method using saline gel phantoms and biological tissue phantoms. We have also performed in-vivo validation studies using mouse tumor models. In addition, we have obtained increased MAT-MI tissue signals by using a high magnetic field from a magnetic resonance imaging (MRI) scanner for human study (Vaughan *et al* 2006) in combination with a high power magnetic pulse generator (Gang *et al* 2011). The testing results demonstrated our imaging system has the capability of providing MAT-MI high-resolution bioimepedance images (Mariappan *et al* 2013, Hu *et al* 2010, Hu *et al* 2011). Most materials in this chapter have been previously published (Mariappan *et al* 2011, Mariappan *et al* 2014).

3.2 MAT-MI Problem Description

In this section, we describe the forward and the inverse problem of MAT-MI. In the forward problem, the physical process by which eddy current is induced and the acoustic pressure is generated is described, and the equations governing the processes are derived. Image reconstruction methods from the obtained pressure signal are then described in the inverse problem of MAT-MI. In the first step of the inverse problem we describe the method of obtaining the acoustic source distribution which can be further

combined with the knowledge of the dynamic and the static magnetic fields to derive the conductivity distribution of the object.

3.2.1 Forward Problem

In MAT-MI a conductive object with an isotropic conductivity of $\sigma(\boldsymbol{r})$ is placed in the presence of a static magnetic field with flux density $\boldsymbol{B_0}(\boldsymbol{r})$, and a time varying magnetic pulse $\boldsymbol{B_1}(\boldsymbol{r},t)$ is applied to the object. This magnetic field induces an electric field $\boldsymbol{E}(\boldsymbol{r},t)$ in the object which for a conductive sample gives rise to eddy currents $\boldsymbol{J}(\boldsymbol{r},t)=\sigma(\boldsymbol{r})\boldsymbol{E}(\boldsymbol{r},t)$ in the object.

The magnetic pulse used in MAT-MI is generated using approximately microsecond long currents through coils which lead to magnetic fields with slow time variation such that the propagation time of the field through the object is negligible. This allows the magnetic induction problem in MAT-MI to be considered as quasi-static. The skin depth of the corresponding MHz field in general biological tissue is at the level of meters which is much larger than the characteristic dimension of the object, so the magnetic diffusion can be ignored (Wang and Eisenberg 1994). This allows the applied magnetic field to be uniquely determined by the coil setup and the separation of the spatial and temporal functions in the electromagnetic field analysis of MAT-MI as in $\boldsymbol{B_1}(\boldsymbol{r},t)=\boldsymbol{B_1}(\boldsymbol{r})f(t),\ \boldsymbol{E}(\boldsymbol{r},t)=\boldsymbol{E}(\boldsymbol{r})f'(t)$ where the prime indicates first derivative. In addition to this, the microsecond long magnetic stimulation also leads to the displacement current being much weaker than the ohmic current due to the fact that $\sigma>>\omega\epsilon$ in biological tissue in the 1 MHz range (Xu and He 2005), where ω is the angular

frequency of the stimulating field and ϵ is the permittivity of the object. Therefore, the tissue capacitance effect is ignored here and only conductivity of the tissue is considered.

According to Faraday's law, the curl of the electrical field is: $\nabla \times \boldsymbol{E}(\boldsymbol{r}, t) = -\frac{\partial \boldsymbol{B_1}}{\partial t}$. Considering the magnetic vector potential $\boldsymbol{A}$ corresponds to magnetic stimulation $\boldsymbol{B_1} = \nabla \times \boldsymbol{A}, \nabla \cdot \boldsymbol{A} = 0$ would lead to $\nabla \times \left(\boldsymbol{E} + \frac{\partial \boldsymbol{A}}{\partial t}\right) = \boldsymbol{0}$. The electric field can then be described as:

$$\boldsymbol{E} = -\frac{\partial \boldsymbol{A}}{\partial t} - \nabla \phi \tag{3.1}$$

where $\phi(\boldsymbol{r}, t)$ is the electrical scalar potential. The induced current density can then be obtained from Ampere's law as $\boldsymbol{J} = \sigma \boldsymbol{E}$.

Now according to the continuity, equation

$$\nabla \cdot (\boldsymbol{J}) = 0 \tag{3.2}$$

This allows for the induced current in MAT-MI to be described by the following equations:

$$\begin{cases} \nabla \cdot \left(-\sigma \frac{\partial \boldsymbol{A}}{\partial t} - \sigma \nabla \phi\right) = 0 \ \ in \ \ \Omega \\ \boldsymbol{J} \cdot \mathbf{n} = 0 \text{ on } \partial\Omega \end{cases} \tag{3.3}$$

where Ω denotes the domain in which the object is present, $\mathbf{n}$ is the unit vector normal to the boundary surface $\partial\Omega$. The quasi-static condition in MAT-MI allows estimating the magnetic vector potential $\boldsymbol{A}$ directly from the configuration of the coils and the currents applied to them. For a known conductivity distribution σ and vector potential $\boldsymbol{A}$ the above magnetic induction problem can be solved in the domain Ω for the electric

potential ϕ using the finite element method (FEM) simulations, and the electric field can be obtained according to equation 3.1.

Now, in the presence of a static magnetic field $\boldsymbol{B_0}$ the induced eddy current is subject to Lorentz force $\boldsymbol{J} \times \boldsymbol{B_0}$ and the time-varying Lorentz force gives rise to a traveling acoustic wave. In MAT-MI the divergence of the Lorenz force $\nabla \cdot (\boldsymbol{J} \times \boldsymbol{B_0})$ acts as the source of the acoustic wave. Now the static magnetic field $\boldsymbol{B_0}$ in MAT-MI is generated from external sources outside the conductive object, so its spatial distribution can be determined by the setup generating the magnetic field. The field from the permanent magnets used in the current study can be approximated to $\boldsymbol{B_o} = \mathrm{B}\,\hat{k}$, where B is a constant and $\hat{k}$ is the unit vector in the Z direction. This leads to $\nabla \times \boldsymbol{B_0}$ being negligible inside the object space and the acoustic source can be further simplified as $\nabla \times (\boldsymbol{J}) \cdot \boldsymbol{B_0}$. Now, the induced eddy current $\boldsymbol{J}$ is a smooth function that vanishes outside the object space with its first derivative, so it can be decomposed into a rotational part $\boldsymbol{J_c}$ and an irrotational part $\nabla\theta$ (Joseph 2006). The current $\boldsymbol{J}$ can be written as:

$$\boldsymbol{J} = \boldsymbol{J_c} + \nabla\theta \tag{3.4}$$

Of these two components, the term $\boldsymbol{J_c}$ acts as the source for the acoustic wave, as $\nabla \times \boldsymbol{J} = \nabla \times \boldsymbol{J_c}$ and the MAT-MI acoustic source can then be written as $\nabla \cdot (\boldsymbol{J_c} \times \boldsymbol{B_0})$. The generated acoustic waves can be described by the following equation (Roth *et al* 1994, Xu and He 2005):

$$\nabla^2 p - \frac{1}{c_s^2}\frac{\partial^2 p}{\partial t^2} = \nabla \cdot (\boldsymbol{J} \times \boldsymbol{B_0}) = \nabla \cdot (\boldsymbol{J_c} \times \boldsymbol{B_0}) \tag{3.5}$$

where p is the pressure and c_s is the acoustic speed in the medium.

Suppose the induced eddy currents are confined to the object space Ω. The acoustic source is then zero outside the conductive object. Now the detected acoustic pressure $p(\boldsymbol{r}, t)$ on the scanning aperture can be obtained using Green's function solution to the wave equation as follows (Xu and He 2005):

$$p(\boldsymbol{r}, t) = -\frac{1}{4\pi} \iiint d^3 r' \nabla_{r'} \cdot \left(\boldsymbol{J_c}(\boldsymbol{r}') \times \boldsymbol{B_0}(\boldsymbol{r}') \right) G(\boldsymbol{r}, \boldsymbol{r}', t) \tag{3.6}$$

where $\boldsymbol{r}'$ is the location of the acoustic source, $\boldsymbol{r}$ is the location of the detector, $\nabla_{r'}$ implies derivative with respect to source space $\boldsymbol{r}'$, the Green's function for this solution $G(\boldsymbol{r}, \boldsymbol{r}', t) = \frac{\delta\left(t - \frac{R}{c_s}\right)}{R}$ where $R = |\boldsymbol{r} - \boldsymbol{r}'|$. The volume integration is carried out over the acoustic source distribution in the object space Ω. This equation gives the observed pressure for an impulse source i.e. a source with its time function as $\delta(t)$. An induced acoustic source field with time dependence $h(t)$ gives an observed pressure $p(\boldsymbol{r}, t) \otimes h(t)$, where $\otimes$ is the convolution operator. The Green's function for this time dependence can be written as: $G(\boldsymbol{r}, \boldsymbol{r}', t) = \frac{h\left(t - \frac{R}{c_s}\right)}{R}$ (Mariappan *et al* 2011).

3.2.2 Inverse Problem Description

The image reconstruction algorithm for MAT-MI can be broken into two steps. In the first step the acoustic source distribution is obtained, and in the second step this acoustic source is used to estimate the conductivity of the object. For an impulse source, i.e. $\boldsymbol{J}(\boldsymbol{r}, t) = \boldsymbol{J}(\boldsymbol{r})\delta(t)$, the pressure in the object is zero before time zero which on integrating equation 3.5 from $(-\infty, 0+)$ leads to (Xu and He 2005):

$$-\frac{1}{c_s^2} \frac{\partial p}{\partial t}\Big|_{0+} = \nabla \cdot (\boldsymbol{J} \times \boldsymbol{B_0}) \tag{3.7}$$

So, determining $-\frac{1}{c_s^2}\frac{\partial p}{\partial t}\Big|_{0+}$ in the object would lead to determining the MAT-MI source distribution. For this, an ultrasound imaging system is used which consists of transducers placed around the object collecting the generated MAT-MI acoustic wave. Depending on the ultrasound scanning system used, different image reconstruction algorithms can be applied. Two algorithms implemented to image the acoustic source, $\nabla \cdot (\boldsymbol{J} \times \boldsymbol{B_0})$, for MAT-MI are described in the following sections.

3.2.3 Point receiver based system

The signal pressure received by an ideal point receiver is described in equation 3.6. With such a receiver collecting pressure signal on an aperture enclosing the object ($\sum$) in an acoustically homogeneous medium, the initial pressure distribution can be determined by time reversing the acoustic waves (Xu and Wang 2004a) as:

$$p'(r, 0+) \approx \frac{1}{2\pi c_s} \iint_{\sum} dS_d \boldsymbol{n} \cdot \frac{\boldsymbol{r_d} - \boldsymbol{r}}{|r_d - r|^2}\, p''(\boldsymbol{r_d}, |r_d - r|/c_s) \tag{3.8}$$

where $\boldsymbol{r_d}$ is a point on the detection surface, $\boldsymbol{r}$ is a point in the object space, and the single and double prime represent the first and second derivative over time, respectively. In this equation a term corresponding to the first derivative is neglected as its contribution is negligible compared to the second derivative term.

This initial pressure derivative can be substituted into equation 3.7 to reconstruct the MAT-MI source distribution.

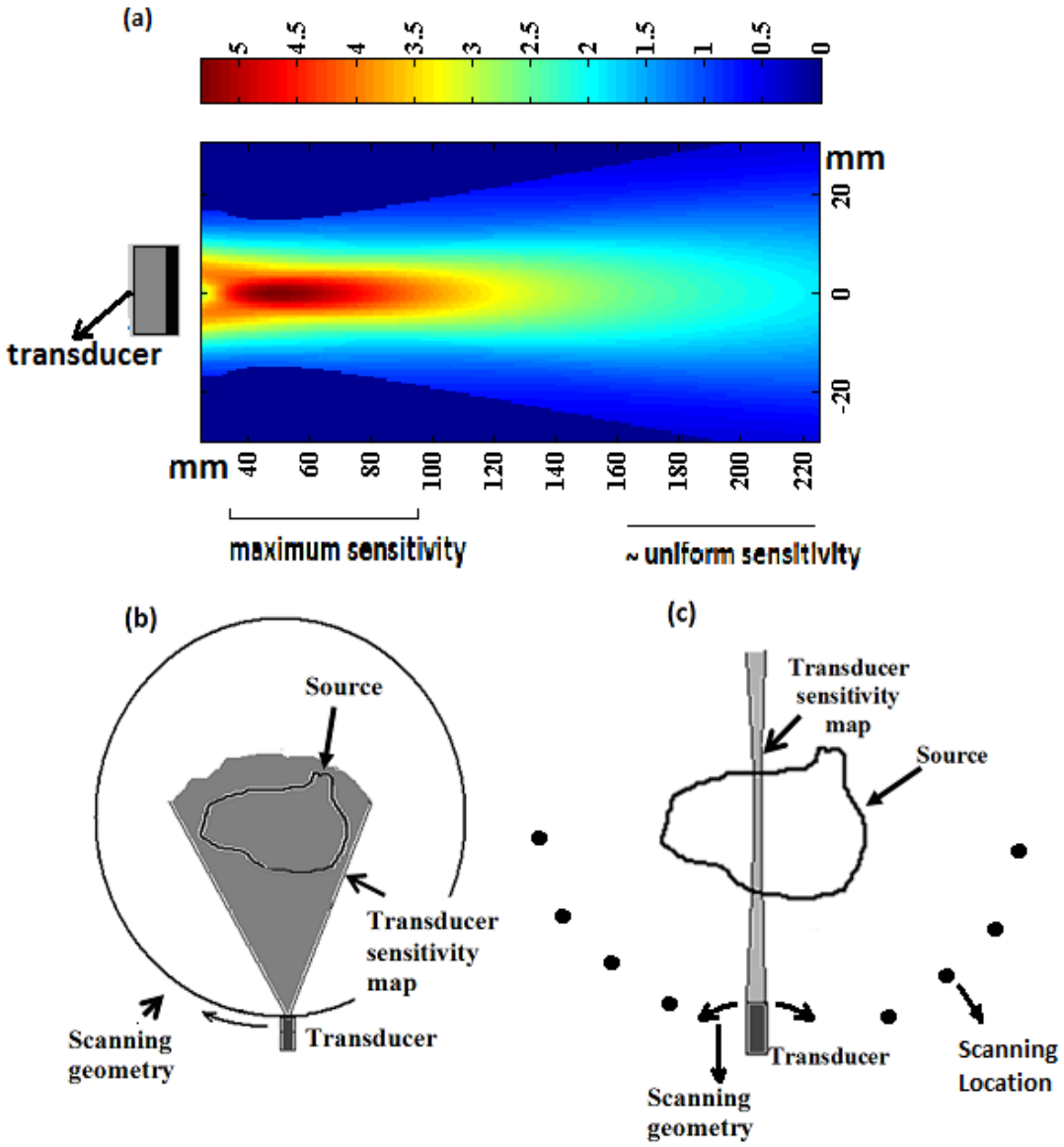

Fig. 3, (a) Sensitivity map of a piston transducer (b)-(c) Schematic of image reconstruction schemes for MAT-MI for a given transducer and source distribution (b) Point receiver with scanning around the object (c) Sector-Scan with focus transducer and scanning at different locations around the object

3.2.4Focus transducer based system

The acoustic source imaging using a point receiver based method requires an ideal point sized sensor which has very low sensitivity due to the size of the aperture. Therefore, in MAT-MI imaging systems, a point receiver is implemented with a piston transducer of finite aperture size. The omnidirectional nature of the point receiver is achieved by placing the object in a region of approximately uniform sensitivity as shown in figure 3(a). However, as seen in this figure, to obtain the uniform sensitivity, it requires the object to be placed at a relatively large distance away from the transducer and also away from its maximum sensitivity region. The transducer is scanned around the object, forming a continuous aperture for image reconstruction (Xu and He 2005, Li *et al* 2006, Li *et al* 2007) as shown in figure 3(b). Other techniques of acoustic source imaging using virtual point detectors with scanning around the object have been tried out for photoacoustic tomography (PAT). These methods like using a large numerical aperture transducer (Li and Wang 2008) or a negative lens (Li *et al* 2008) have been proposed to improve the sensitivity of the receiver and shorten the scanning radius. These techniques are based on virtual point detectors; however, much like the piston transducer acting as a point receiver, they need scanning to be done on a continuous aperture around the object. In this section, we will describe the use of the focus region of a transducer with B mode scan scheme to reconstruct the MAT-MI ultrasound source distribution (Mariappan *et al* 2011). The focus region of a transducer has the maximum sensitivity as seen in figure 3(a). Utilizing such kind of focus region, the transducer receives signal generated mainly from sources in a relatively narrow beam region along its acoustic axis. These sources are

time resolved in the collected signal due to time of flight difference to the transducer. The signal obtained is backprojected to reconstruct acoustic sources in the beam region. However, the signal received from a smoothly distributed acoustic source is the strongest when the transducer axis is perpendicular to the source distribution (Xu *et al* 2001, Xu *et al* 2004). Therefore, to obtain a complete image of the MAT-MI sources, we need to set the transducer facing various edges of the source distribution. This is achieved by rotating the transducer at a location to scan along various lines through the object. This is then repeated at a number of locations around the object for complete image reconstruction, and only a discrete number of scanning locations around the object are needed. This kind of scanning scheme is shown in figure 3(c). This scanning scheme is denoted here as the B-Scan based method.

3.2.4.1 B-Scan Image Reconstruction

The signal received at the ultrasound transducer with a finite aperture size can be described as follows:

$$p_{tr}(\boldsymbol{r},t) = \iint_{\substack{transducer\\surface}} p(\boldsymbol{r},t)\, dxdy \tag{3.9}$$

On combining (3.6) and (3.9), we can get

$$p_{tr}(\boldsymbol{r},t) = -\frac{1}{4\pi}\iiint d^3r'\nabla_{r'}\cdot\left(\boldsymbol{J_c}(\boldsymbol{r'})\times\boldsymbol{B_0}(\boldsymbol{r'})\right)\iint_{\substack{transducer\\surface}} G(\boldsymbol{r},\boldsymbol{r'},t)\, dxdy$$

Here we can define the term $h_r(\boldsymbol{r'},t)$ as follows

$$h_r(\boldsymbol{r'},t) = \iint_{\substack{transducer\\surface}} G(\boldsymbol{r},\boldsymbol{r'},t)\, dxdy \tag{3.10}$$

This is the spatial impulse response of the transducer located at position *r*, and it is a characteristic of the transducer's geometry. The effect of the electromechanical impulse response of the transducer $e(t)$ and the temporal waveform of the induced acoustic fields $f(t)$ on the obtained pressure signal can be accounted for in the forward computation by convolving the spatial impulse response with these waveforms $h_r(r', t) \otimes e(t) \otimes f(t)$.

The shape of the transducer can be designed in such a way that the spatial impulse response of the transducer is sensitive towards a limited region of the acoustic source distribution. The gain map of such a transducer capable of focusing on a certain region of the object is shown in figure 4.

The acoustic source reconstruction using the focused transducer can be done using the B-Scan method which involves backprojecting the signal along the focus of the transducer. This gives a 1D image of the object also known as a B-scan. The transducer is then rotated at the location to face various lines through the object. The entire angle over which the transducer is rotated is fixed to cover the object dimensions. The individual 1D images obtained at different angles during the rotation are added up and this gives a sector scan image. To obtain a complete image, sector scan images are collected at a number of locations around the object and are added up to form the final image. This is called a compound scan. This scheme of scanning ensures that the transducer faces the various edges in the object and gives a complete reconstruction of the acoustic source distribution.

While forming those 1D images with backprojection it is assumed that the transducer beam is a narrow 1D line. However the actual transducer has a finite beam width as seen in figure 4 which is generally termed the "directivity" of the transducer. Taking this into account, a simplified backprojection process for estimating the acoustic source can be described by the following equation:

$$A(\boldsymbol{r}') = \sum_{\substack{transducer \\ locations}} g_n(R) p_{tr}''(r, t_R) \tag{3.11}$$

The term $g_n(R)$ accounts for the effect of the transducer's directivity and acts as weighting term to maintain a uniform quality throughout the image (Xu *et al* 2001), where $R = |\boldsymbol{r} - \boldsymbol{r}'|$, $\boldsymbol{r}$ is the location of the transducer and $\boldsymbol{r}'$ is the location of the acoustic source. The term $g_n(R)$ is determined by the strength of the transducer's spatial impulse response $h_r(r', t)$ at time t_R, where t_R is the time at which the signal from the source location arrives at the transducer. For the current work, the directivity has been obtained from simulations of the transducer's spatial impulse response. The imaging algorithm described by (3.11) can be used to determine the point spread function (PSF) of the system. The reconstructed image is the convolution of the acoustic source and the system PSF. Therefore, the PSF determines the imaging quality, and the predicted PSF can be used to filter the image to improve the accuracy of the reconstruction.

We can use 2D Fourier filtering to improve the accuracy of the acoustic source reconstruction as described by the following equation:

$$I_k' = I_k \cdot \frac{d_k^*}{|d_k|^2 + \beta} \tag{3.12}$$

where I_k' , I_k and d_k are the 2D FFT of the filtered image, reconstructed image and the PSF. The term β is a regularization parameter to reduce the effect of noise during filtering and is determined based on SNR considerations. The filtered image is obtained as the 2D inverse Fourier transform of I_k'.

3.3 Computer Simulation Study

To evaluate different MAT-MI system designs, we have developed a simulation protocol that can take into account different transducer designs and scanning schemes for MAT-MI imaging.

The MAT-MI acoustic source is the divergence of the Lorentz force ($\nabla \cdot (\boldsymbol{J} \times \boldsymbol{B_0})$), and it depends on the variation of the induced eddy current in the object. This leads to a strong MAT-MI acoustic source at the conductivity boundaries due to a big variation in the induced current from the conductivity change at all these boundaries. This has been observed in experiments and previous simulation studies (Li *et al* 2006, Li *et al* 2007, Xia *et al* 2007). In the current study, FEM simulations using COMSOL software were used to determine the induced eddy current densities in the object. The static and dynamic magnetic fields are assumed to be uniform over the entire object, and the corresponding acoustic sources obtained from the simulation are also observed to be the strongest at the conductivity boundaries. Thus, in this study of various ultrasound scanning methods, the MAT-MI acoustic source is assumed to be only from conductivity boundaries in the object.

Ultrasonic imaging simulations were performed with Field II software (Jensen and Svendsen 1992). The software allows defining transducers of various geometries. The spatial impulse response of the transducer is calculated in the software by breaking the transducer's surface into smaller elements. The program also allows simulating the transducer's electromechanical impulse response. In the current simulations this is set to the experimentally measured electromechanical impulse response of the transducer obtained with a wide band hydrophone.

B-scan imaging simulations are performed with a 500 KHz, 4 cm diameter concave transducer with a 5.5 cm focus. For comparison, a piston transducer with 500 KHz central frequency and 2 cm diameter is also used in our simulation study. The piston transducer can be used for the two imaging techniques, namely the point receiver and the B-Scan based method. The gain map of this transducer in the focus region is shown in figure 4(b). The concave transducer is a larger focus transducer and has a narrower, stronger beam as compared to the piston transducer as seen in figure 4(a). This gives a better spatial resolution and improved sensitivity of 4 times while imaging with the B-scan method as seen from the color bars for the gain maps in figure 4. The concave transducer simulated here has a beam length of about 4-5 cm around a focal length of 5.5 cm. So an object space of 4 cm by 4 cm is used in the present simulation study, and the locations at which the sector scans for the compound scan are performed are 5.5 cm away from the center of the object space. The bandwidth of both of the transducers is around 60% of their centre frequency (500 kHz).

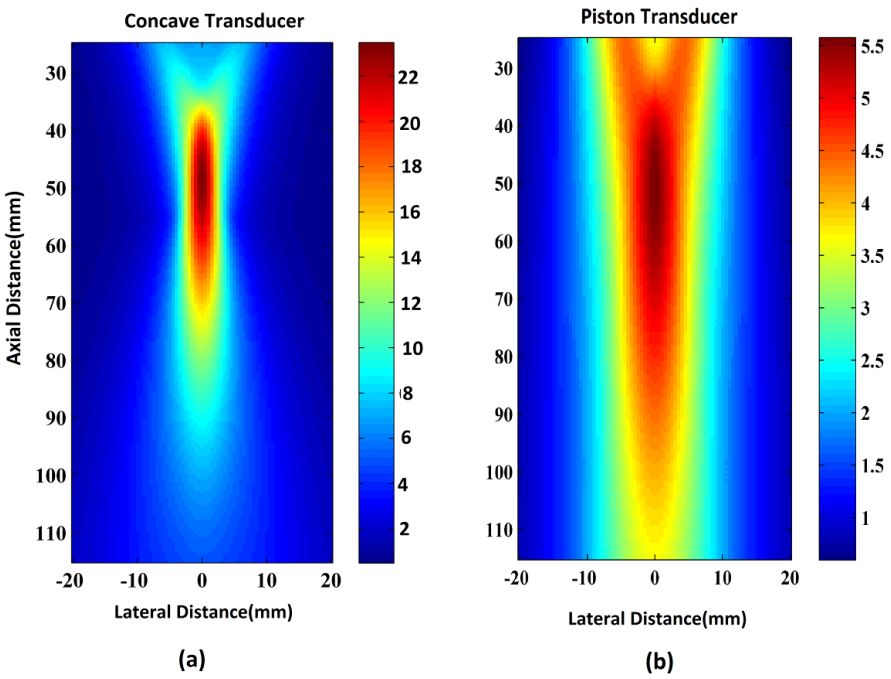

Fig 4 (a) Gain map of a concave transducer (b) Gain map of a piston transducer

The received pressure signal is computed according to (3.9). At a given transducer location, the spatial impulse response is computed at each source location. The received signal is then obtained by adding up the spatial impulse response multiplied with the source amplitude. This process is then repeated for each transducer orientation and location employed in the compound scan.

The image reconstruction is done by using (3.11). In the current compound scan scheme, a 180 degree view angle (Xu *et al* 2004) around the object is used. This gives a complete image reconstruction. The resolution of the reconstruction is about 3-4 mm at 500 kHz transducer frequency with a 60% bandwidth (Li *et al* 2006).

3.4 B-Scan Image Reconstruction

A simulation example is shown in figure 5. An object of 2 concentric circles with inner circle conductivity of 0.6 S/m and outer circle conductivity of 0.3 S/m in a background of 0 S/m is imaged in this simulation. The induced current density is obtained with FEM simulations using COMSOL software. This is then used to compute the acoustic source distribution which is shown in figure 5(b). As it can be seen here the acoustic source is strongest at the conductivity boundaries.

The acoustic source distribution is used to compute the signal received at the transducer. A typical signal received with the concave transducer 5.5 cm from the origin is seen here in figure 5(c). In this case, the transducer's acoustic axis passes through the

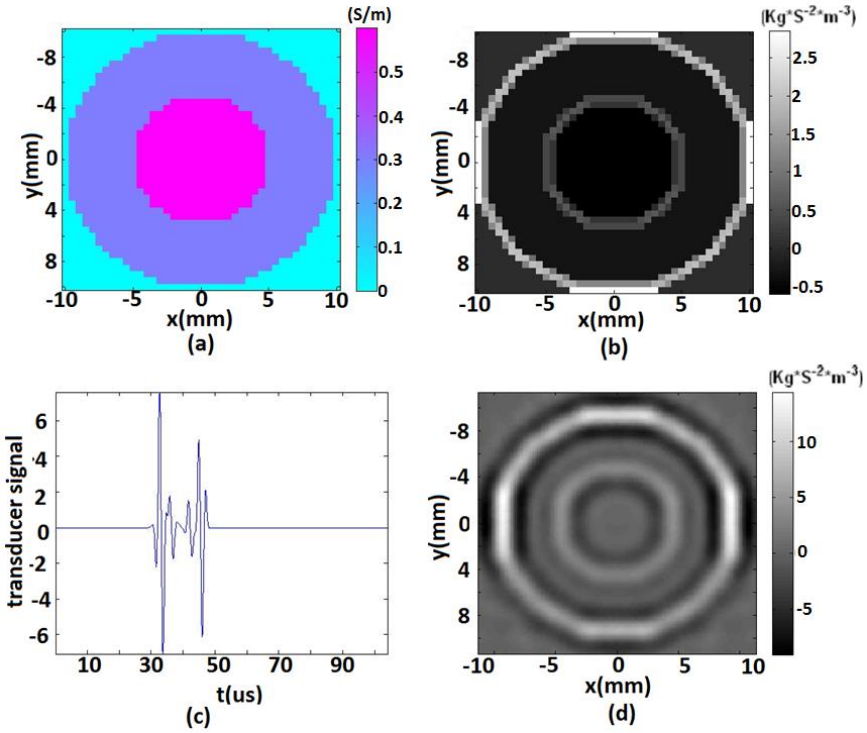

Fig. 5, (a) Object conductivity distribution (b) Simulated acoustic source (c) Simulated signal received at the transducer (d) Reconstructed acoustic source distribution

object's center and the four pulses seen in the received signal correspond to the four object boundaries. The signal obtained at various transducer locations as described in the scanning scheme are then used to reconstruct the acoustic sources as described in section 2.2. The bandwidth used in the simulation is around 300 kHz. This results in an image resolution of about 3-4mm which leads to a thicker boundary after reconstruction. Figure 6(a-c) shows the sector scan image from locations at 0,35 and 55 degress and as seen here the acoustic sources parallel to the transducer direction is imaged. The complete object reconstruction with compound scan is seen in figure 6(d).

The acoustic source reconstruction results in the presence of noise are shown in

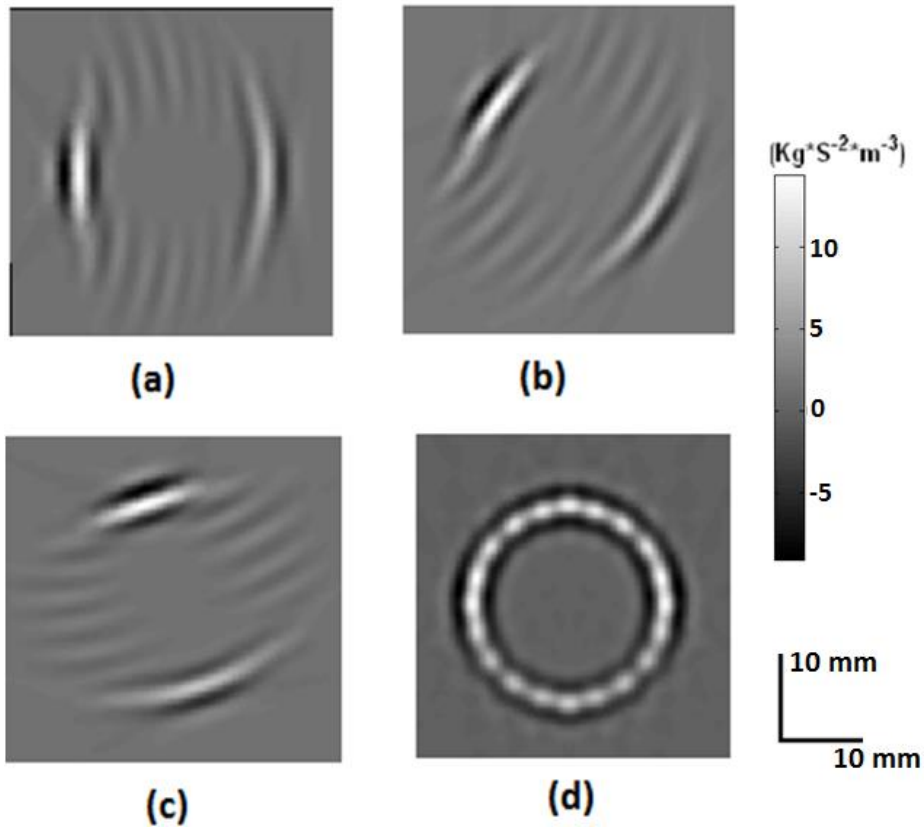

Fig. 6, Image reconstruction of a 1 cm circular object (a)-(c) Sector scans at 0, 35, 55 degrees, respectively (d) Compound scan image obtained by adding all the individual sector scans

figure 7. Two target acoustic source distributions are shown in figure 7(a). Image reconstruction with varying SNR is shown in figure 7(b)-(d), the maximum SNRs of the scans used in each of the compound scan images shown here are fixed at 10, 5 and 2, respectively.

The simulation method can also be used to predict the point spread function (PSF) of the reconstruction scheme, and this kind of PSF can be used to filter the image to give a more accurate reconstruction. This is seen in figure 8 where the number of transducer locations used for reconstruction is reduced from 11 sector scans which give a complete reconstruction to 6 and 4 sector scans. The resultant point spread functions for these different numbers of scanning locations are shown in figure 8(a), and these PSFs can be

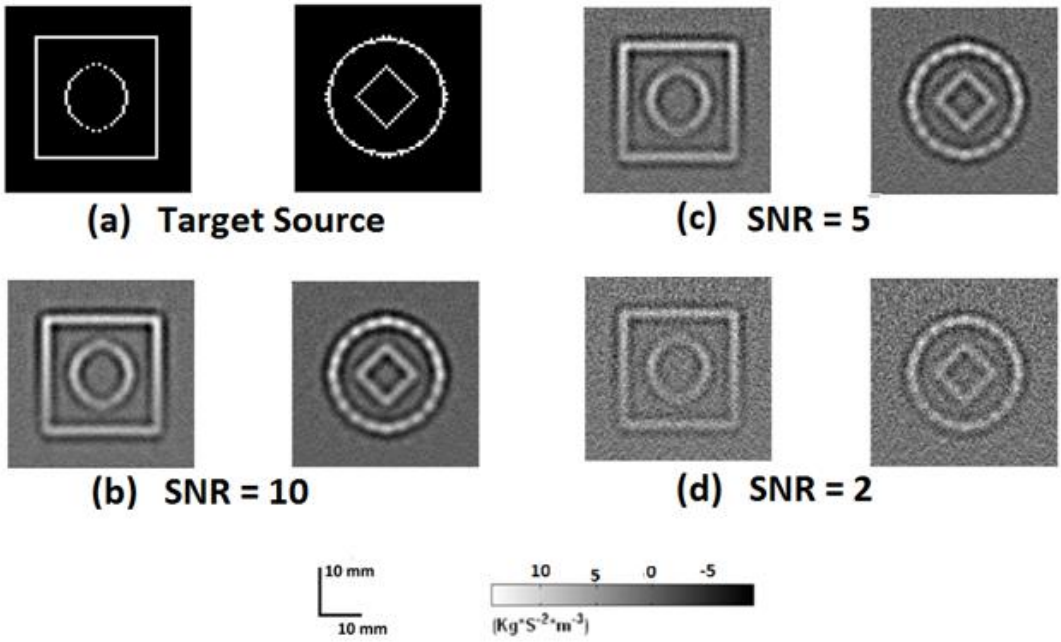

Fig. 7, (a) Target source (b)-(d) Reconstructed source distribution (b) SNR=10 (d) SNR=5 (d) SNR=2

used to filter the reconstructed images. We have used a 2D Fourier filter for the images, filtering as described previously. However, the filtering process is very sensitive to errors in the reconstructed image (Wan *et al* 2009). So to reduce the effect of noise in the filtered image we have used the PSF from 11 sector scans as target PSF. The filtered images show a better reconstruction of the target source distribution as shown in figure 8.

As mentioned in section 3.2.2, we have used a continuous scanning scheme using a point receiver in a previous MAT-MI system and we have also implemented a

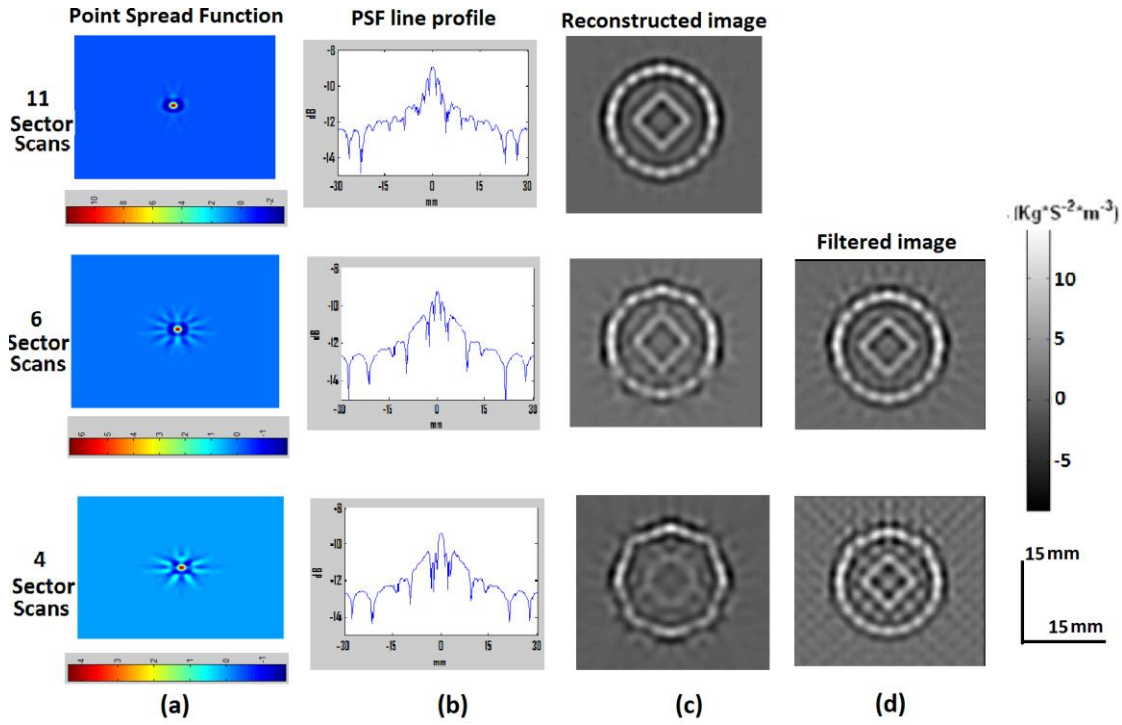

Fig. 8, Images reconstructed with compound scan. The three rows from top to bottom correspond to 11, 6 and 4 sector scans in the compound scan. (a) Point spread function for each scanning scheme (b) A line profile from the PSF (c) Reconstructed image (d) PSF filtered image

compound scan scheme. We have compared these two scanning methods in computer simulations. For comparison, we have used the same piston transducer for image reconstruction. The region at the transition from near field to far field provides certain focussing of the piston transducer as seen in figure 3(a), and this region is used for the compound scan scheme. The piston transducer gives a uniform sensitivity at a farther distance as described above and can act as a point receiver. We have compared in simulation the distance required for accurate image reconstruction using the two methods and the resultant SNR of the reconstructed images. As shown in figure 9, square acoustic sources of 1, 2 and 4 cm are used for this testing. Image reconstructions using the point receiver method with a scanning radius of 5.5 cm, 10 cm and 20 cm are compared with those using the compound scan method with a scanning radius of 5.5 cm, which equals the transducer's focal length. Equal noise is added to each received signal with the highest SNR in the data being 5 and 200 scan lines being used with each reconstruction. For each of the sources the image reconstructed with various scanning distances is shown in the figure. It can be seen in the figure that the point receiver method reconstructs the 1 cm square at all three scanning radii, and as the size of square increases to 4 cm a complete reconstruction is obtained only at scanning distance around 20 cm. The compound scanning method on the other hand reconstructs the sources at a 5.5 cm scanning radius. As expected, because the point receiver method requires a uniform gain for image reconstruction, at a closer distance only smaller objects get completely reconstructed. To completely image a larger object with the size of 2-4 cm, the transducer has to be placed around 10-20 cm away from the imaging center which will inevitably

reduce the sensitivity of the receiver. This can be seen in figure 9 where the complete image reconstruction with point receiver scheme at 20 cm has the lowest image SNR. In comparison, with the compound scan, the most sensitive region of the transducer's spatial gain map is used while a complete image reconstruction can still be obtained. As shown in figure 9, the resultant SNR using the compound scan is much better compared to the point receiver scheme.

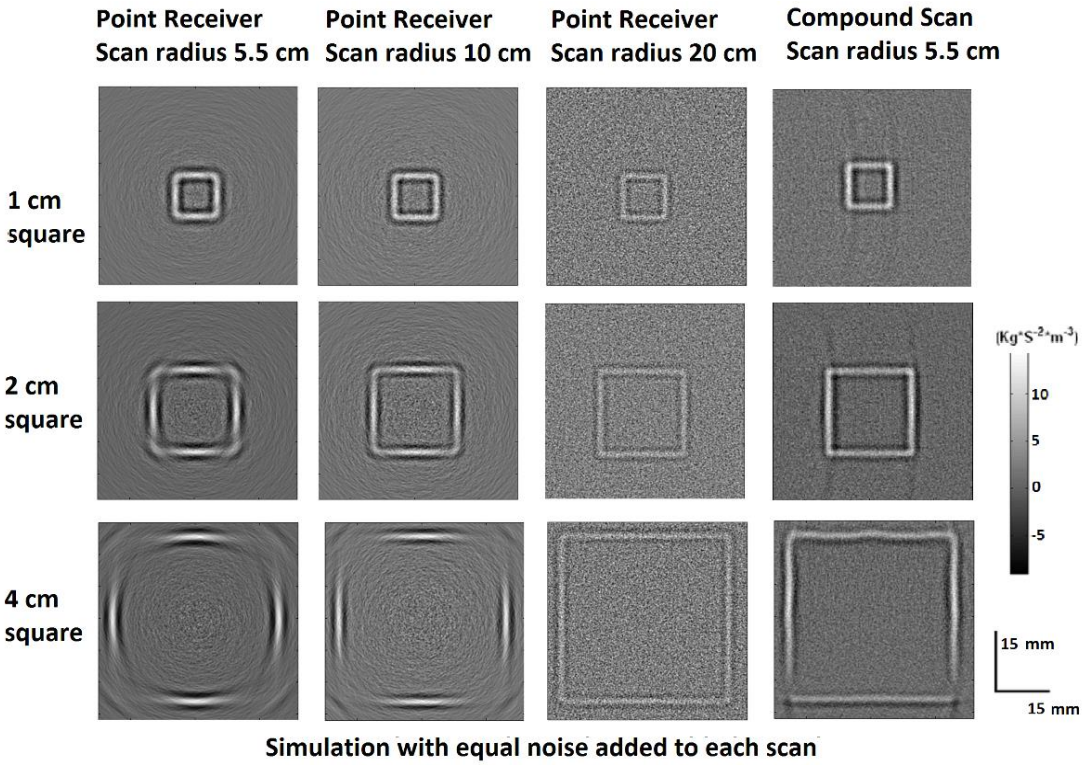

Fig. 9, Images of reconstructed source distributed along a square. Each column from left to right corresponds to either different scanning method or different scanning distance. Each row from top to bottom corresponds to the square imaging object of size 1cm, 2cm and 4 cm. Equal noise was added to the acoustic signals in each scan.

3.5 B-Scan Experiment

We have also evaluated the proposed method in MAT-MI experiments. The experimental setup consists of two permanent magnets used like a Helmholtz pair to get an approximately uniform magnetic field of 0.2T between them. A pair of coils again in Helmholtz configuration are used to generate the dynamic magnetic field. The coil is driven by a current source generating one cycle of sine wave at each pulse. A Gage CompuScope AD converter is used for data acquisition. The transducer signal is amplified by 90 dB and sampled at 10 MHz. The transducers for the current experiments are from Panametrics (center frequency 1 MHz, 9 cm focal length, 4.5cm diameter). The

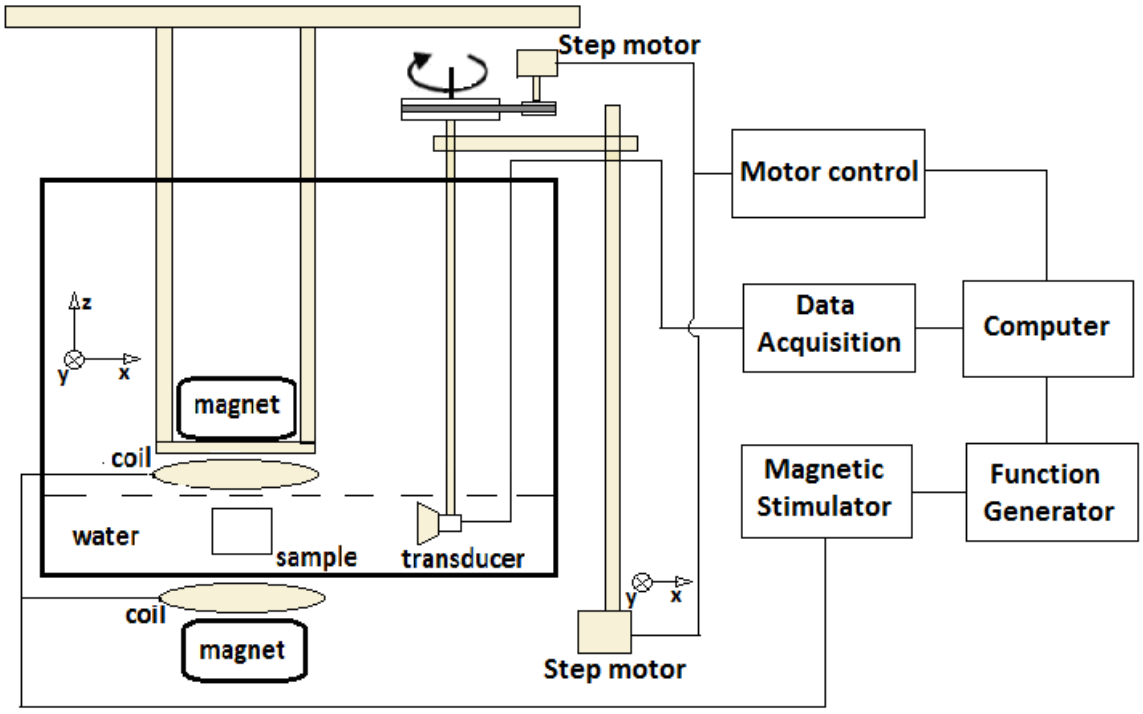

Fig. 10, Schematic diagram of present experiment system

phantom and the transducer are immersed in water for better ultrasound coupling. The signal is averaged 2000 times to improve the SNR. The scanning stage consists of 4 stepper motors capable of moving along x, y and z directions and also rotating the transducer to a desired angle. The schematic diagram of the setup is shown in figure 10.

The backprojection method as described in section 2.2 is used for image reconstruction. In the experiment system, noise degrades the final reconstruction, and the noise unlike the signal from an acoustic source adds up incoherently during the backprojection process. This can be suppressed by multiplying the image with a coherence factor (CF) (Liao *et al* 2004) given by

$$CF = \frac{\left|\sum_{f=1}^{N} I_f\right|^2}{N\sum_{f=1}^{N}\left|I_f\right|^2} \tag{3.13}$$

where I_f is a B-scan image added in the final compound scan and N is the total number of B-scans. The numerator represents the total coherent energy at a point; the denominator denotes the total incoherent energy. At points in the image other than the source location where incoherent noise dominates, the denominator is much larger than the numerator thus suppressing the noise.

Phantoms made of pork skin gel have been used in these experiments. In the first experiment we use a phantom consisting of an approximately 2cm square gel block of 10% salinity embedded in a 0% gel. As shown in figure 11, the directional nature of the MAT-MI sources can be seen in the reconstruction with the transducers facing only one side of the object and only reconstructing the edge parallel to it. In the reconstructed

image, a coherence factor (CF) weighting is seen to suppress the incoherent noise in the received signal from affecting the image reconstruction as seen in figure 11(a) and 11(b). The experiment result is also compared with simulation result as in figure 11(c) and a one to one correspondence can be seen between the experiment and the simulation.

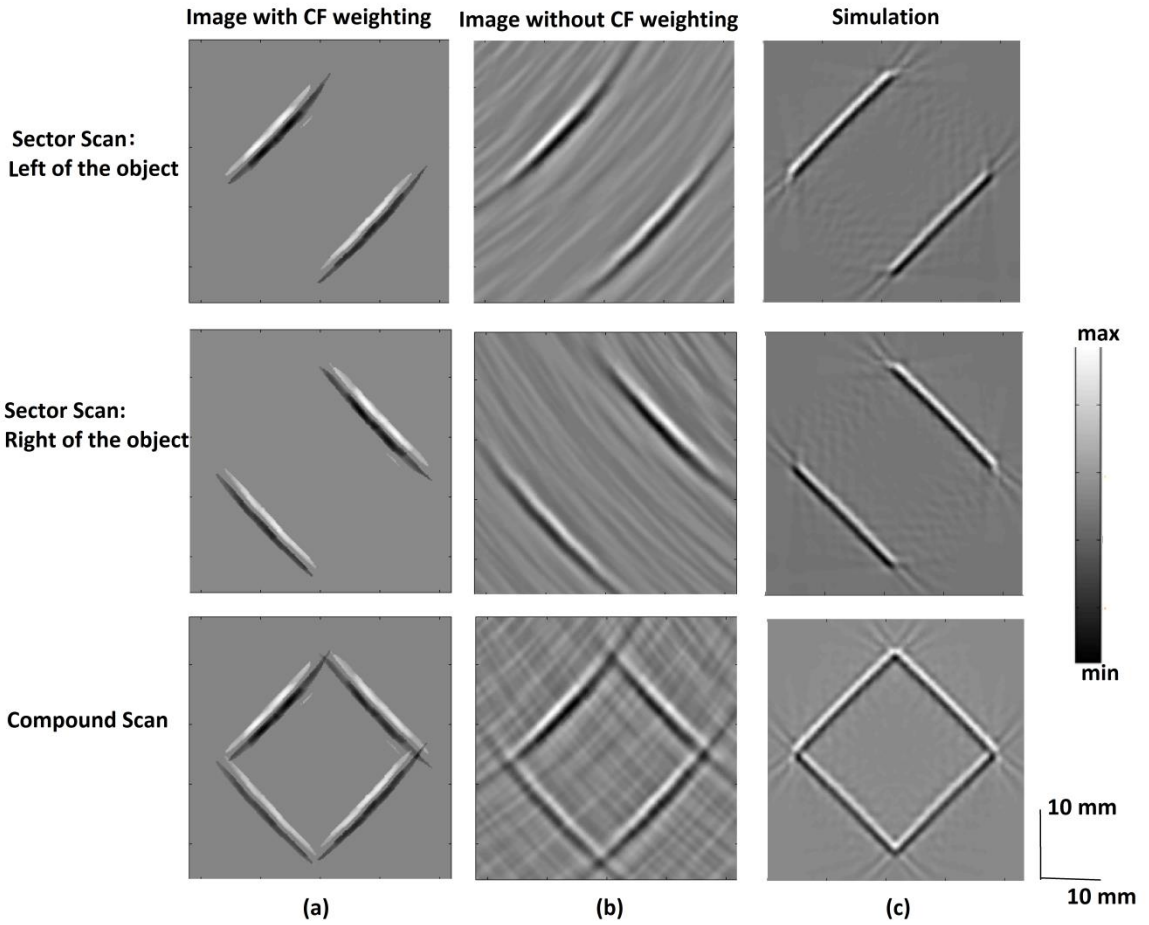

Fig. 11, (a)-(c) Each row from top to bottom corresponds to image reconstructed by using experimental sector scan data on the right, left of a square gel object and all the sector scans, respectively. (a) Reconstructed images with CF weighting (b) Reconstruction without CF weighting (c) Simulation

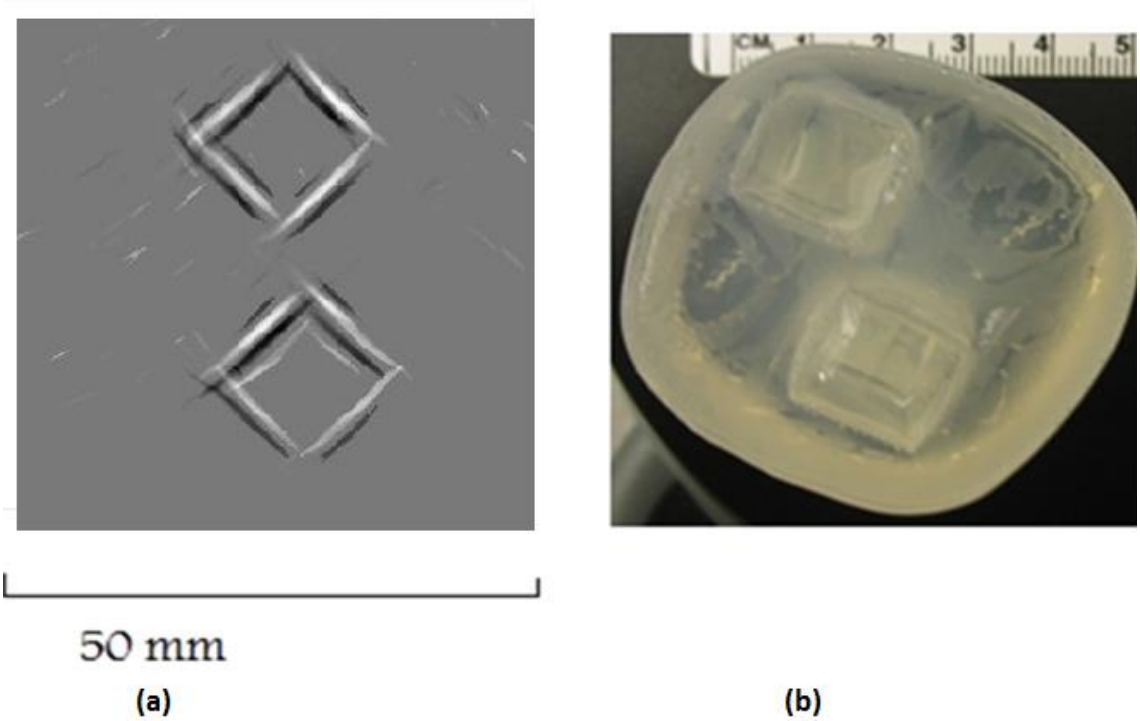

Fig. 12, (a) MAT-MI image of two 10% salinity square gel blocks embedded in a 0% salinity gel (b) Top view photo of the phantom

The second phantom imaged is of two 1 cm blocks of 10% salinity embedded in a 0% gel. The conductivity boundaries alone are reconstructed in the MAT-MI image. Thus, the boundaries between the two saline gels and the outer gel are seen in the reconstruction. Because the outer gel with 0% salinity and water have very close conductivities, this boundary is not present in the MAT-MI image.

3.6 Experiment Study with MR system

The MAT-MI method uses the combination of a static and a pulsed magnetic field to induce mechanical vibrations in the tissues due to the Lorentz force, which gives rise to measurable ultrasound signals for image reconstruction. However, the MAT-MI

imaging systems equipped with permanent magnets only acquired a small amplitude of ultrasound signals as real biological tissues are poor conductors of electricity, which limits the eddy current generation. Consequently, the imaging quality has been limited by the weak MAT-MI signals. In this section, we improved the measurement of MAT-MI tissue signals by using a high magnetic field from the magnetic resonance imaging (MRI) scanner for human study. Our testing results demonstrated this imaging system had the capability to reconstruct tissue structure reflecting electrical conductivity properties with improved imaging quality.

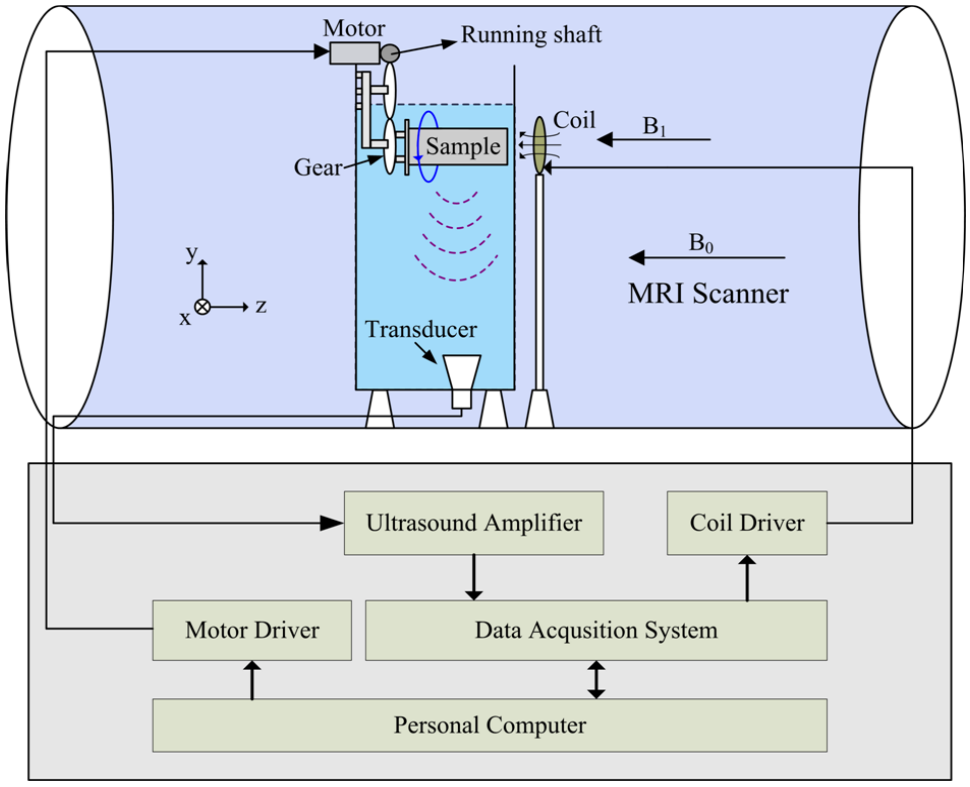

Fig.13, Hardware setup of MAT-MI imaging system under MRI scanner for biological tissue imaging.

Figure 13 shows the hardware setup for MAT-MI experiments in an MRI scanner. The MRI scanner (Magnet, Oxford, UK) had a maximum 9.4 T static magnetic field in horizontal Z direction and a 65 cm inner diameter bore for human imaging. Our sample and a 25 mm-diameter unfocused transducer (V301, Olympus, MA, USA) with nominal peak frequency of 0.5 MHz were immersed under distilled water in a plastic tank which was sitting vertically on a wooden bed placed in the MRI scanner bore. A customized non-magnetic linear motor (N-310K128, PhysikInstrumente, Germany) was mounted on the top of the tank. This motor had a 125 mm travel range, 7 m control cable and it could provide up to 10 N push or pull force. We designed a gear system to convert the motor's linear motion into rotary motion using three gears with a diameter of 32 mm cascaded to realize 360^{o} rotation of the sample for full-angle signal measurements. In experiments, the sample was fixed well to the bottom gear through a plastic sample holder. A customized magnetic stimulator was employed to deliver magnetic stimulation to the sample to induce eddy currents. The three-turn magnetic coil with an outer diameter of 70 mm was vertically placed very close to the tank wall to maximize the stimulation. The coil driver was equipped with an adjustable high-voltage source (0~24 kV), a capacitor and a solid state switch for handling large currents. The coil was embedded in a 2 mm thick plastic cylinder and placed as shown in the figure close to the imaging sample. We estimated the induced electrical field by using a sensing coil with a diameter of 30 mm. The sensing coil was placed on the surface of the plastic cylinder containing the magnetic coil. For charging voltage at 24 kV, the maximum induced voltage in the sensing coil was around 120 V. Consequently, the peak induced electrical field was estimated to be 1250

V/m. Piezoelectric signals collected by the transducer were amplified with low-noise ultrasound amplifiers (5660B, Olympus, MA,USA and VP2000, Reson, Denmark) before entering the data acquisition system which acquired 2048 data points for each channel with a 5 MHz sampling rate. To comply with MRI compatibility rules, all electrical devices were put outside of the shielded magnet room except for the transducer and the MRI-compatible linear motor. We used 7 m cables for electrical connections to the coil, the transducer and the motor as shown from the side view in figure 13.

We performed experiments on a well-controlled gel phantom to check the intensity of the induced MAT-MI ultrasound signal. In this experiment, two 50 mm-diameter, 25 mm-thickness single layer uniform phantoms built with a cooled gelatin solution were used. The phantoms had salinities of 0.7% and 1.0% for the comparison with the data obtained from the experiment using a permanent magnet. Five different charging voltages, i.e., 8, 12, 16, 20, 24 kV were chosen in the magnetic stimulator. The ultrasound signals were acquired with 20 times averaging to improve signal-to-noise ratio. The testing results are shown in figure 14. It can be seen that around 14 times improvement in induced MAT-MI ultrasound signals was observed, which mainly attributes to the use of a high 9.4 T static field in the MRI scanner. However, the energy losses in the long cable to the excitation coil and detection transducer significantly decrease the expected gain from high $\mathbf{B}_0$ field.

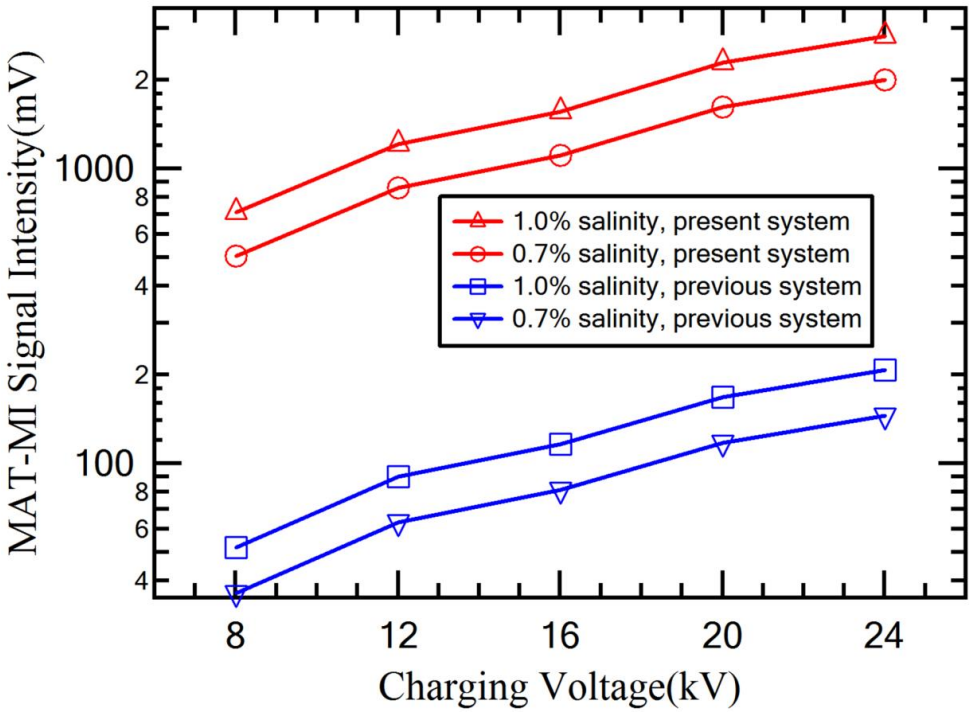

Fig. 14, Comparison of the induced MAT-MI ultrasound signal intensity produced by the previous experiment and present experiment in a 9.4 T MRI scanner. Single layer uniform phantoms with salinity of 0.7% and 1.0% were tested with different charging voltage setting.

Experiments were also performed on biological tissues. A piece of fresh pork tissue purchased from a local grocery store was cut into a size of 18mm × 15 mm × 15 mm for the experiment. This sample had a natural fat-muscle-fat structure implying detectable electrical conductivity contrasts for measurements. We put this tissue sample into a thin walled plastic container with a diameter of 50 mm. The container was then filled with a cooled gelatin solution with a salinity of 1.0% to finalize the sample as shown in the photograph in figure 15. The charging voltage was set at 16 kV and the ultrasound signal was acquired with 20 times data averaging. The collected single channel ultrasound data plotted in figure 15 clearly shows bipolar-structure signals,

which correspond well to the locations where electrical conductivity interfaces exist. The tissue signals appearing roughly at time points from 175.8 μs to 186.2 μs are in agreement with the approximate tissue thickness of 15 mm when considering an averaged acoustic speed of 1.5 mm/μs for soft tissues. The fat-muscle-fat tissue structure is also reflected in the recorded ultrasound data, demonstrating the capability of MAT-MI under an MRI scanner to resolve small conductivity contrasts in tissues even with single channel ultrasound measurement.

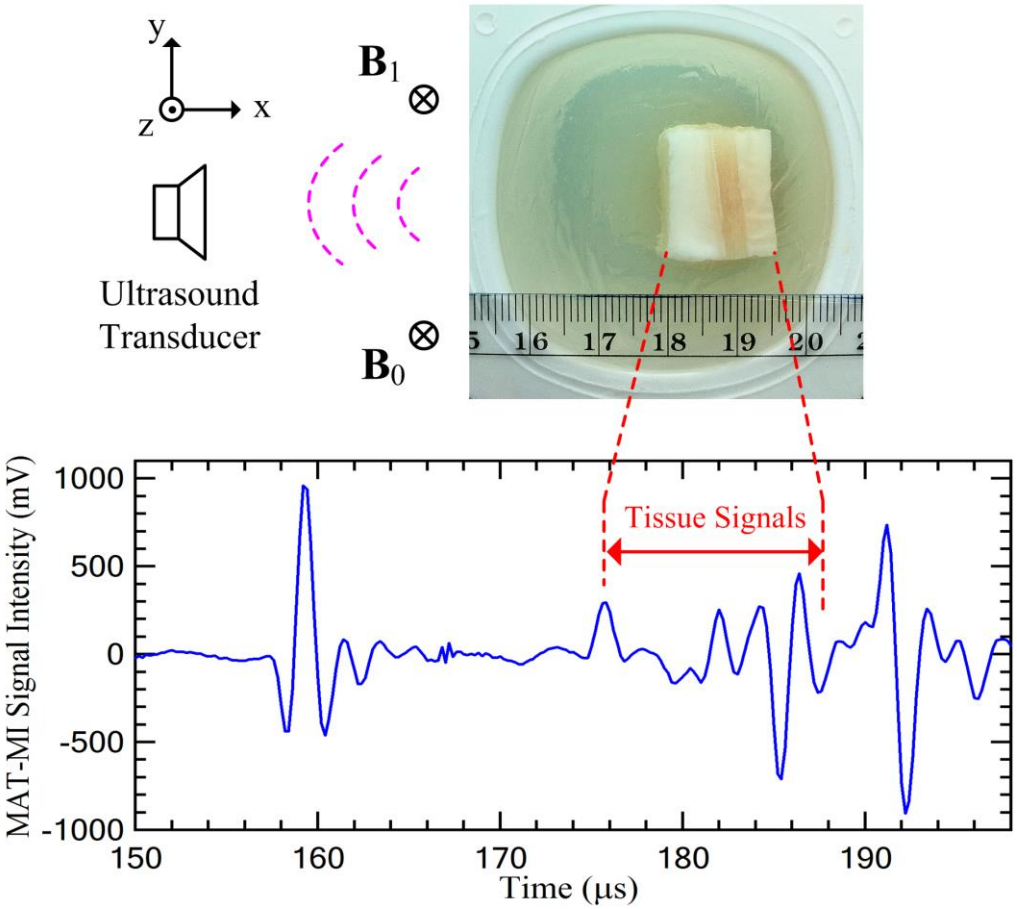

Fig. 15, A recorded temporal MAT-MI ultrasound wave shows the bipolar-structure signals reflecting the electrical conductivity contrast at muscle-fat interfaces in the pork tissue.

In addition, we performed imaging experiments on biological tissues. A piece of salted pork tissue (10 mm thickness in the Z direction) was adopted for a test. This sample had an irregular shape with a maximum length of 25 mm and a maximum width of 12 mm. The muscle portion had a 2 mm width between the two fat portions as shown in the top view photograph in figure 16(a). Scanning with an angular step of 3^{o} was done to collect 120-channel data with 40 times signal averaging for each channel. The reconstructed MAT-MI image is illustrated in figure 16(b), which shows the tissue structure in good agreement with the original photograph. However, due to a limited image spatial resolution tested in this study, the signals from the two internal tissue interfaces (fat-to-muscle and muscle-to-fat) with 2 mm spacing cannot be clearly distinguished. The second imaging experiment was conducted on a fresh pork phantom, which had low electrical conductivity value similar to real human tissue. This sample had a naturally formed fat-muscle structure as seen in figure 16(c) with a length of 22 mm and width of 12 mm. The thickness of the sample was around 12 mm. We acquired 120-channel MAT-MI signals with a 3^{o} angular step and 100 times data averaging for each channel. Figure 16(d) shows the reconstructed MAT-MI image with visible slanting fat-to-muscle interface, which matches well with the original photograph of the tissue structure in figure 16(c). To estimate the image quality, we used the contrast to noise ratio, defined as the ratio of the averaged signal intensity at the target interfaces to the standard deviation of the background noise in the reconstructed image. The contrast to

noise ratio for the fat-to-muscle interface in figure 16(d) is estimated to be ~6.8, which is higher than ~1.5 as measured from the previous imaging data (Hu *et al* 2011).

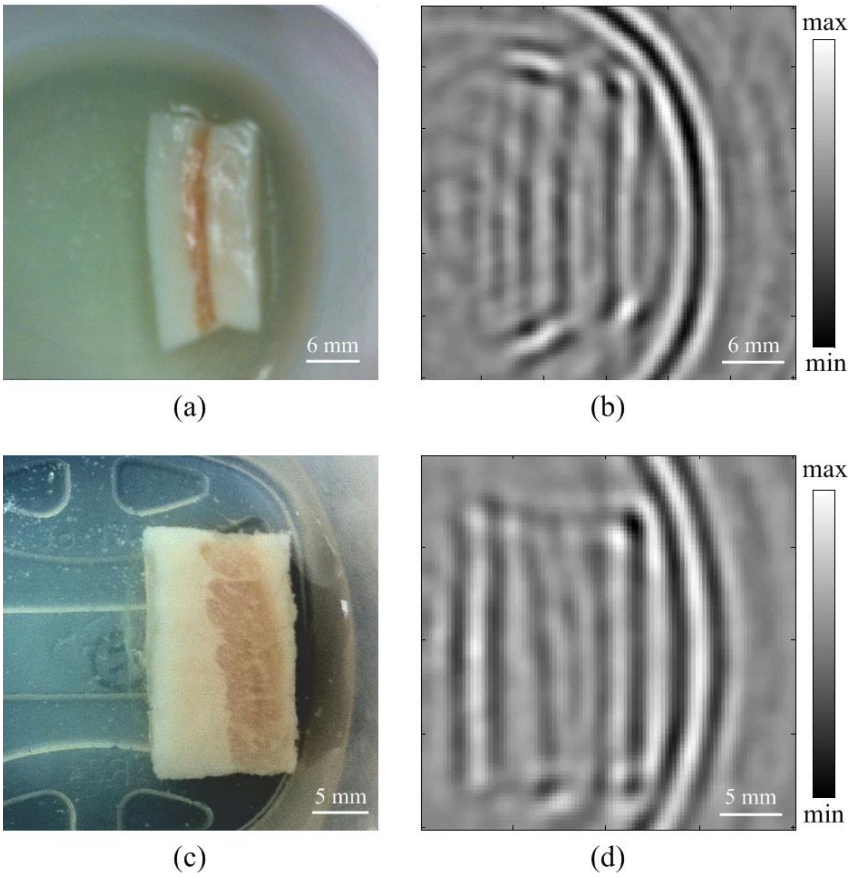

Fig.16, (a) Photograph of a salted pork tissue sample. The muscle portion has 2 mm width. (b) Reconstructed MAT-MI image of the tissue sample shown in (a). (c) Photograph of a fresh pork phantom with a slanting fat-to-muscle interface.(d) Reconstructed MAT-MI image of the tissue sample shown in (c).

3.7 In-vivo small animal tumor imaging

In this work, we have performed experiments to evaluate the performance of MAT-MI imaging in detecting in-vivo tumors in a mouse model. Previous studies have shown that MAT-MI imaging is capable of differentiating conductivity contrast seen between ex-vivo human liver tissue and tumors (Hu *et al* 2011). As the conductivity is dependent on several factors such as temperature, cell structure, tissue fluid content, etc, which vary between in-vivo and ex-vivo conditions, a mouse tumor model allows validating the MAT-MI method in distinguishing and imaging tumors in living systems.

For these experiments, a human prostate tumor in a mouse model has been used. Prostate tumors are the most widely diagnosed malignancy in males and the second most reason for cancer deaths (Cancer Facts and Figures, 2005). The 5 year survival rate is close to 100% when the cancer is detected early and while still confined to the prostate (Cancer Facts and Figures, 2005). The commonly used methods for prostate cancer detection, namely prostate specific antigen detection (PSA) and digital rectal exams, although capable of detecting a high percentage of tumors, still have limitations (Carter 2004). Studies of electrical impedance measurements on prostate tissue have shown that prostate cancer has a significantly different electrical conductivity in comparison to surrounding normal tissue (Lee *et al* 1999, Halter *et al* 2007, Mishra *et al* 2012). This has led to active research in the diagnosis of prostate cancers based on bioimpedance measurements. The mouse experiments performed here have been approved by the Institutional Animal Care and Use Committee (IACUC) for animal research at the University of Minnesota.

3.7.1 Experiment Setup and Result

Tumors were induced by injecting LNCaP cells into the hind limbs of 7 week old nude mice. The LNCaP cell line was derived from human prostate adenocarcinoma and has commonly been used in cancer research (Horoszewicz *et al* 1983). Specifically, 1e6 cells suspended in 0.1 mL Matrigel matrix (50% Matrigel and 50% LNCaP growth medium) were subcutaneously injected into the hind limb of each 24-g nude mouse. Tumors grown for 4 to 6 weeks with a diameter of 5 to 10 mm were used for the imaging experiments. The imaging experiment setup is seen in figure 17(a) and gross histology of the tumor

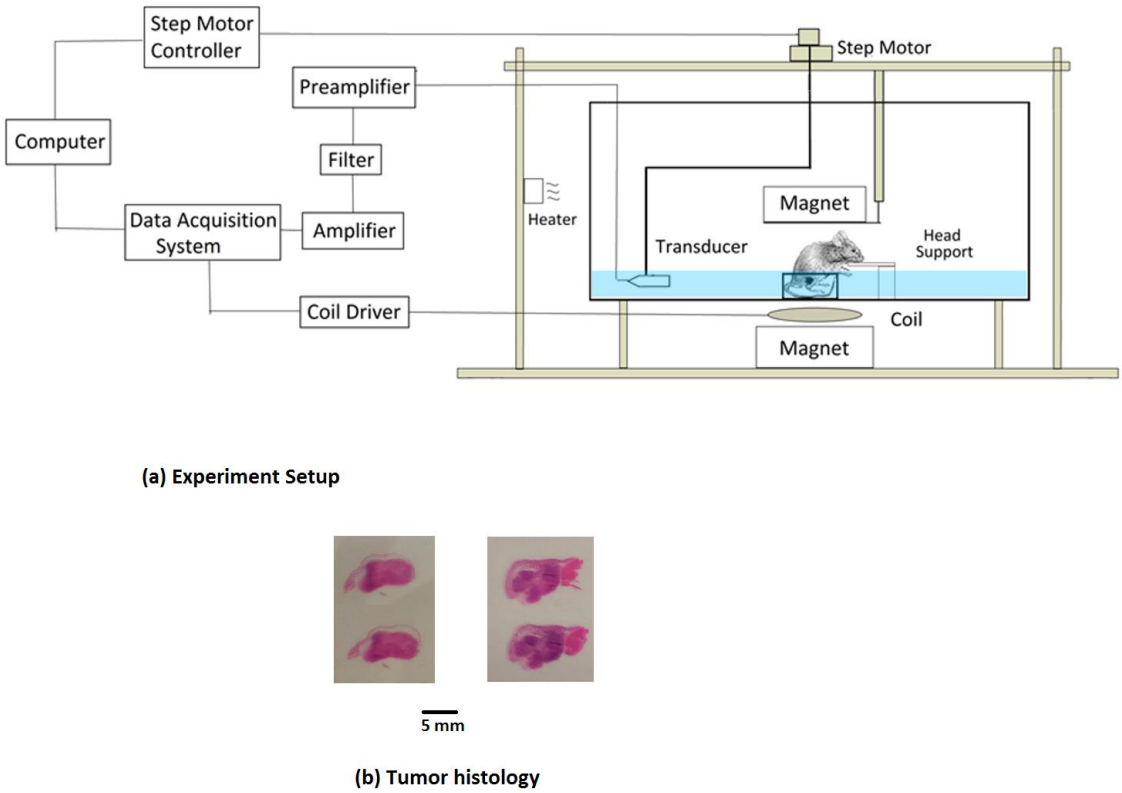

Fig.17, (a) Schematic diagram of experiment setup. (b) Gross histology of tumor cross-section parallel to the imaging plane

reflecting the imaging crossection is shown in figure 17(b). As seen in figure 17(a), the anesthetized mouse with the tumor is placed, in a sitting position, inside a cup and fixed in this position with a cooled agar gel. The cup region with the tumor is immersed under warm water for coupling of the acoustic signal with the ultrasound transducer, while the head of the mouse is held outside the water to allow for normal breathing. For the MAT-MI experiment, scanning is done over a 180 degree view angle in a circular scan setup. The system operates with a 500 kHz center frequency. After the MAT-MI experiment, the mouse phantom was scanned using a 5 MHz ultrasound scanner to obtain high resolution sonogram images for comparison with the MAT-MI image reconstruction. After the imaging, the mouse is sacrificed and histology is performed on the tumors as seen in figure 17(b).

Figure 18 shows the image reconstruction of the mouse with hind limb tumors. The top view photo of the mouse placed in the cup is shown in figure 18(a), and the sonogram of the mouse showing the cross-section along the imaging plane is shown in figure 18(b). The regions containing the tumors on the surface of the hind limb can be seen in the sonogram. The MAT-MI image of the mouse is seen in figure 18(c). From the figure, it can be seen that the structure of the tumor can be imaged, and the internal tumor-muscle interface shows in the reconstruction which allows for the identifying of the tumor from normal tissue under in-vivo conditions.

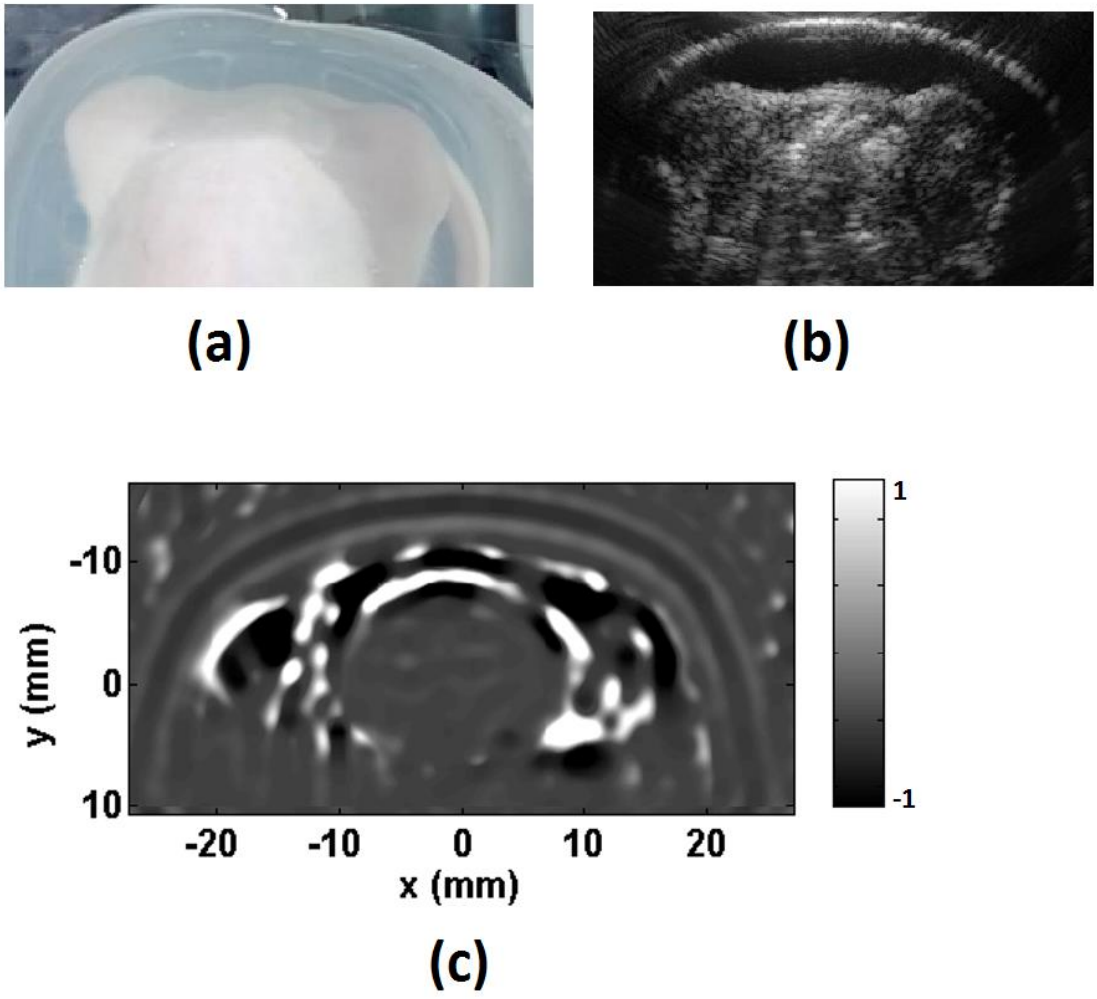

Fig 18 (a) Photo of the mouse (b) Sonogram along the MAT-MI imaging plane (c) MAT-MI conductivity contrast imaging, the boundaries of the hind limb tumors are seen

3.8 Discussion

We have applied to MAT-MI a point receiver based scanning method and the commonly used ultrasound reconstruction method, i.e. B-scan imaging. This allows for the use of mature scanning techniques in ultrasonography to reconstruct the MAT-MI acoustic sources. The reconstructed images in computer simulation and experiments show a good agreement with the corresponding target source profiles.

We have assumed uniform magnetic fields in the current simulations which can be achieved when the coils used for generating the magnetic fields are sufficiently larger than the object dimensions. In addition, since the current study is focused on imaging the acoustic source distribution, a uniform magnetic field assumption works well for both our computer simulation and experiments. On the other hand, the variations in the uniformity of the fields as seen in our experiment system can be accounted for in estimating conductivity distribution from the reconstructed acoustic source images as demonstrated (Li and He 2010) where exact magnetic coil configurations have been used.

The B-scan technique uses the focus region of a transducer's gain map for imaging, and this for a given transducer allows imaging of an object from a much closer distance and promises an improved sensitivity. The point receiver based method, however, requires the transducer to be placed at a relatively far distance away from the source giving it lower sensitivity. The B-scan technique thus optimizes the ultrasound receiver for the MAT-MI system. The experimental implementation of the method requires the transducer to be placed at a closer distance to the object. This also leads to a higher electromagnetic interference (EMI) from the magnetic stimulator which requires a

careful design of the stimulator to have very low ringing on turn off for the EMI to subside at the time the ultrasound signal arrives at the transducer. The stimulator design implemented in the current system has very low oscillations on turn off, but it is weaker in strength than the ones used in previous MAT-MI experiments giving an overall lower system SNR. Therefore, to fully realize the potential of B-scan imaging for MAT-MI a stronger stimulator with very low oscillations on turn off is required.

In the present system, the sector scan is achieved by mechanically rotating a focus transducer. In a practical setting, this could also be done by beam forming and beam steering using a transducer array with better efficiency and accuracy. In addition, the discrete number of scanning locations needed by the compound scan scheme for reconstruction allows using MAT-MI when a limited number of acoustic windows are available. Thus, a method like this promises to broaden the applicability of MAT-MI for human imaging.

In all the algorithm derivations, we assumed that the medium is acoustically homogenous, and the effect of acoustic heterogeneity in soft tissues is negligible. The acoustic heterogeneity of soft tissue is less than 10% (Duck 1990), and the acoustic pathway in MAT-MI is about half the length of conventional diagnostic ultrasound. Furthermore, the effect of acoustic heterogeneity in MAT-MI is quite similar as that in photoacoustic tomography (PAT), which has been demonstrated negligible both theoretically (Xu and Wang 2003) and experimentally (Wang *et al* 2003). Normally, the acoustic heterogeneity could be considered as a secondary scattering acoustic source. If the amplitude of these secondary acoustic signals is small, acoustic signals generated by

them can be taken as background noise. A corresponding random noise model may be used to investigate how acoustic heterogeneity influences the proposed reconstruction algorithm. More theoretical discussion about the effect of acoustic heterogeneity on thermoacoustic tomography (TAT) can be found in the references (Anastasio *et al* 2005).

In the study with a high power magnetic pulser and the MRI system, we observed that technical challenges degrade the final image contrast-to-noise ratio. The long coil cable (7 meter) leads to energy loss in addition to introducing redundant capacitance and inductance causing significant ringing and noise in the system due to the strong differential effects produced by $d\mathbf{B}_1/dt$ while inducing tissue eddy currents. In addition, the long cable for ultrasound detection picks up more environmental noise, which pollutes the measured MAT-MI signals.

In the circular scanning system used with the high power pulser, a large scanning radius of ~ 30 cm is used to reduce the effect of high EMI in this system. However, this limits the possible Z resolution with a 500 kHz scanning setup to ~ cms and leads to the averaging of the Z profile of the object in the reconstruction. In phantoms with complex structures, this leads to further degradation of imaging quality. A higher frequency system with lower EMI would allow good resolution crossection imaging with available practical ultrasound setup.

In the current simulation study we have used Field II software to simulate ultrasound transducers used with MAT-MI. Compared to the previous MAT-MI simulations (Li *et al* 2007, Li *et al* 2009, Xia *et al* 2009) where an ideal ultrasound receiver is assumed, the current simulation takes into account the finite bandwidth and

shape of the transducer used for imaging. These simulations, taking the transducer parameters into account, validate our experimental observations with MAT-MI where the acoustic sources at the boundaries of conductivity change alone get reconstructed.

Chapter 4

Conductivity Imaging through Vector Source Reconstruction

4.1 Introduction

In the present study, we propose a conductivity reconstruction method based on vector acoustic source imaging as the intermediate step. The vector source field, which is a component of the induced eddy current, unlike the boundary signal dominant scalar acoustic field, is uniformly present throughout the conductive object, and such a field requires lesser frequency bandwidth to be reliably estimated. Further, using a relationship between the conductivity distribution of the object and the MAT-MI source component of the induced current, using Helmholtz decomposition for a piece-wise homogeneous object, we reconstruct the complete object's conductivity. The developed reconstruction algorithm is applied to MAT-MI simulation, gel phantom, biological tissue and ex-vivo tissue experiments with limited bandwidth acoustic measurement setup to test its performance. Further, using numerical simulations, we can estimate the imaging point spread function (PSF), which gives the resolution of the reconstruction. It is shown in these experiments that reliable conductivity estimation is possible with the proposed reconstruction method under limited bandwidth ultrasound measurement and using a single magnetic excitation. This allows for practical implementation of the MAT-MI approach for human imaging applications for differentiation of tissue types based on conductivity distribution, which has potential application for cancer imaging. Most

materials in this chapter have been previously published (Mariappan and He 2013, Mariappan *et al* 2014).

4.2 Imaging Problem Description

4.2.1 Forward Problem

The forward problem here describes the process of generation of the pressure waves from the Lorentz force in the medium and relates the velocity, at a point of the wave, to the Lorentz force. In an object with an induced current $\boldsymbol{J}(\boldsymbol{r},t)$ placed in a static magnetic field $\boldsymbol{B_0}(\boldsymbol{r})$, it leads to the Lorentz force acting on the object given by $\boldsymbol{F}(\boldsymbol{r},\boldsymbol{t}) = \boldsymbol{J}(\boldsymbol{r},t) \times \boldsymbol{B_0}(\boldsymbol{r})$. This time varying Lorentz force gives rise to acoustic waves in the medium. For an in-viscid fluid medium, the linearized Navier-stoke's equation describing the pressure wave is as follows (Xu and He 2005 , Roth and Wikswo 1998,Cobbold 2007):

$$\rho \frac{\partial \boldsymbol{v_1}}{\partial t} = -\nabla p_1 + \boldsymbol{F} \tag{4.1}$$

where ρ is the density, $\boldsymbol{v_1}(\boldsymbol{r},t)$ is velocity and $p_1(r,t)$ is the pressure at point in the medium at time t. The acoustic wave leads to small changes in the object density, pressure and velocity which can be described as a combination of steady state value $(\rho_0, p_0, \boldsymbol{v_0} = \boldsymbol{0})$ and a small change $(\rho, p, \boldsymbol{v})$ due to the acoustic wave. The continuity equation in the medium for such an acoustic wave can be described as:

$$\frac{\partial p}{\partial t} + \rho_0 \nabla \cdot \boldsymbol{v} \approx 0 \tag{4.2}$$

Further, under isentropic conditions, the small changes in pressure and density can be described as follows:

$$\beta_s p = \frac{\rho}{\rho_0} \tag{4.3}$$

where β_s is the adiabatic compressibility of the medium. The continuity equation can then be written as follows:

$$\beta_s \frac{\partial p}{\partial t} + \nabla \cdot \boldsymbol{v} \approx 0 \tag{4.4}$$

The Navier-stoke's equation combined with the continuity equation describes the acoustic wave in the medium due the force $\boldsymbol{F}$. The acoustic wave equation in terms of pressure can be obtained by taking the divergence of (4.1):

$$\nabla^2 p - \frac{1}{c_s^2}\frac{\partial^2 p}{\partial t^2} = \nabla \cdot \boldsymbol{F} \tag{4.5}$$

where $c_s = \frac{1}{\sqrt{\rho_0 \beta_s}}$. Using the Helmholtz representation, the vectors $\boldsymbol{F}$ and v can be described as the sum of a rotational component ($\boldsymbol{F_c}$ and $\boldsymbol{v_c}$) whose divergence is zero and irrotational component ($\boldsymbol{F_d}$ and $\boldsymbol{v_d}$) whose curl is zero. So the source of MAT-MI acoustic pressure can be written as $\nabla \cdot \boldsymbol{F} = \nabla \cdot \boldsymbol{F_d}$.

The temporal derivative of 4.1 gives the wave equation in terms of the irrotational velocity component as follows:

$$\nabla^2 \boldsymbol{v_d} - \frac{1}{c_s^2}\frac{\partial^2 \boldsymbol{v_d}}{\partial t^2} = -\beta_s \frac{\partial \boldsymbol{F_d}}{\partial t} \tag{4.6}$$

where $\nabla(\nabla \cdot \boldsymbol{v_d}) = \nabla^2 \boldsymbol{v_d}$. The equation with the rotational component of the velocity corresponds to the propagation of shear waves in the medium with no pressure or density changes. In biological tissues these shear waves are strongly attenuated and are not available for measurements outside the object. For a MAT-MI current source

$\boldsymbol{J}(\boldsymbol{r},t) = \boldsymbol{J}(\boldsymbol{r})\delta(t)$ integrating both left and right hand sides of equation 4.5 from $t = (\infty, 0^+)$ where 0^+ is an infinitely small positive real value, we have (Xu and He 2005):

$$\rho_0 \boldsymbol{v}(\boldsymbol{r}, 0^+) = \boldsymbol{F_d}$$

The pressure in the medium is given by the greens function solution to equation 4.5:

$$p(\boldsymbol{r},t) = -\frac{1}{4\pi}\iiint d^3r' \nabla_{\mathrm{r}'} \cdot \boldsymbol{F}(\boldsymbol{r}',t)\, G(\boldsymbol{r},\boldsymbol{r}',t) \tag{4.7}$$

where $\boldsymbol{r}'$ is the location of the acoustic source, $\boldsymbol{r}$ is the location detector, $\nabla_{r'}$ implies derivative with respect to source space $\boldsymbol{r}'$, the Green's function for this solution $G(\boldsymbol{r},\boldsymbol{r}',t) = \frac{\delta\left(t-\frac{R}{c_S}\right)}{R}$ where $R = |\boldsymbol{r} - \boldsymbol{r}'|$. The volume integration is carried out over the acoustic source distribution in the object space Ω. This equation gives the observed pressure for an impulse source i.e. a source with its time function as $\delta(t)$. An induced acoustic source field with time dependence $h(t)$ gives an observed pressure $p(\boldsymbol{r},t) \otimes h(t)$, where $\otimes$ is the convolution operator. The Green's function for this time dependence can be written as: $G(\boldsymbol{r},\boldsymbol{r}',t) = \frac{h\left(t-\frac{R}{c_S}\right)}{R}$ (Mariappan *et al* 2011).

The ultrasound transducers that are commonly used in medical systems measure the pressure of the acoustic wave. In regions outside the object where the source is zero or for an impulse source ($\boldsymbol{J}(\boldsymbol{r},t) = \boldsymbol{J}(\boldsymbol{r})\delta(t)$) at time $t > 0^+$ the velocity can be related to pressure from equation 4.1 as follows:

$$\nabla p = -\rho_0 \frac{\partial \boldsymbol{v_d}}{\partial t}$$

4.2.2 Inverse Problem

In the inverse problem, first we describe a method based on ultrasound beamformation to estimate the vector source distribution from the measured pressure signal along the scanning aperture. Then, from the relationship of the conductivity distribution to this vector source and the applied magnetic fields we reconstruct the conductivity image of the object.

As the static magnetic field $\boldsymbol{B_0}$ in MAT-MI is generated from external sources outside the conductive object, so its spatial distribution can be determined by the setup generating the magnetic field. The field from the permanent magnets used in the current study can be approximated to $\boldsymbol{B_o} = \mathrm{B}\,\hat{k}$, where B is a constant and $\hat{k}$ is the unit vector in the Z direction. This leads to $\nabla \times \boldsymbol{B_0}$ being negligible inside the object space and the acoustic source can be further simplified as $\nabla \times (\boldsymbol{J}) \cdot \boldsymbol{B_0}$. Now, the induced eddy current $\boldsymbol{J}$ is a smooth function that vanishes outside the object space with its first derivative, so it can be decomposed into a rotational part $\boldsymbol{J_c}$ and an irrotational part $\nabla\theta$ (Joseph 2006). The current $\boldsymbol{J}$ can be written as:

$$\boldsymbol{J} = \boldsymbol{J_c} + \nabla\theta \tag{4.8}$$

Of these two components, the term $\boldsymbol{J_c}$ acts as the source for the acoustic wave, as $\nabla \times \boldsymbol{J} = \nabla \times \boldsymbol{J_c}$ and the MAT-MI acoustic source can then be written as $\nabla \cdot \boldsymbol{F_d} = \nabla \cdot (\boldsymbol{J_c} \times \boldsymbol{B_0})$.

4.2.3 Beamformation: Vector Source Imaging

In the present section, the rotational component of the induced current density is reconstructed through the design of vector point spread functions for the ultrasound

measurement system. For an unfocussed small aperture detector acting as a point receiver, the pressure signal at the receiver can be described by equation (4.7):

$$p(\boldsymbol{r},t) = -\frac{1}{4\pi}\iiint d^3r'\nabla_{r'}\cdot\left(\boldsymbol{J_c}(\boldsymbol{r'})\times\boldsymbol{B_0}(\boldsymbol{r'})\right)G(\boldsymbol{r},\boldsymbol{r'},t)$$

The current source is zero outside the conductive object region, so this equation can be rewritten as follows:

$$p(\boldsymbol{r},t) = \frac{1}{4\pi}\iiint d^3r'\left(\boldsymbol{J_c}(\boldsymbol{r'})\times\boldsymbol{B_0}(\boldsymbol{r'})\right)\cdot\nabla_{r'}G(\boldsymbol{r},\boldsymbol{r'},t) \qquad (4.8)$$

As the ultrasound measurement aperture used for MAT-MI imaging comprises of a finite number of receivers, the formulization of the image reconstruction can readily be discretized. By applying a beamformer algorithm (Ranganathan and Walker 2003) with the signal received at the sensor locations, we can design the imaging PSF to extract the orthogonal components of the vector source. The beamformer algorithm comprises of summing up the magnitude weighted and time delayed signal at all the receiver locations. This can be described by the following equations

$$V(\boldsymbol{r_s}) = \sum_n W_a p(\boldsymbol{r}, t - t_a) \qquad (4.9)$$

Where W_a is the weight applied to the ultrasound signal, t_a is the time delay applied to the signal, n is the number of ultrasound receiver signals used in the beamformation process and V is the resultant signal obtained at source location $\boldsymbol{r_s}$ from the beamformation process. Now substituting for the pressure $p(\boldsymbol{r},t)$ using equation (4.8) in (4.9) we get

$$V(\boldsymbol{r_s}) = \sum_n W_a\left(\frac{1}{4\pi}\right)\iiint d^3\boldsymbol{r'}(\boldsymbol{J_c}(\boldsymbol{r'})\times\boldsymbol{B_0}(\boldsymbol{r'}))\cdot\nabla_{r'}G(\boldsymbol{r},\boldsymbol{r'},t-t_a) \qquad (4.10)$$

Interchanging the integration over the source space and the summation over the sensor space, (4.10) can be written as

$$V(\boldsymbol{r_s}) = \iiint d^3\boldsymbol{r'}(\boldsymbol{J_c}(\boldsymbol{r'}) \times \boldsymbol{B_0}(\boldsymbol{r'})) \cdot (\frac{1}{4\pi}) \sum_n W_a \nabla_{r'} G(\boldsymbol{r}, \boldsymbol{r'}, t - t_a)$$

$$= \iiint d^3\boldsymbol{r'}\boldsymbol{J_c}(\boldsymbol{r'}) \cdot (\boldsymbol{B_0}(\boldsymbol{r'}) \times (-\tfrac{1}{4\pi}) \textstyle\sum_n W_a \nabla_{r'} G(\boldsymbol{r}, \boldsymbol{r'}, t - t_a)) \qquad (4.11)$$

The vector term $\boldsymbol{S}(\boldsymbol{r'}) = (\frac{-1}{4\pi}) \sum_n W_a \nabla_{r'} \mathrm{G}(\boldsymbol{r}, \boldsymbol{r'}, \mathrm{t} - \mathrm{t_a}))$ is the point spread function (PSF) of the ultrasound imaging system. The beamforming algorithm is designed such that the vector $\boldsymbol{S}(\boldsymbol{r'})$ is a spatial impulse pointing in one of the orthogonal spatial directions, for example $\boldsymbol{S}(\boldsymbol{r'}) \approx \delta(\boldsymbol{r'})\hat{\imath} + 0\,\hat{\jmath}$, where $\hat{\imath}, \hat{\jmath}$ are the orthonormal vectors describing X and Y directions. Another design with beamformer algorithm is implemented using a new set of weights and time delay to obtain a vector PSF pointing in the other orthogonal direction i.e. $\boldsymbol{S}(\boldsymbol{r'}) \approx 0\,\hat{\imath} + \delta(\boldsymbol{r'})\hat{\jmath}$. Such PSF vectors combined with the knowledge of $\boldsymbol{B_0}(\boldsymbol{r'})$ can be used to extract the individual components of the current density $\boldsymbol{J_c}$ which induces the MAT-MI acoustic waves.

4.2.4 Beamformation Design

This term $S(\boldsymbol{r'})$ is the point spread function (PSF) of the ultrasound imaging system reconstructing the orthogonal components of the vector source. The weights and time delay to generate such a vector point spread function can be computed by forming a set of linear equations with the known Green's function distribution as follows:

$$Ux = b \qquad (4.12)$$

where, $U = \frac{-1}{4\pi}\begin{pmatrix}\nabla_{y'}G(\boldsymbol{r},\boldsymbol{r}',t-t_a)\\ \nabla_{x'}G(\boldsymbol{r},\boldsymbol{r}',t-t_a)\end{pmatrix}$

when, $x = W_a$ and $b = \begin{pmatrix}\delta(\boldsymbol{r}')\\ 0\end{pmatrix} or \begin{pmatrix}0\\ \delta(\boldsymbol{r}')\end{pmatrix}$ corresponding to the two desired point spread functions reconstructing the x and the y component of the current source respectively and $t = \frac{|r-r_s|}{c_s}$ to obtain the source at location $\boldsymbol{r_s}$.

4.2.5 Impedance Estimation

In MAT-MI a conductive object with an isotropic conductivity of $\sigma(\boldsymbol{r})$ is placed in the presence of a static magnetic field with flux density $\boldsymbol{B_0}(\boldsymbol{r})$, and a time varying magnetic pulse $\boldsymbol{B_1}(\boldsymbol{r},t)$ is applied to the object. This magnetic field induces an electric field $\boldsymbol{E}(\boldsymbol{r},t)$ in the object which for a conductive sample gives rise to eddy currents $\boldsymbol{J}(\boldsymbol{r},t) = \sigma(\boldsymbol{r})\boldsymbol{E}(\boldsymbol{r},t)$ in the object.

The magnetic pulse used in MAT-MI is generated using approximately microsecond long currents through coils which lead to magnetic fields with slow time variation such that the propagation time of the field through the object is negligible. This allows the magnetic induction problem in MAT-MI to be considered as quasi-static. The skin depth of the corresponding MHz field in general biological tissue is at the level of meters, which is much larger than the characteristic dimension of the object, so the magnetic diffusion can be ignored (Wang and Eisenberg 1994). This allows the applied magnetic field to be uniquely determined by the coil setup and the separation of the spatial and temporal functions in the electromagnetic field analysis of MAT-MI as in $\boldsymbol{B_1}(\boldsymbol{r},t) = \boldsymbol{B_1}(\boldsymbol{r})f(t)$, $\boldsymbol{E}(\boldsymbol{r},t) = \boldsymbol{E}(\boldsymbol{r})f'(t)$ where the prime indicates first

derivative. In addition to this, the microsecond long magnetic stimulation also leads to the displacement current being much weaker than the ohmic current due to the fact that $\sigma >> \omega\epsilon$ in biological tissue in the 1 MHz range (Xu and He 2005), where ω is the angular frequency of the stimulating field and ϵ is the permittivity of the object. After applying the above approximations, the induced current in MAT-MI can be described by the following equations:

$$\begin{cases} \nabla \cdot \left(-\sigma \frac{\partial \boldsymbol{A}}{\partial t} - \sigma \nabla \phi\right) = 0 \; in \Omega \\ \boldsymbol{J} \cdot \mathbf{n} = 0 \text{ on } \partial\Omega \end{cases} \tag{4.13}$$

where Ω denotes the domain in which the object is present, $\boldsymbol{A}$ is the magnetic vector potential corresponding to magnetic stimulation $\boldsymbol{B_1} = \nabla \times \boldsymbol{A}, \nabla \cdot \boldsymbol{A} = 0$ and ϕ is the electrical scalar potential; n is the unit vector normal to the boundary surface $\partial\Omega$. The quasi-static condition in MAT-MI allows estimating the magnetic vector potential $\boldsymbol{A}$ directly from the configuration of the coils and the currents applied to them. For a known conductivity distribution σ and vector potential $\boldsymbol{A}$, the above magnetic induction problem can be solved in the domain Ω for the electric potential ϕ using the finite element method (FEM) simulations. The electric field can then be obtained as

$$\boldsymbol{E} = -\frac{\partial \boldsymbol{A}}{\partial t} - \nabla \phi \tag{4.14}$$

In the presence of a static magnetic field $\boldsymbol{B_0}$ the induced eddy current is subject to Lorentz force $\boldsymbol{J} \times \boldsymbol{B_0}$, and the time-varying Lorentz force gives rise to a traveling acoustic wave. In MAT-MI the divergence of the Lorenz force $\nabla \cdot (\boldsymbol{J} \times \boldsymbol{B_0})$ acts as the source of the acoustic wave

Now the reconstructed vector source is uniformly present in the object and can be used to directly estimate the conductivity in an object with piece wise homogeneous conductivity distribution. The induced current density J is given by:

$$\boldsymbol{J} = -\sigma \boldsymbol{E} = -\sigma \frac{\partial \boldsymbol{A}}{\partial t} - \sigma \nabla \phi \tag{4.15}$$

This can be rewritten as follows:

$$\boldsymbol{J} = -\sigma \frac{\partial \boldsymbol{A}}{\partial t} + \phi \nabla \sigma - \nabla(\sigma \phi) \tag{4.16}$$

For an object with piece-wise homogeneous conductivity distribution, $\nabla\sigma \approx 0$ at points other than at the conductivity boundaries. So in regions away from the boundary, the induced current can be approximated as follows:

$$\boldsymbol{J} \approx -\sigma \frac{\partial \boldsymbol{A}}{\partial t} - \nabla(\sigma \phi) \tag{4.17}$$

In this region, the term $-\sigma \frac{\partial \boldsymbol{A}}{\partial t}$ is a purely rotational vector due to the design of themagnetic vector potential $\boldsymbol{A}$ and is the only contributor to the MAT-MI acoustic pressure source in the homogeneous region given by $-\sigma \nabla \times \frac{\partial \boldsymbol{A}}{\partial \boldsymbol{t}}$. So the vector source $\boldsymbol{J_c}$, which is the rotational part of the induced current, under a piece-wise homogeneous conductivity distribution at points away from the boundary, can be represented as follows:

$$\boldsymbol{J_c} \approx -\sigma \frac{\partial \boldsymbol{A}}{\partial t} \tag{4.18}$$

Under limited bandwidth reconstruction which is encountered in ultrasound imaging systems (Li and He 2010, Mariappan and He 2013), the point spread function acts as a band pass filter removing the dc to low frequency components of the generated

signal. The resultant point spread function of the imaging system is a non-ideal pulse, and to get a more complete reconstruction of the current source, the estimated point spread function of the imaging system can be used to filter the reconstructed image. Further, in the presence of noise there is a tradeoff between the completeness of the inverse filtering process and noise amplification. When a uniform pulsed field $\boldsymbol{B_1} = \boldsymbol{\nabla} \times \boldsymbol{A}$ is applied over the object space, the induced MAT-MI current source which is proportional to the vector potential increases with the radius inside the homogeneous conductive region (Xia *et al* 2009), and the curl of the current source is approximately constant away from the conductivity boundaries (Li *et al* 2007).

Under the noise conditions leading to inaccuracies in the estimated acoustic source reconstruction, the conductivity can then be better estimated from a modification to the above vector equation as follows:

$$\sigma \approx S_1 \backslash S_2 \tag{4. 19}$$

where

$$S_1 = (\boldsymbol{J_c}(y'_{1n}, y'_{2n}..y'_{nn}) \cdot \hat{\imath} - \boldsymbol{J_c}(y'_{1m}, y'_{2m}..y'_{mm}) \cdot \hat{\imath}) + (\boldsymbol{J_c}(x'_{1n}, x'_{2n}..x'_{nn}) \cdot \hat{\jmath} - \boldsymbol{J_c}(x'_{1m}, x'_{2m}..x'_{mm}) \cdot \hat{\jmath})$$

$$S_2 = (\boldsymbol{A'}(y'_{1n}, y'_{2n}..y'_{nn}) \cdot \hat{\imath} - \boldsymbol{A'}(y'_{1m}, y'_{2m}..y'_{mm}) \cdot \hat{\imath}) + (\boldsymbol{A'}(x'_{1n}, x'_{2n}..x'_{nn}) \cdot \hat{\jmath} - \boldsymbol{A'}(x'_{1m}, x'_{2m}..x'_{mm}) \cdot \hat{\jmath})$$

where, $A' = \frac{\partial A}{\partial t}$, \ operator is the least square fit ,$\boldsymbol{x'}, \boldsymbol{y'}$, are points which vary along the x, y coordinates within a region of uniform conductivity in the object, S_1, S_2 are similar to the curl of the current source and the vector potential, respectively, in a homogeneous conductivity region. The boundaries of such a region can be determined

from the MAT-MI acoustic source distribution, which is the strongest at the location of conductivity change in the object (Li *et al* 2007, Li *et al* 2011, Mariappan *et al* 2012). The conductivity estimation around the boundaries of a homogeneous region, where the error is maximum over one imaging resolution, is determined by interpolating the values around the region.

4.3 Computer Simulation

4.3.1 Beamformation Based Imaging

The proposed image reconstruction technique has been verified with computer simulations. In these studies, the conductive samples and the magnetic fields were assumed to be homogeneous in the z direction. With these approximations and an appropriate setup for acoustic measurements, we can simplify the corresponding MAT-MI imaging problems to 2-D problem.

Figure 19(a) shows the diagram of the MAT-MI imaging setup, and figure 19(b) shows the design of the point spread function for the scalar and vector source reconstruction. In the computer simulation setup as seen in figure 19(a), the static magnetic field $\boldsymbol{B_0}$ points in the Z direction with a uniform strength of 1 Tesla, and the pulsed magnetic field is applied with a coil arrangement as seen in the figure. For the simulation, a coil pair of 16 cm diameter separated by 3 cm is used to build a uniform magnetic field over the object space, which has a dimension of 10 by 10 by 2 cm and it is placed symmetric to the center of the coils. A current pulse applied to the coil generates the magnetic field, and the maximum rate of change of the current is fixed at 10^7A/s. The

electric potential ϕ induced in the object space is computed using FEM simulations with COMSOL of the partial differential equation as described in equation (4.13). The induced electric field is determined according to equation (4.14) using the computed electric potential ϕ from which the induced current density is determined as $\boldsymbol{J} = \sigma \boldsymbol{E}$. This current density $\boldsymbol{J}$ is then interpolated to a square mesh of size 10×10 cm with a grid size of 0.15 mm from which the induced MAT-MI acoustic source distribution is then computed according to $As = \nabla \cdot \boldsymbol{F} = (\nabla \times \boldsymbol{J}) \cdot \boldsymbol{B_0}$.

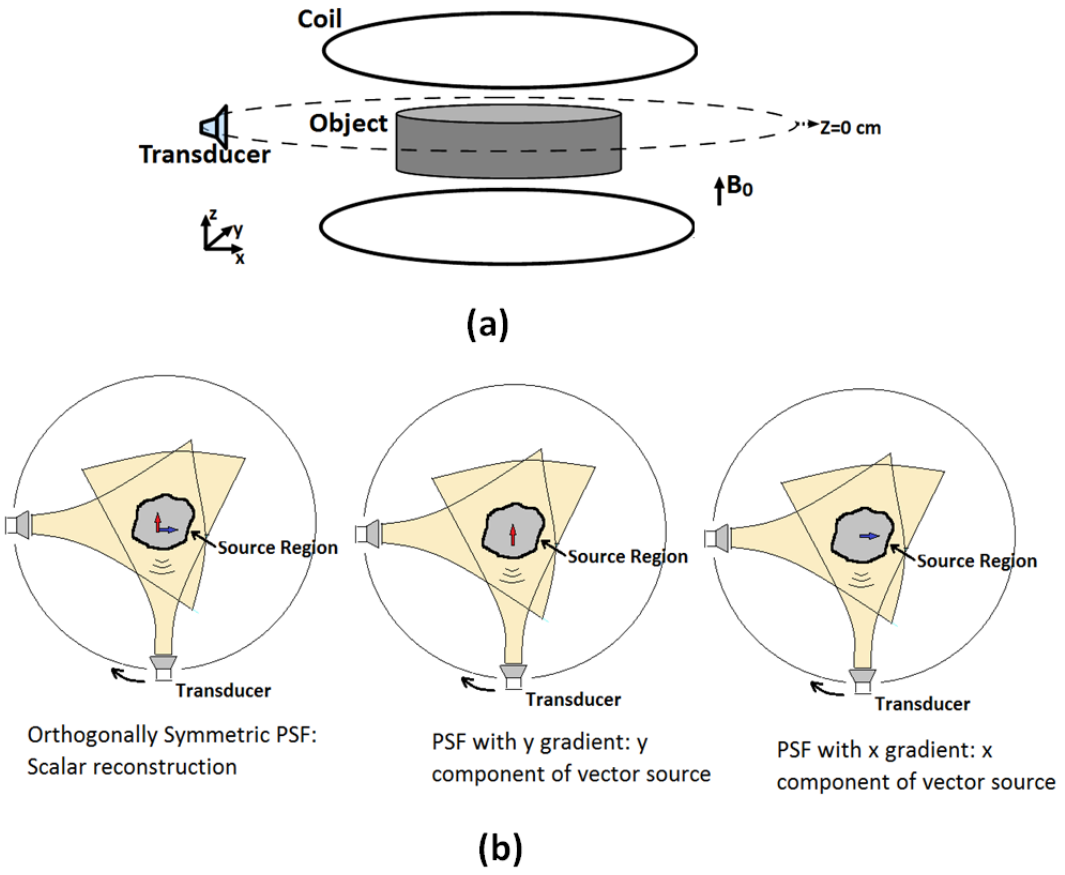

Fig. 19, (a) Schematic diagram of MAT-MI imaging method (b) Schematic representation of the point spread function for scalar and vector reconstruction

The acoustic pressure measured by the ultrasound scanning setup is determined according to the Green's function solution to wave equation as given in (4.7). The piston transducers used in the simulation are assumed to have a receiver bandwidth of 100% around the central frequency which corresponds to ~70% bandwidth in a pulse echo system consisting of limited bandwidth to transmit and receive. The transducers are placed on a circular scanning geometry 30 cm away from the center of the object on a Z=0 plane. The 30 cm scanning radius leads to an approximately uniform sensitivity over the object space. Thus, the piston transducer can be assumed to be acting as a point receiver. The large scanning radius also ensures that the spherical acoustic waves from the MAT-MI source can be approximated as plane waves at the transducer, which allows for the ultrasound imaging setup to also be approximated as a 2D system. The weightings and the time delay for the beamformation are determined according to equation (4.12). The time delays with a discretized pressure signal can be applied as $t_a = n\Delta T$, where n is an integer with $n = -\frac{N}{2} to \frac{N}{2}, \left|\frac{N}{2}\right| \Delta T$ as the maximum delay and ΔT the time between samples. This set of weightings and the corresponding time delay applied to each line of transducer signals, prior to the summation of the signals from all the transducer locations, can be considered as an N+1 tap finite impulse response (FIR) filter acting on the received pressure signal which is combined in the beamformation algorithm to reconstruct the acoustic source distribution. Under limited bandwidth data collection in the presence of noise, to obtain an ideal spatial impulse $\delta(\boldsymbol{r}')$, as the point spread function, such a filter would act as an inverse filter increasing the signal bandwidth and amplifying the noise. So in the design of the beamformer, $N = 0$ is used which would

lead to the design of a point spread function with non-ideal spatial pulse $D(\boldsymbol{r}')$ approximating the desired spatial impulse response $\delta(\boldsymbol{r}')$. In the simulation, the function $D(\boldsymbol{r}')$ is set to the imaging point spread function obtained for the pressure source reconstruction with the backprojection algorithm for the given scanning setup. For determining the beamformation design, a source region, $\boldsymbol{r}'$, of 18×18 mm with a spacing of 0.15 mm is considered. A least square truncated singular value decomposition (tsvd) solution to equation (4.12) is used to solve for the weights.

Inverse filtering is performed on the reconstructed vector source image, which has improved signal-to-noise ratio (SNR) compared to the 1D signal obtained at the transducer due to the summation process in the beamformation algorithm,the filtered image gives a more complete estimation of the source distribution and the conductivity is then determined from this source image according to the description above.

The result of the vector source reconstruction under noise free condition is shown in figure 20. Figure 20(a) shows the conductivity distribution of the simulated object and figure 20(b) shows the induced MAT-MI acoustic source distribution for the object. To verify the proposed Helmholtz decomposition to obtain the rotational component of the induced current, the acoustic source distribution was obtained with two methods, one using the induced current $\boldsymbol{J}$ and the other with the rotational componentof the current $\boldsymbol{J_c}$ as described in the theory section. The two source distributions were compared and were found to be approximately equal. A portion of the induced current density is seen in figure 20(c) and the corresponding reconstructed current density is seen in figure 20(d).

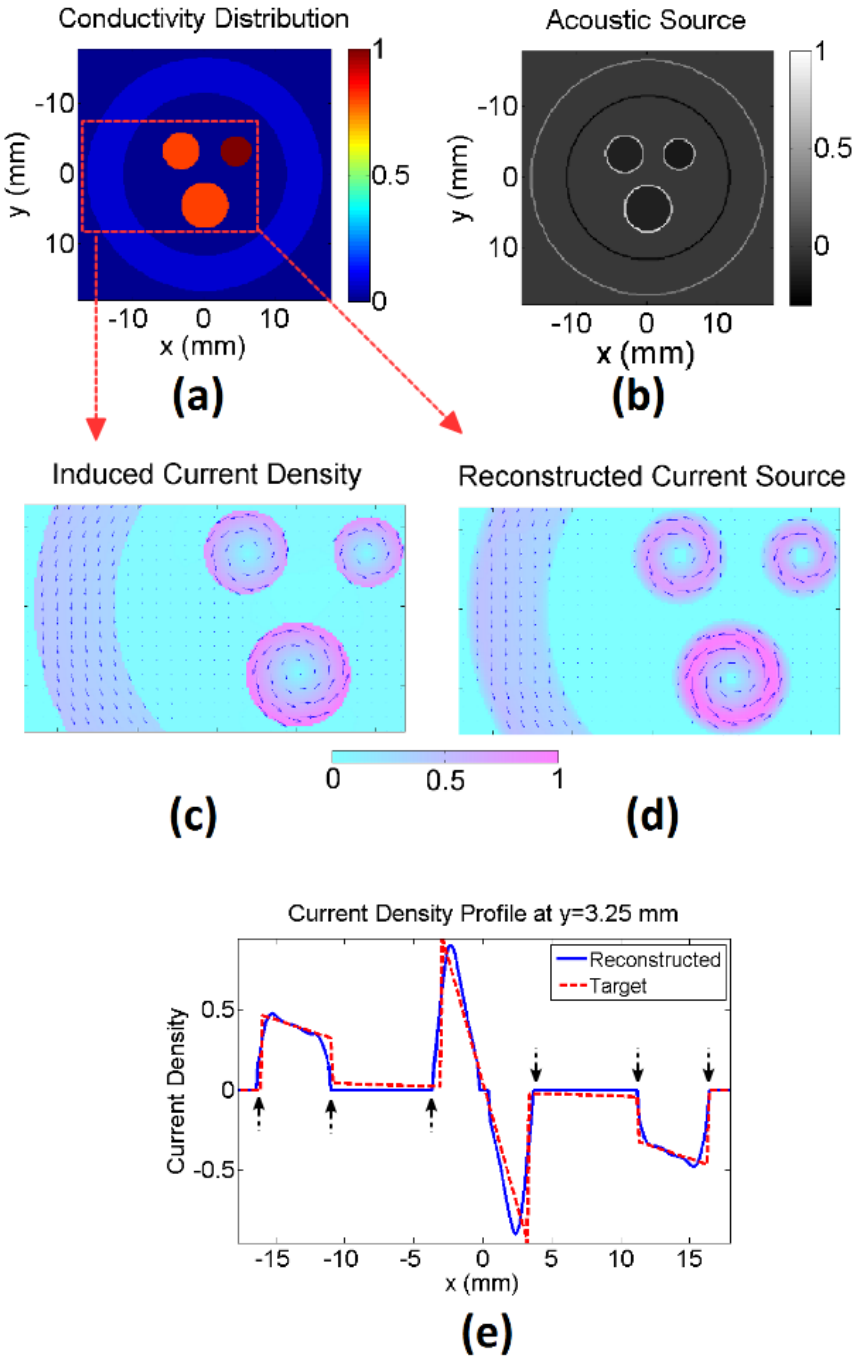

Fig. 20, (a) Simulated conductivity distribution. (b) Induced acoustic source in the object. (c) Induced current density. (d) Reconstructed current density.(e) Current density profile through y=3.25 mm of $\boldsymbol{J}_y$, the arrows mark the conductivity boundaries.

The induced eddy currents are cyclic, as seen in this figure, due to the magnetic vector potential generated by the coils being cyclic. The individual orthogonal components of the reconstructed vector source ,$\boldsymbol{J_x}$and $\boldsymbol{J_y}$, have phase inversion about the x and y axis, respectively, due to the cyclic nature of the current. Figure 20(e) shows a line profile of the reconstructed current source with the points of conductivity boundaries marked by arrows. Due to the limited bandwidth of the imaging system, spatial smoothing is observed in the reconstructed current density, especially at the conductivity boundaries where a sharp change in the current density is expected.

The results of the vector source reconstruction, with the designed PSF, and the conductivity estimation for an object is shown in figure 21. Figure 21(a) shows the conductivity distribution of the simulated object, and the normalized current density corresponding to the induced current source due to the applied magnetic pulse is shown in figures 21(b) and (c). As the induced eddy currents are cyclical in nature, the individual vector components have phase inversions about the orthogonal axis as seen in the figure. The estimated conductivity distribution and the reconstructed vector current source are shown in figures 21(d), (e) and (f) respectively. Figures 22(a) and (b) show a line profile of the reconstructed conductivity and the current source respectively when x=0. As seen in the line profile of the current source, due to the limited bandwidth of the imaging system, spatial smoothing is observed in the reconstructed current density, especially at the conductivity boundaries where a sharp change in the current density occurs. This smoothing effect in the reconstruction on current density leads to the estimated conductivity to have maximum error at the boundaries of the object.

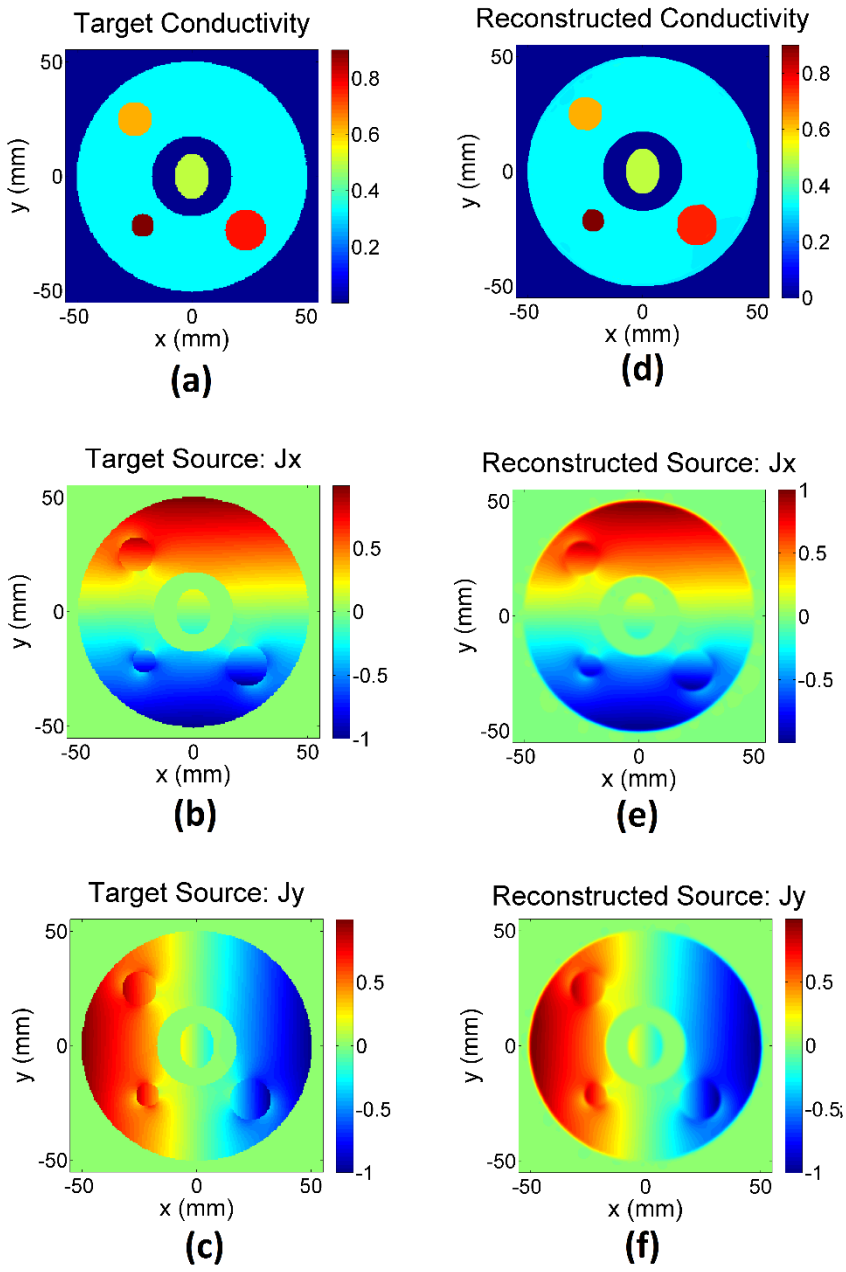

Fig. 21, (a) Simulated conductivity distribution. (b), (c) Induced current source, orthogonal components Jx, Jy. (d) Reconstructed conductivity distribution.(e), (f) Reconstructed current density orthogonal components Jx, Jy.

To reduce this error, the conductivity in this region over 3 mm corresponding to the boundary spread is estimated by extrapolating the conductivity at the neighboring points which leads to reliably reproducing the target conductivity as seen in the line profile of the reconstructed conductivity.

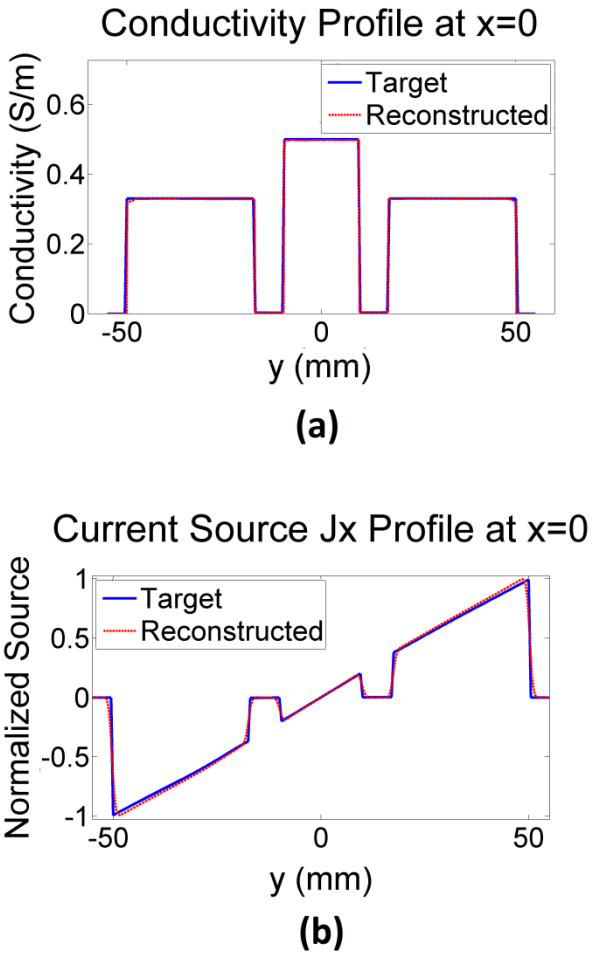

Fig. 22, (a)Line profile of the reconstructed conductivity distribution at x=0 (b) Line profile of the current density component Jx at x=0

The conductivity reconstruction from vector source imaging is seen in figure 23 for various noise levels. Figure 23(a) shows the conductivity distribution of the simulated object. Figures 23(b), (c), and (d) show the conductivity reconstruction for SNR levels of 50, 10 and 1, respectively. The reconstructed conductivity values when compared to the target have correlation coefficients (CC) of 99.6%, 99.2%, and 98.3%, respectively. The

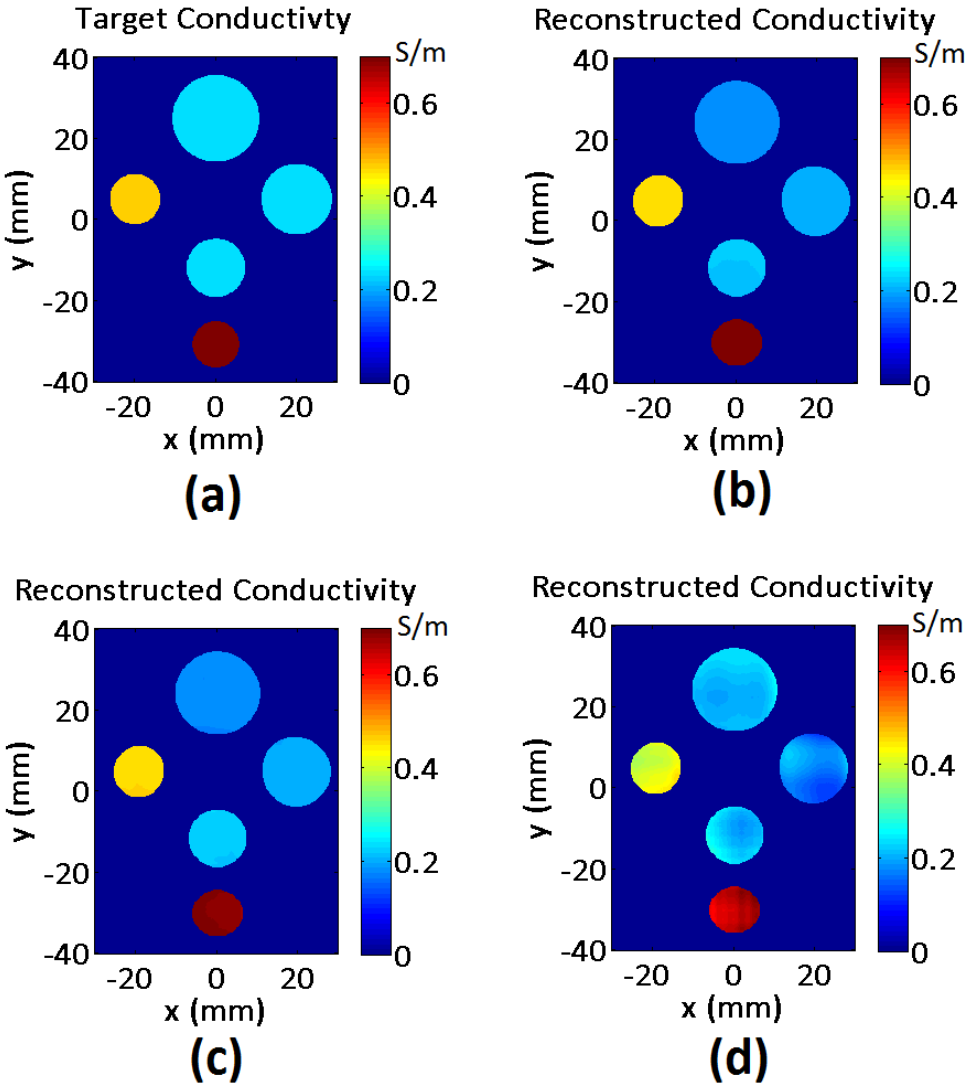

Fig. 23, (a) Target conductivity image. (b), (c) and (d) Reconstructed conductivity images with SNR of 50, 10 and 1, respectively

corresponding relative error (RE) is 6.3%, 10.87%, and 24.68%, respectively. Due to the smoothing effect of limited bandwidth reconstruction on current density, the estimated conductivity at the boundaries of the object have the maximum error. To reduce this error, the conductivity in this region around the boundary is estimated by extrapolating the conductivity at the neighboring points.

Figure 24 shows the point spread function designed using the vector beamformer algorithm to obtain the orthogonal components of the current source in MAT-MI. Figure 24(a) shows the simulated system impulse response and figure 24(b) shows the resultant imaging point spread function (PSF) for the scalar pressure source reconstruction using the backprojection algorithm. This PSF is a limited bandwidth approximation to a spatial impulse function and is used as one of the components of the target vector PSF with a zero valued function as the other component as shown in figure 24(c). The vector PSF in figure 24(c) with its x and y components can reconstruct the x component of the current source distribution, and a vector PSF with these x and y components interchanged could be used to image the y component of the current source distribution. The weights and time delay applied to the aperture are designed according to the proposed method, and the resultant vector PSF, approximating the target spatial function, obtained with the method is shown in figure 24(d) with the aperture weights necessary to obtain this PSF shown in figure 25(a). The image reconstructed with this bandwidth limited PSF is further filtered to obtain a more complete estimate of the source distribution, and the resultant spatial function with the inverse filtering applied to the bandwidth limited PSF would be the

imaging PSF for the estimated vector source distribution. So, this inverse filtered spatial function determines the resolution of the reconstructed image.

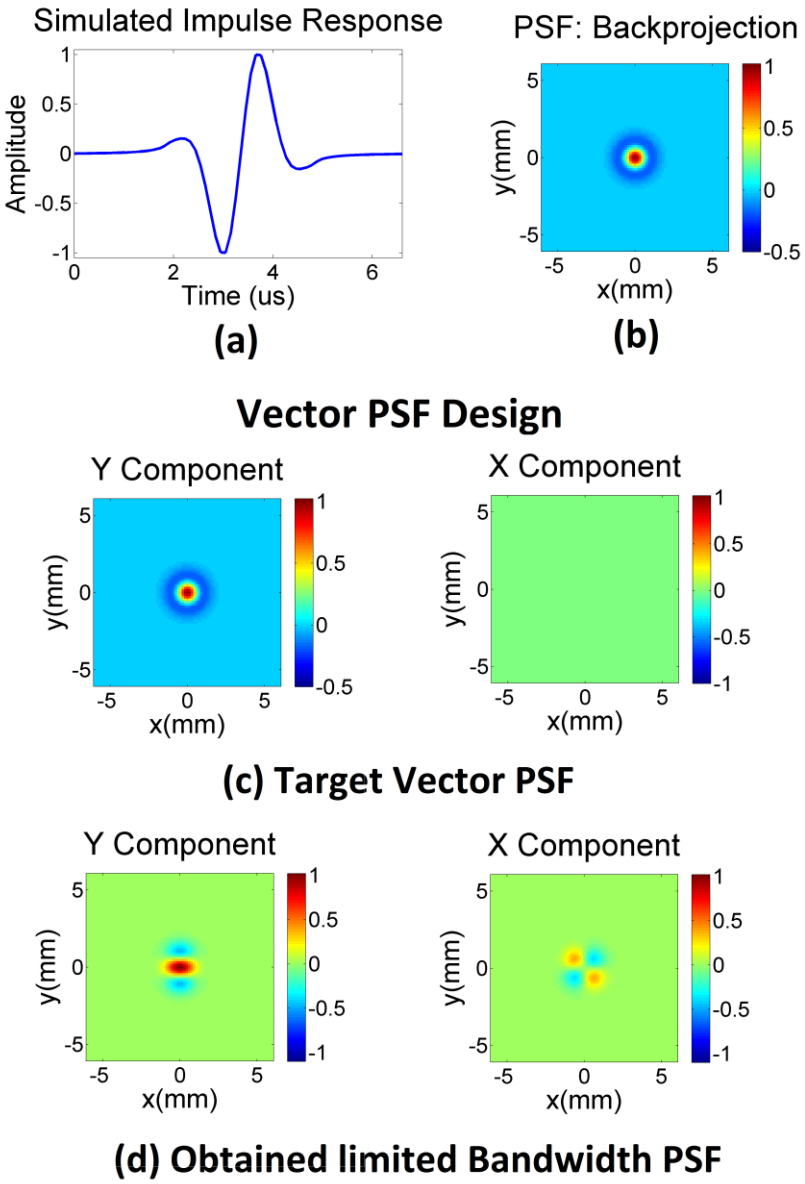

Fig. 24, (a) Simulated PSF of the ultrasound system (b) resultant PSF for acoustic source imaging (c) Target PSF for vector source reconstruction to obtain Y component of the vector source (d) PSF obtained from the beamformation algorithm

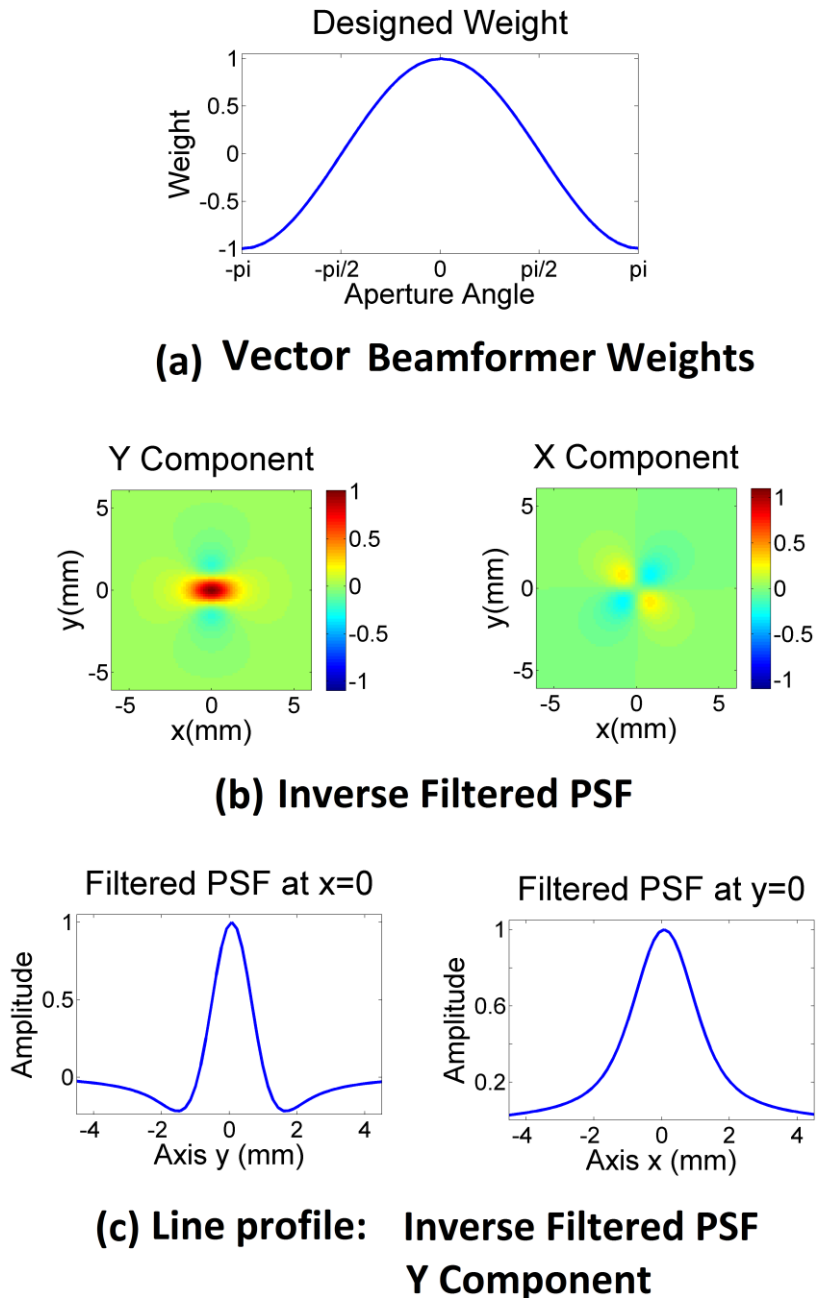

Fig. 25, (a) Weights applied to the aperture to obtain the vector PSF obtained from the beamformation algorithm (b) PSF obtained after inverse filtering which leads to a more complete imaging of MAT-MI sources (c) Line profiles of the PSF from which the imaging resolution can be estimated

The line profiles of this function along the two orthogonal axis are shown in

figure 25(c), and the full width half maximum (FWHM) of this function, which is the imaging resolution for the given system bandwidth, is between 1.5-2 mm along both the orthogonal direction.

The resolution of the imaging system determines the size of the object that can be reconstructed reliably. We have simulated the ability of MAT-MI to reconstruct the conductivity distribution of objects with different sizes under various system frequencies as seen in figure 26. The resolution of the imaging system, as determined by the point spread function, increases with frequency bandwidth of the imaging system as seen in Figure 26(a), which shows the line profiles of the PSF for imaging system frequencies of 300 kHz, 500 kHz and 2.5 MHz with the half width half maximum (HWHM) marked in the plot. The HWHM is half the resolution of the imaging system, and the resolutions at these frequencies are obtained as ~ 2.5, 1.5 and 0.3 mm respectively. The target object imaged in this simulation, as shown in Figure 26(b), consists of conductive circular objects with diameters of 4.5, 3, 1.5, 0.5 mm in a non-conductive background. The reconstructed conductivity images at different system frequencies are shown in figures 26(c), (d), (e) corresponding to 2.5 MHz, 500 kHz and 300 kHz respectively. As seen in the reconstructed image, objects larger than the resolution of the imaging system are reliably reconstructed.

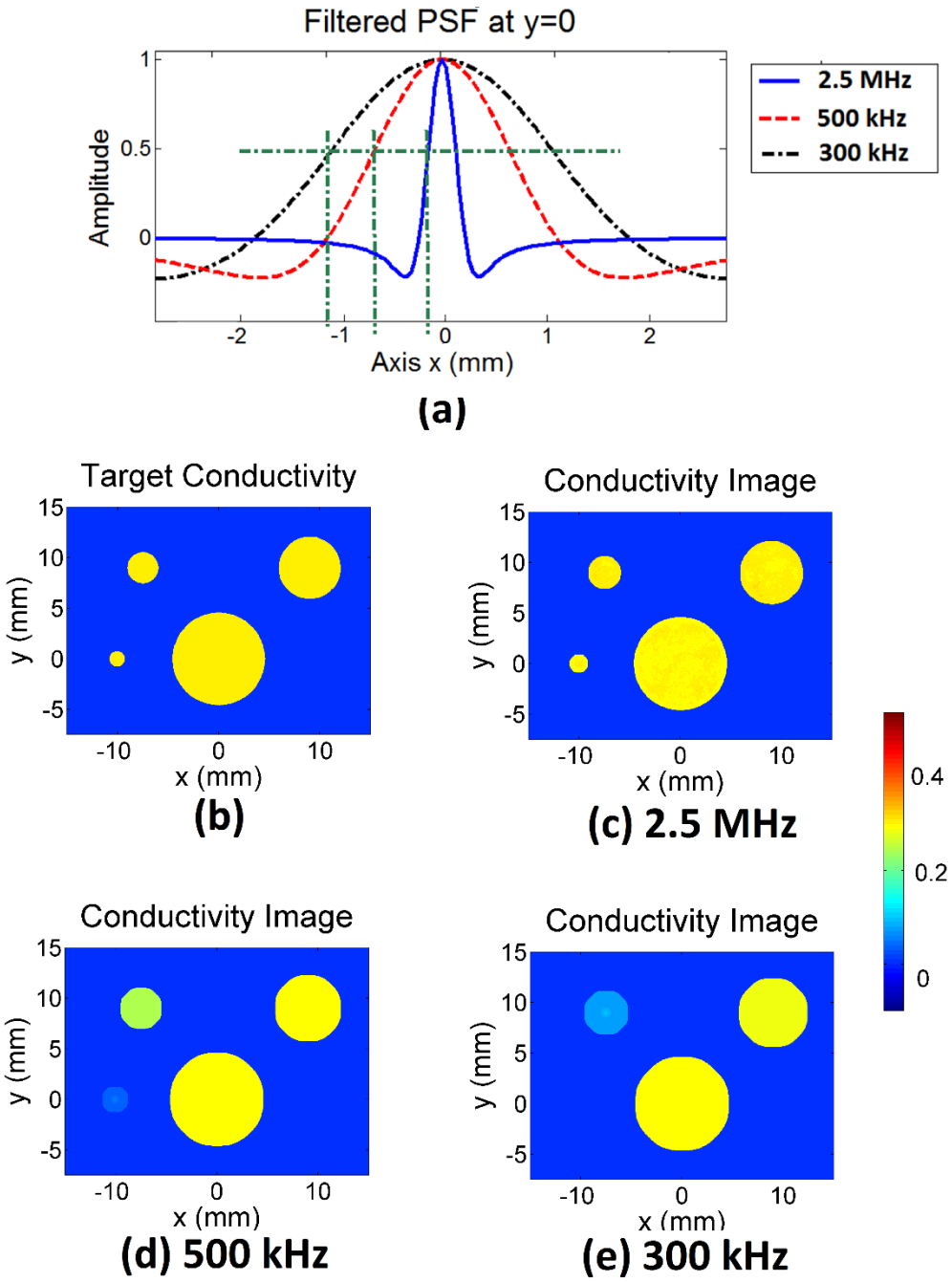

Fig. 26, (a) Line profiles of the PSF at 2.5 MHz, 500 kHz and 300 KHz center frequency with the HWHM of the PSF marked. (b) target conductivity distribution. (c), (d) and (e) reconstructed conductivity distribution with ultrasound frequency at2.5 MHz, 500 kHz and 300 KHz respectively

Further, we have tested the imaging method to reconstruct anatomically realistic objects applicable to human imaging. For this we adopt 3D numerical breast phantoms from the online repository developed and maintained by the University of Wisconsin Computational Electromagnetics Laboratory (UWCEM) (Zastrow *et al* 2008). The repository phantoms are derived from MRIs of healthy breasts, and thus convey the realistic shape and internal adipose (fatty) and fibroglandular tissue structure of the breast. The range of dielectric properties assigned to each tissue type (adipose, transitional, or fibroglandular) are derived from conductivity measurement studies reported in the literature (Zou and Guo, 2003, Gabriel *et al* 1996). The repository

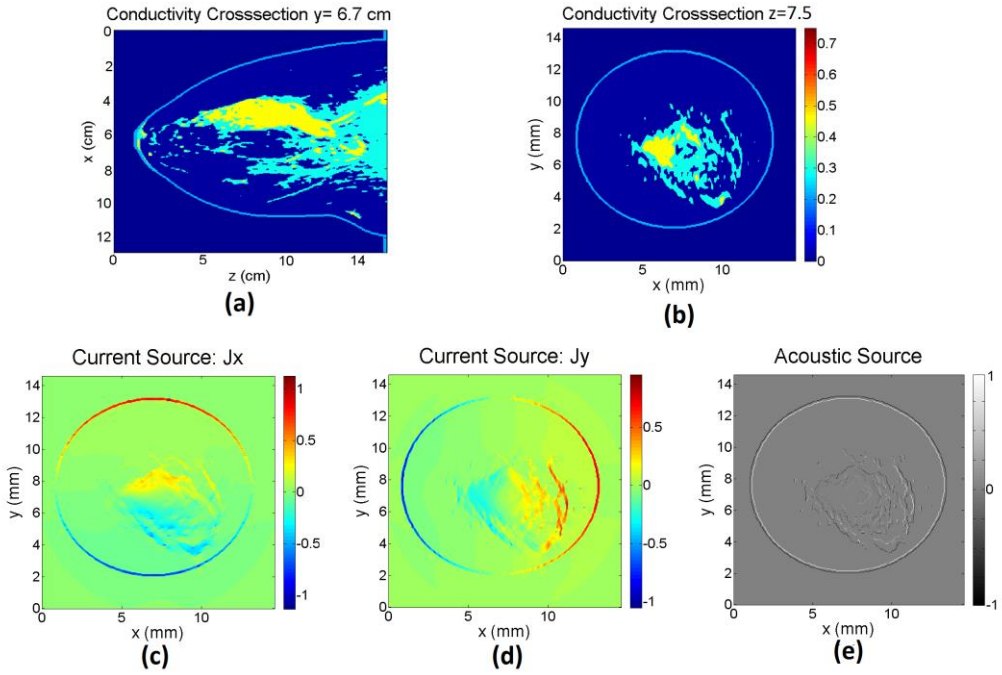

Fig. 27, (a) Cross-section of the simulated conductivity breast phantom along the y axis (b) cross-section of the phantom along z axis (c)-(d) induced current source in the cross-section along z axis shown in (b) (e) resultant acoustic source in this cross-section

phantoms are defined on a uniform 0.5 mm voxel grid and include a homogeneous skin layer and a chest wall. A 3D focused circular scan is used for the ultrasound imaging for reconstructing crossections of the phantom in the x y plane. In the simulation study, ideal focusing along the z axis is assumed to be available.

Figure 27 shows the forward simulation with the breast phantom, and the simulated conductivity cross-section of the phantom along 2 perpendicular planes are shown in figures 27(a) and (b). The induced vector current sources are shown in figures 27(c) and (d) in the phantom crossection shown, and the induced acoustic source arising from this vector source is shown in figure 27(e). It can be seen from figure 27 that the MAT-MI currents are induced in the conductive fibroglandular tissue and hence the induced acoustic source is also the strongest in this tissue region. The conductivity reconstruction result in the simulated breast phantom can be seen in figure 28 along the crossesction of the ultrasound scanning plane. The target and the reconstructed conductivity along this plane at different z locations are shown in figures 28(a)-(f), and in figure 28(g) a line profile of the reconstructed conductivity compared to the target is plotted.

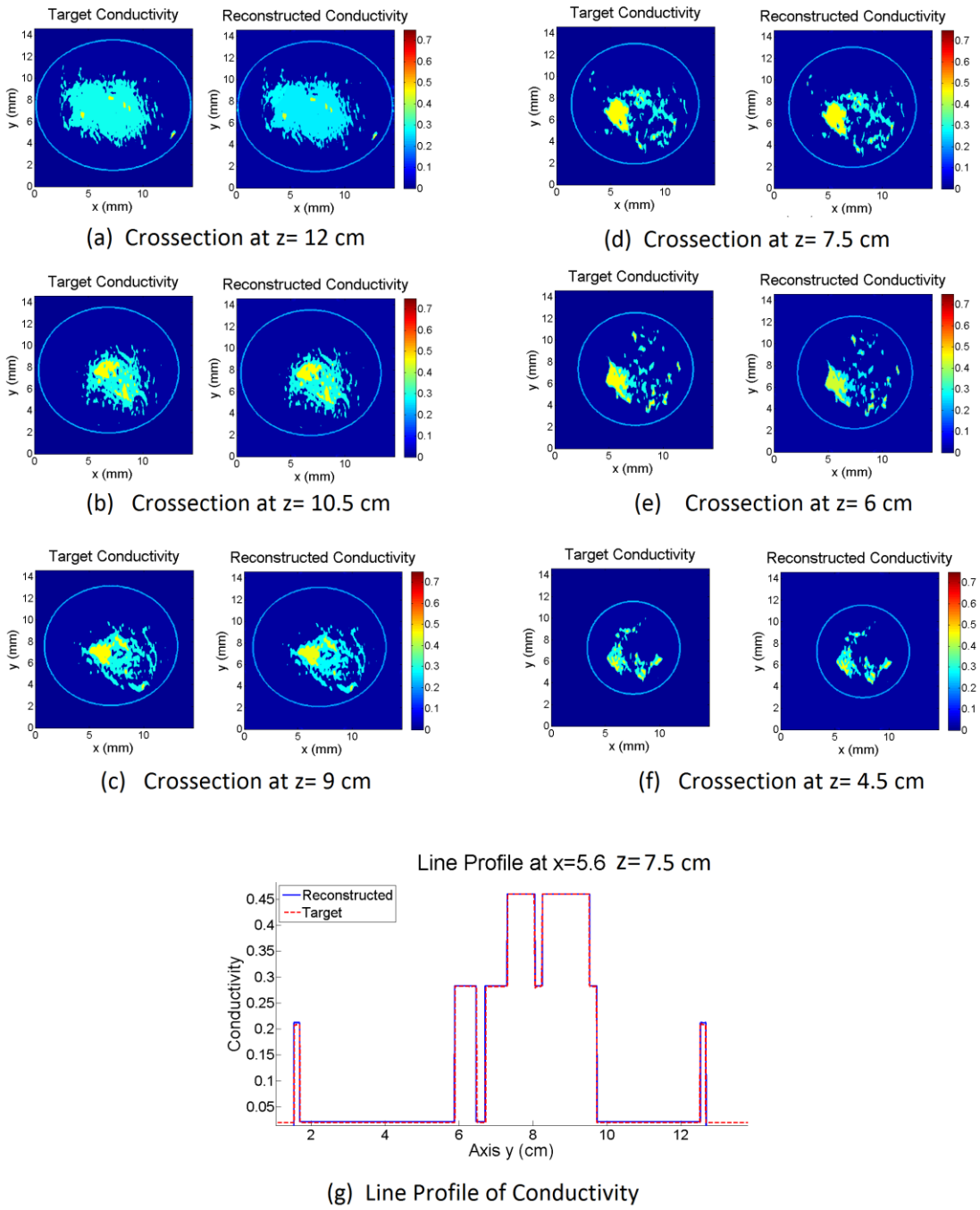

Fig. 28, (a) –(f) Cross-section of the target and reconstructed conductivity of the breast phantom at various Z levels (g) line profile of the reconstructed and target conductivity

4.4 Experiment Study

We have evaluated the proposed conductivity reconstruction method in MAT-MI experiments. The typical experiment system used in this study has a similar design to the schematic setup shown in figure 29. The static magnetic field $\boldsymbol{B_0}$ is applied with two permanent magnets used like a Helmholtz pair to get an approximately uniform magnetic field of 0.2 T (Gaussmeter, Alpha Laboratory) between them. Two coils of three turn each, and arranged as a Helmholtz pair they are used to generate the pulsed magnetic field $\boldsymbol{B_1}$. A stimulator based on a transistor switch was developed to drive these coils. The current flowing in the coils has a waveform approximating a bipolar single cycle sinusoid, which lasts 2μs and gives a center frequency of 500 kHz which matches with the bandwidth of the ultrasound imaging transducer. The dynamic magnetic excitation generated by the stimulating coils was measured by a sensing coil with a radius of 1.5 cm connected to an oscilloscope. The estimated maximum current changing rate in the coils is 1.5e8 A/s, which corresponds to a magnetic field changing rate of 6e3 T/s at the coordinate center. The maximum dynamic magnetic field strength $\boldsymbol{B_1}$ is estimated to be around 0.006 T at the coordinate center. The MAT-MI acoustic signal measurement was conducted using a circular scanning scheme. During experiments, both the sample and the transducer were submerged in a distilled water media for acoustic coupling. A 500 KHz flat transducer (Panametrics V301) with a 29 mm diameter and around 60% bandwidth was employed in this study. The transducer was mounted to a scanning frame driven by a stepper motor that can scan around the sample over a 320° view angle and 2.0° scanning step. The scanning radius was about 20 cm. While scanning, the object and

the magnetic field setup are fixed in position to reliably acquire the acoustic measurements. The acoustic data collection is synchronized with the magnetic excitation. Again, as in simulation, the uniformity along Z direction of conductivity distribution of the object and the uniformity of the magnetic fields and the implemented scanning setup allows the corresponding MAT-MI problem to be simplified as a 2D problem. The acoustic signals collected using this transducer were fed into preamplifiers with a 90 dB gain and digitized by a 5 MHz data acquisition card. Signal averaging was used to increase SNR. After each experiment, the conductivity of the sample was measured using a four electrode probe (Hu and He 2010). The conductivity distribution reconstructed in

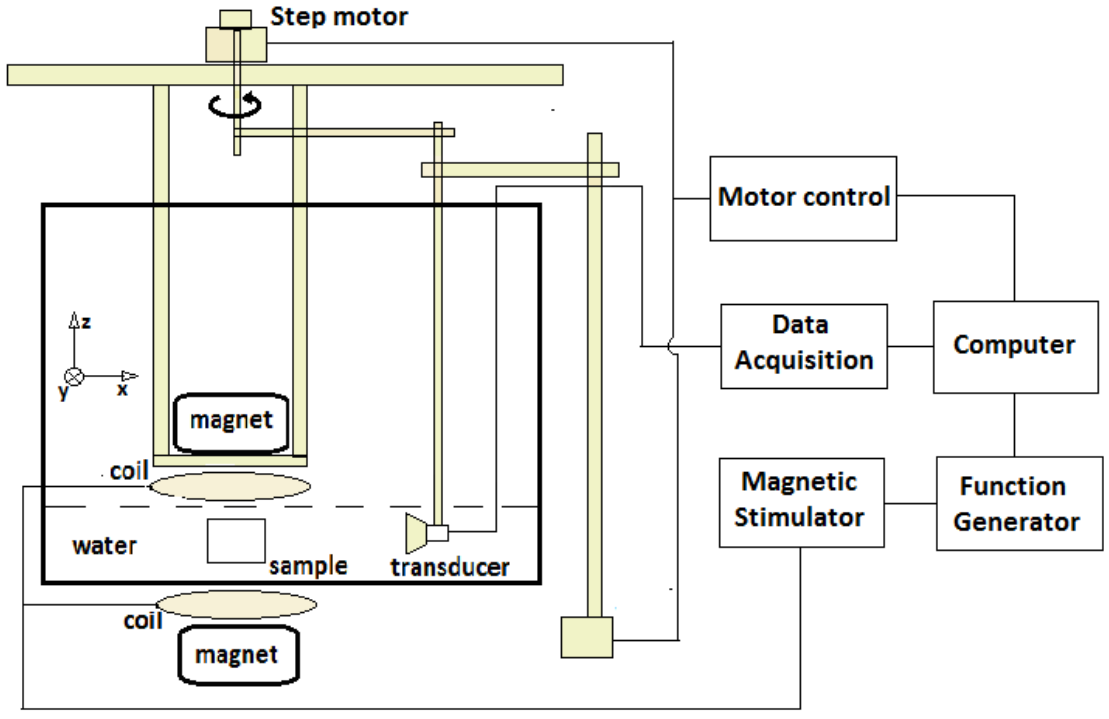

Fig. 29, Schematic diagram of experiment setup

experiments was normalized to the expected range of values using a scaling factor to account for the various gains in the system. The scaling factor was determined by estimating the conductivity of a 50 mm diameter test sample of 0.6 % salinity whose conductivity was measured to be 0.98 S/m using the four electrode probe.

In the experiments, the time varying magnetic field leads to electromagnetic interference (EMI) at the ultrasound transducer. This continues for a certain time duration due to the turn off transients associated with the stimulator and the impulse response of the transducer. The observed EMI signal in the experiment data is seen to have significantly low frequency variations. This noise on backprojection leads to slow varying spatial signals, which interferes with the reconstruction of the desired low spatial frequency component of the vector source distribution. This leads to errors in conductivity estimation, so the received acoustic signal is bandpass filtered to eliminate most of the interfering low frequency and high frequency noise. A simple filter implemented (Xu and Wang 2002) for this purpose in frequency domain is:

$$F(f) = \begin{cases} 1, & 100\ kHz < f < 900kHz \\ 0, & otherwise \end{cases}$$

Further, a hanning window based filtering is applied to the estimated conductivity image to improve the SNR of the reconstruction. Such a filter can be designed as follows:

$$H(n,n) = h \times h'$$

where

$$h(n,1) = 0.5 * \left(1 - \cos\left(2 * \pi * \frac{0:n-1}{n-1}\right)\right), n = 6$$

where n is the width of the hanning window filter H. We have evaluated the proposed technique in phantom experiments.

Phantoms made of pork skin gel were used in these experiments. Figure 30(a) shows a tested phantom photographed after the experiment. The phantom was made with a 0.4 % salinity gel in the background with a diameter of 5cm. A 2.5 cm diameter cylindrical column is embedded in the gel. This region is filled with 1.2% salinity gel after the background gel is set. The conductivity values 0.4% and 1.2% saline solutions are 0.67 S/m, 2.01S/m respectively. A photograph of the phantom was taken immediately after the experiments with a black dye applied to the inner layer for photo contrast enhancement. The reconstructed acoustic source distribution is shown in figure 30(b), and as expected with limited bandwidth reconstruction, the acoustic source is mainly distributed around the conductivity boundaries in the object. Using the vector imaging method, the MAT-MI current source components were reconstructed as shown in figures 30(c) and (d). The cyclical nature of the induced current can be seen in this figure, and the current density is stronger in the higher conductivity inner region as compared to its neighboring lower conductivity region. Figure 30(e) shows the estimated conductivity distribution using the reconstructed vector source. A conductivity profile at x=-1mm is shown in figure 30(f). The reconstructed conductivity distribution seen in these results represents well the expected conductivity of the tested phantom. The extrapolation of conductivity values at the boundary gives a good fit with the expected conductivity profile for the piece wise homogeneous objects.

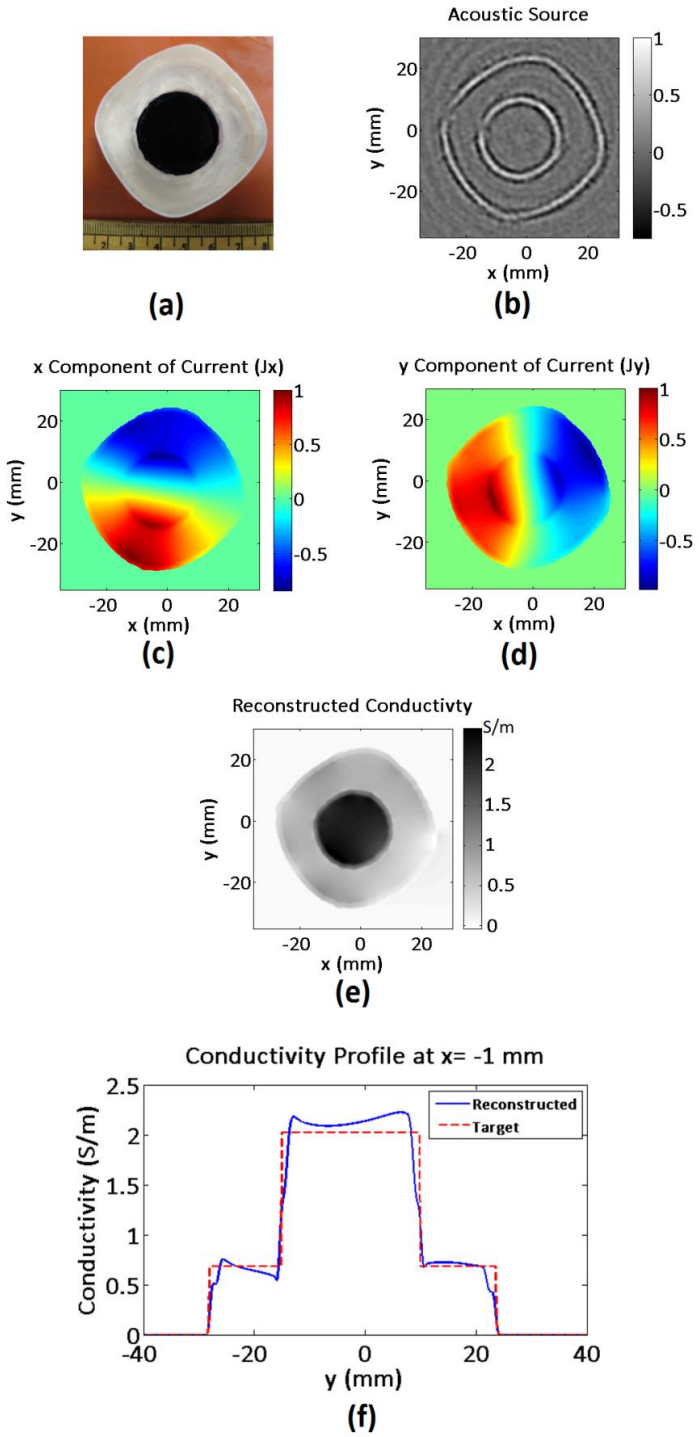

Fig. 30, (a) Photograph of the gel phantom tested. (b) Reconstructed acoustic source distribution. (c) Reconstructed x component of the current: $\boldsymbol{J_x}$. (d) Reconstructed y component of the current: $\boldsymbol{J_y}$. (e) Reconstructed conductivity distribution. (f) Conductivity profile at x=-1mm showing the comparison between the target and reconstructed conductivity value.

We also tested, in experiments, the imaging contrast of the reconstruction technique, as this is an important index for biological imaging. Figure 31(a) shows the photograph of the phantom imaged in this experiment; the phantom consists of a conductive 25 mm square block placed in non-conductive background. Three different samples with 0.3%, 0.6% and 0.9% salinity were prepared for this experiment. The conductivity of the samples were measured to be 0.54, 0.97, and 1.52 S/m, respectively. The reconstructed conductivity images are shown in figures 31(b), (c) and (d)

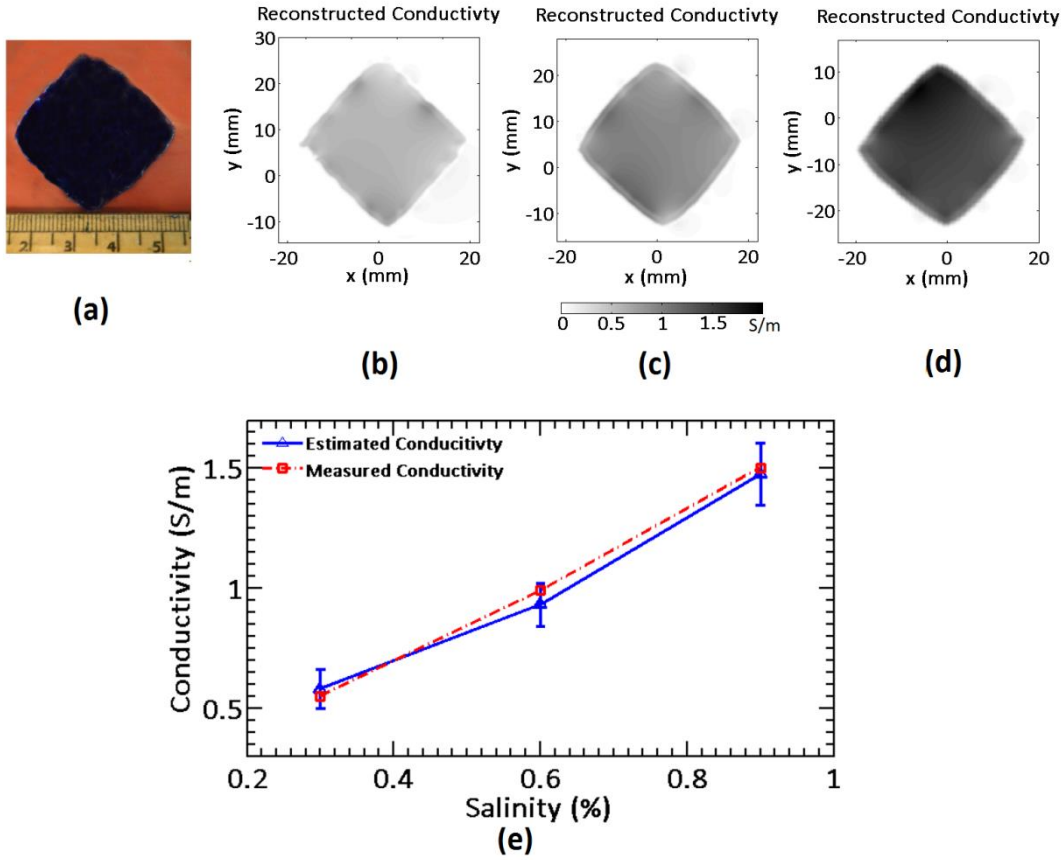

Fig. 31, (a) Photograph of gel phantom used in the study. (b),(c) and (d) The reconstructed conductivity distributions corresponding to phantoms with salinity 0.3%,0.6% and 0.9% respectively

corresponding to the phantoms with 0.3%, 0.6% and 0.9% salinity, respectively. Figure 31(e) shows the plot of the estimated and measured conductivity against the salinity of the phantom. The mean estimated conductivity of the three samples was 0.57, 0.92 and 1.48 S/m respectively. It can be seen from the error bar in figure 31(e) that approximately 10% variation is seen in the reconstructed conductivity.

Spatial resolution is another important index for biological imaging. Figure 32(a) shows the photograph of the phantom imaged. The phantom consists of two square gels of 0.9% salinity embedded in a background gel of 0.4% salinity. The embedded blocks have a dimension of 9 and 13 mm, respectively. The reconstructed image is shown in Figure 32(b); it agrees with the original sample well. Specifically the relative location and size of the square gel are clearly resolved and matches well with the phantom. A line profile at x=3mm from the reconstructed image is shown in Figure 32(c) including the two of square inclusions. The reconstructed profile as seen here is in good agreement with the original profile, which was a grayscale profile from the photo in figure 32(a). Some distortion of the object occurred around the boundary over one ultrasound wavelength, which is 3mm due to the errors in estimating the conductivity around this region.

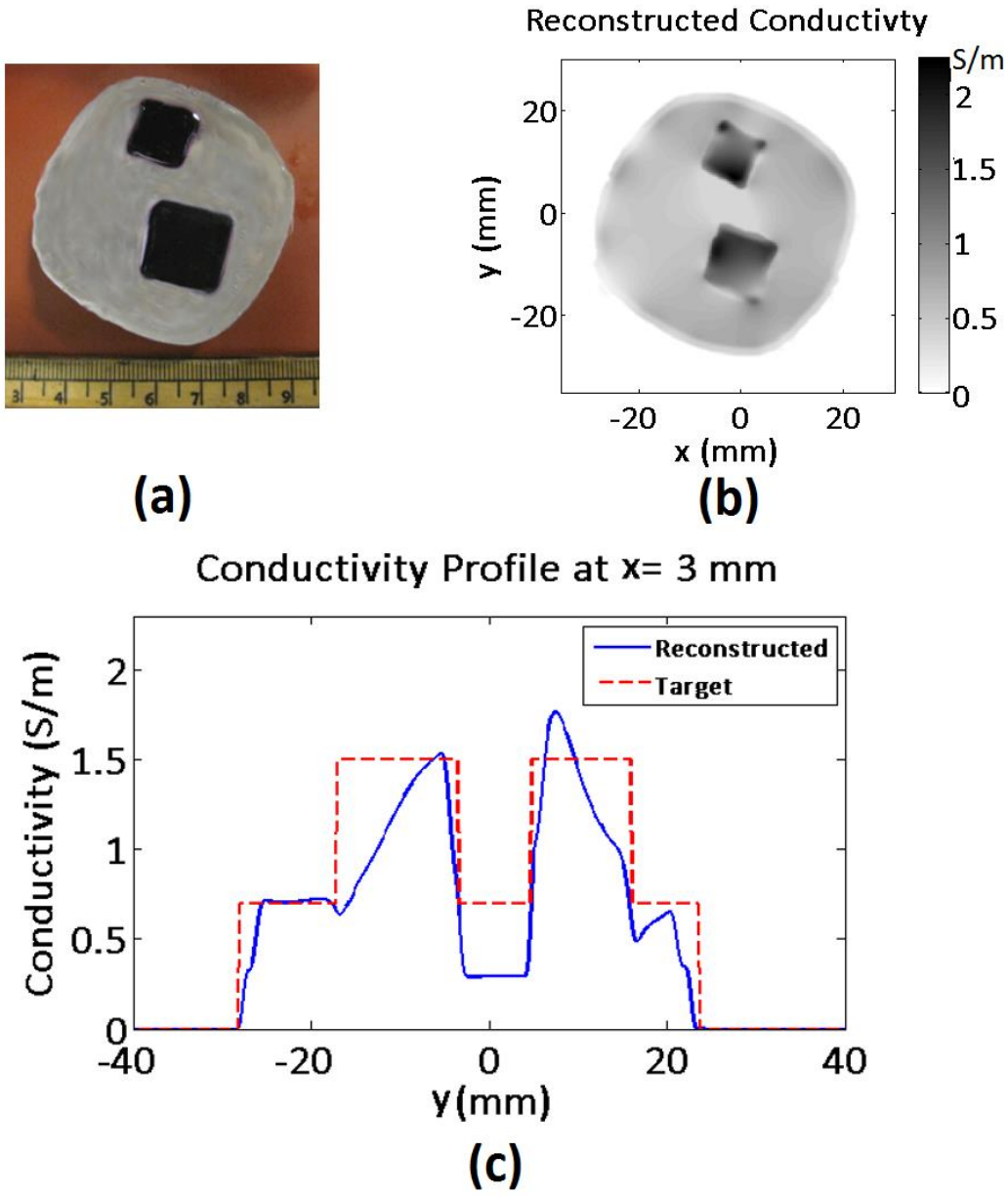

Fig. 32, (a) Photograph of the gel phantom imaged. (b) Reconstructed conductivity distribution. (c) Conductivity profile through x=3 mm comparing the reconstructed conductivity distribution with the target conductivity distribution from the photograph.

For imaging biological tissue, the experiment system under MR static field is used to obtain improved biological tissue signal. However, the strong magnetic pulse used to generate the MAT-MI signal induces electromagnetic interference (EMI) in the ultrasound imaging system. This continues for certain time duration due to the turn-off transients associated with the magnetic stimulator and the impulse response of the transducer. The observed EMI signal in the experiment data is seen to have significantly low frequency variations which could interfere with the estimation of low spatial frequency conductivity distribution, and a bandpass filter is used to suppress this noise. In the reconstructed image, additional artifacts in the form of concentric rings are observed as a result of coherent addition of weak background signal. The strength of the artifacts is comparable to that of MAT-MI sources in the reconstructed image. However, the circular nature of the artifacts can be used to filter out the rings by use of a high pass filter along the azimuthal direction at each radial location on the image. The useful MAT-MI source, present strongly at the conductivity boundary, in the limited bandwidth setup is further filtered to obtain a more complete estimate of the vector current sources and the conductivity is then determined using this source according to method described previously. The conductivity distribution reconstructed in experiments was normalized to the expected range of values using a scaling factor to account for the various gains in the system. The scaling factor was determined by estimating the conductivity of a 50 mm diameter test sample of 0.7% salinity whose conductivity was measured to be 1.2 S/m using a four electrode probe (Hu *et al* 2011).

We have performed imaging experiments on a well-controlled saline phantom as shown in figure 33. As seen in figure 33(a), the phantom consists of 0.7% cooled saline

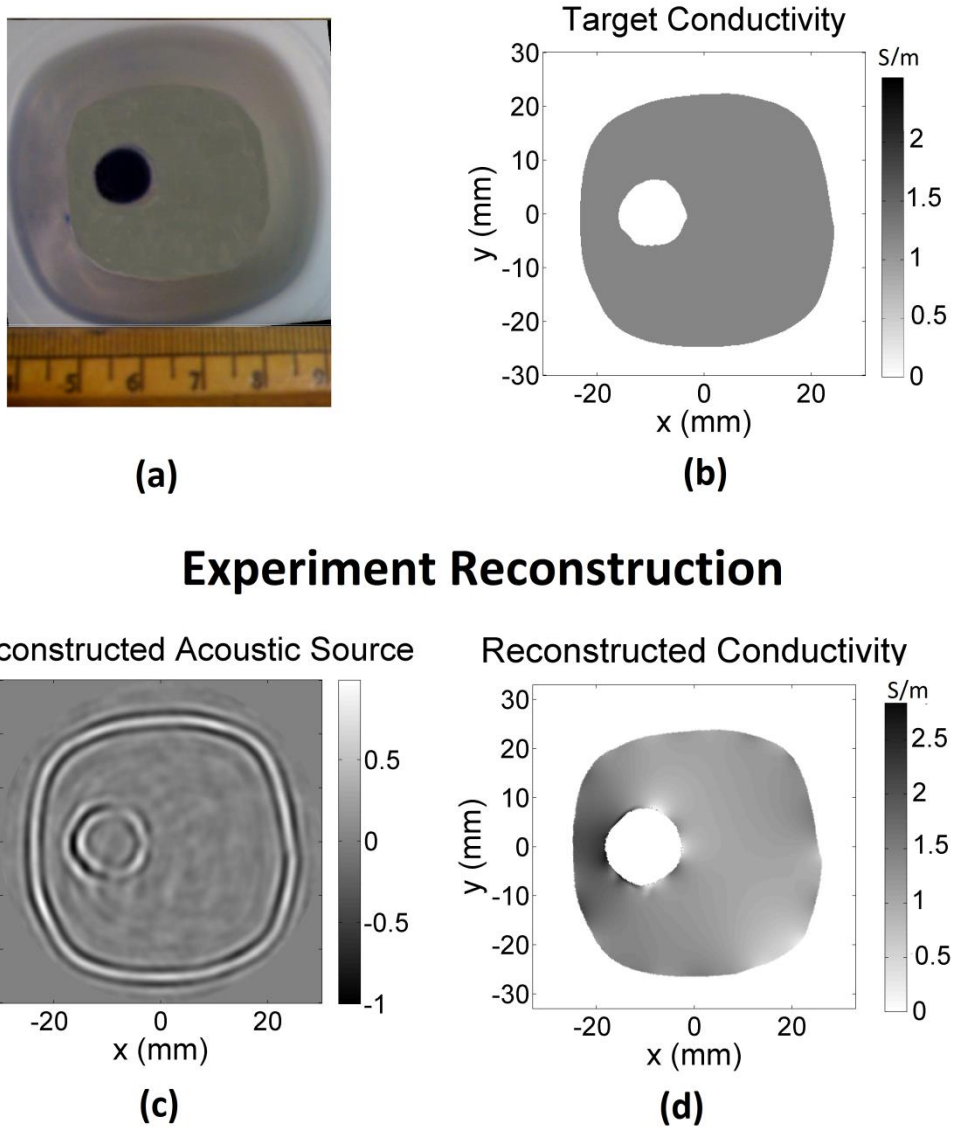

Fig. 33, (a) Photograph of the imaged saline phantom (b) simulated conductivity distribution similar to the experiment phantom (c) experiment pressure source reconstruction with the ring artifacts removed (d) reconstructed conductivity distribution with the experiment phantom.

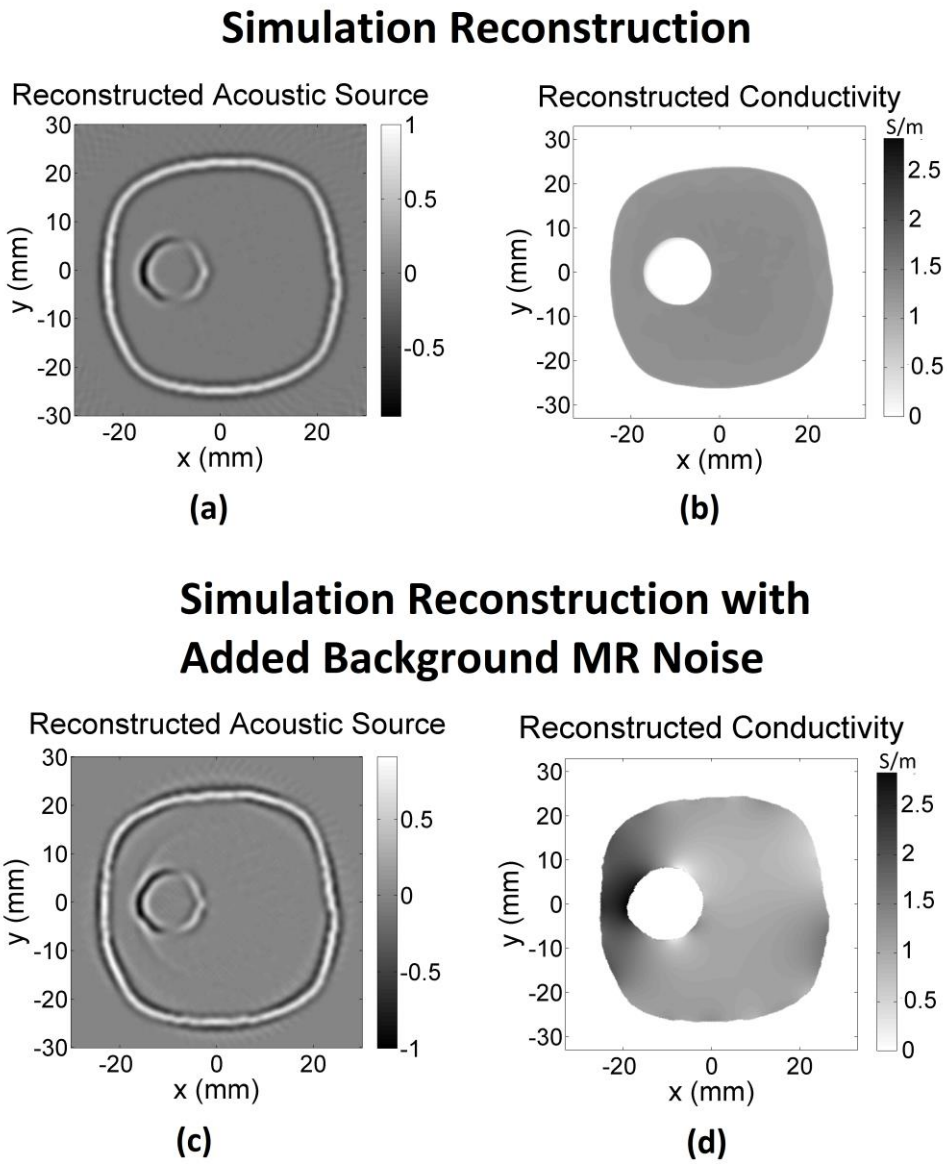

Fig. 34, (a)(b) Pressure source and conductivity reconstruction in simulation without added MR noise of the target conductivity shown in Fig32(b). (c) Filtered simulation pressure source reconstruction with background MR environment noise added to the data (d) conductivity reconstruction of the simulated phantom.

gel with a non-conductive gel structure embedded in it. A dark blue dye is applied to the surface of the non-conductive gel after the experiment for improving photograph contrast.

Also, for better comparison with the experiment result, a simulation has been performed with the target conductivity similar to the experiment phantom as seen in figure 33(b). In figure 33(c), the reconstructed acoustic source, from the experiment, can be seen and the ring artifacts induced by the background noise is filtered as described in the methods section which suppress the circular noise. Some artifacts are induced in the boundary signals due to this filtering and these errors in the boundary signal reconstruction propagates to the conductivity estimation. The conductivity distribution of the object estimated form the reconstructed vector sources are shown in figure 33(d). The simulation reconstruction under no MR environment artifact is shown in figure 34(a) and the corresponding conductivity estimation is shown in figure 34(b). Under such conditions there is no ring artifact in the reconstruction and the conductivity estimate is more reliable. In the simulation reconstruction shown in figure 34(c), common background signal measured in the MRI environment is added to each channel of the simulated pressure data and this leads to ring artifacts which is removed with the filter. The effect of the artifacts from the filtering, which is similar to the experiment reconstruction, is seen in the estimated conductivity distribution in figure 34(d).

We have further imaged phantoms consisting of biological tissue. Figure 35 shows the conductivity reconstruction result with a phantom consisting of goat muscle tissue pressed against a piece of fresh pork fat with a saline gel of 0.8% salinity placed around the sample. The tiny mechanical discontinuities at the muscle-to-fat tissue interface will not contribute much to the induced MAT-MI ultrasound signals (Hu *et al* 2011). The conductivity of the gel, the goat tissue and the pork fat is 1.4 S/m, 0.65 S/m

and 0.02 S/m respectively and the reconstructed average conductivity values are 1.3 S/m, 0.81 S/m, 0 S/m. As seen from the experiment reconstructions, due to the additional ring noise, there is around 25% error in the estimated conductivity for the objects placed in the

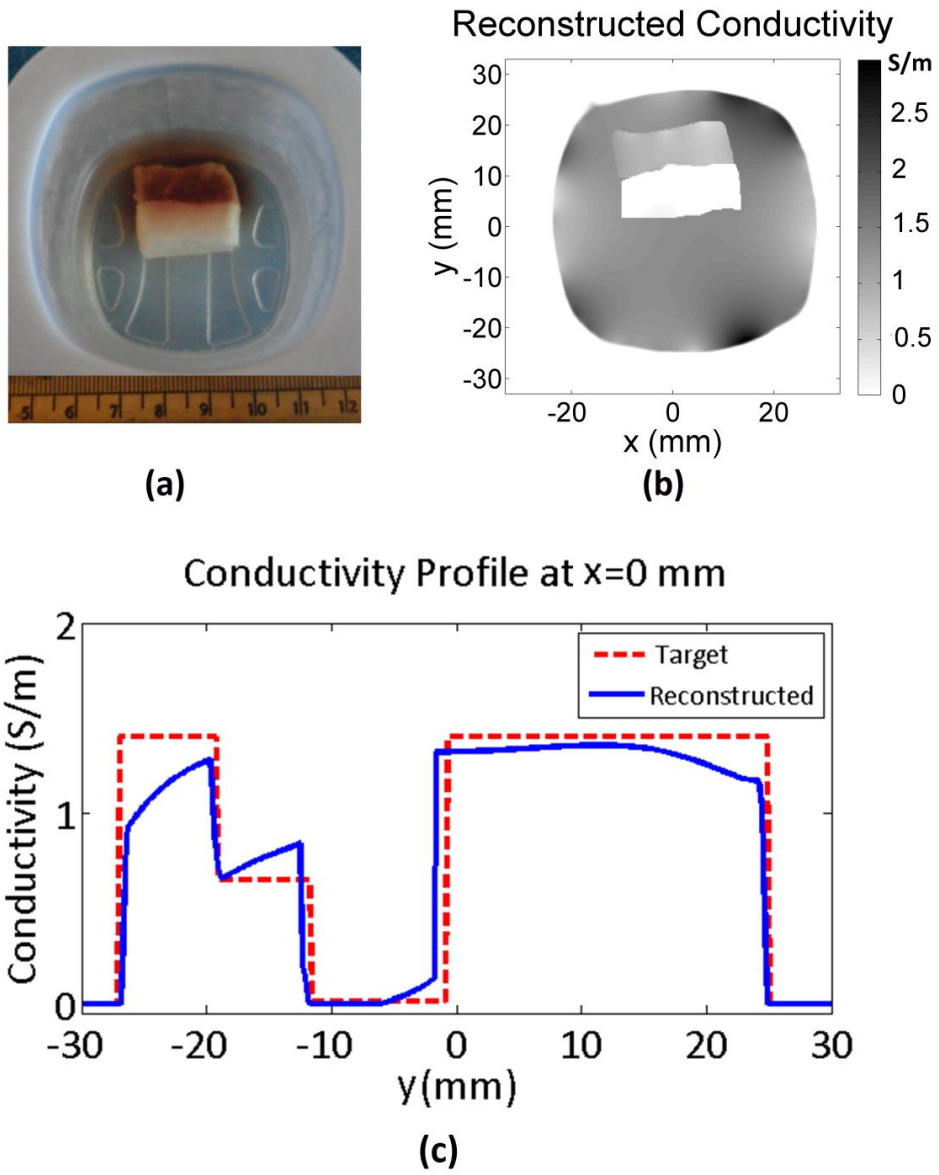

Fig. 35, Tissue phantom conductivity reconstruction (a) Photograph of a tissue phantom (b) reconstruction of the conductivity distribution (c) Line profile of the reconstruction at y=0

background gel which is the conductive structure used to determine the scaling factor for the reconstruction. However the relative conductivities of the objects are reliably imaged.

We have also performed imaging experiments on ex-vivo human liver tissue containing cancer. For these experiments, excised fresh liver sample which was obtained from a patient having previously undergone surgical removal of liver tumor were used. Pathology study of the liver tumor samples confirmed that the tumor sample was a cancerous tumor. In the first experiment we adopted a thick liver sample of 12 mm thickness and the tumor site was excised from the surrounding normal tissue. Direct conductivity measurements were performed for both tumor tissue and the surrounding tissue in ten different points (five for tumor tissue and five for normal tissue) at 0.5 MHz using a four-electrode probe (Hu *et al* 2011). The tumor tissue had conductivity of 0.65–0.70 S⁄m, while the normal tissue had a lower conductivity of 0.25–0.28 S⁄m. Following conductivity measurements, the tumor and normal tissue samples were diced into rectangular shapes with sizes of 11×4×8 and 11×5×8 mm3, respectively and a tumor phantom was composed by pressing the two tissue portions together as shown in figure 36(a). The tissue phantom is fixed in a cooled saline gel. From the photograph it can be seen that the light tissue region corresponds to the tumor and the darker tissue region corresponds to the normal tissue. The MAT-MI imaging experiment was performed under a permanent magnet based system and the circular scan consisted of 200 degrees view angle. The reconstructed conductivity image of the phantom can be seen in figure 36(b), and the average reconstructed conductivity of 0.71 and 0.35 S/m was obtained corresponding to the tumor and normal tissue regions. The experiment artifacts leads to

error in conductivity images, especially around the boundaries; however, the relative conductivities and structure of the tumor and normal tissue is reliably imaged.

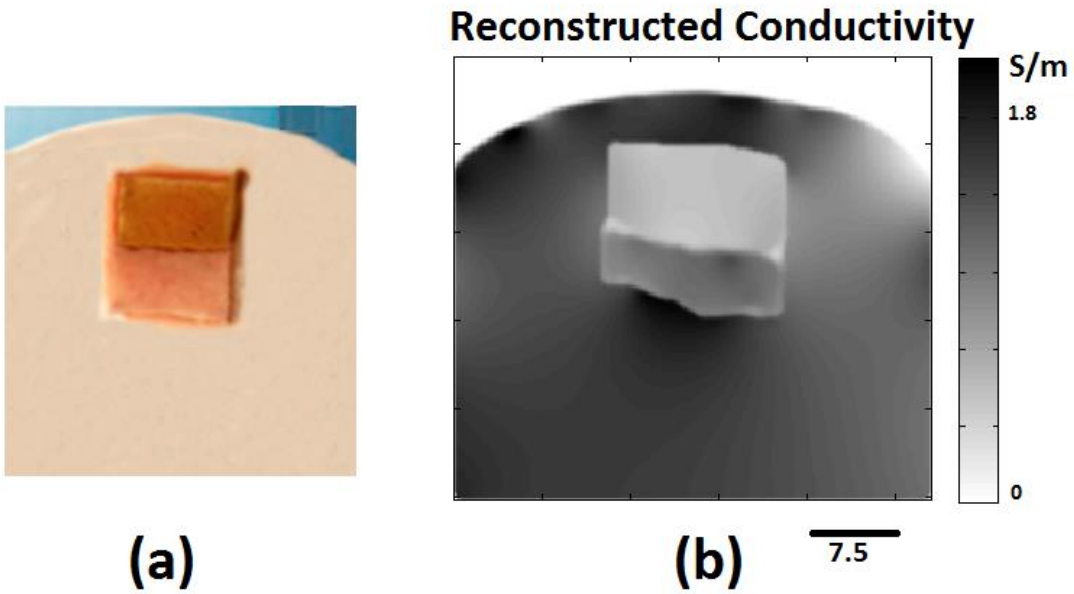

Fig. 36, (a) Photo of the imaged phantom, the darker tissue is normal tissue and the lighter tissue is cancer (b) reconstructed MAT-MI conductivity image

Further, we have imaged a phantom with a natural tumor and liver tissue structure as seen in figure 37. As the tissue structure is 2 mm in thickness direct conductivity measurement is not feasible with the needle electrodes used in our four electrode probe as the needle tip length (1.5–1.8 mm) was comparable to the sample thickness, which would generate inaccurate conductivity results. From the reconstruction in figure 37(b), the relative conductivities and structure corresponding to the tumor and liver tissue are reliably imaged. This allows to better distinguish the tumor from the normal tissue.

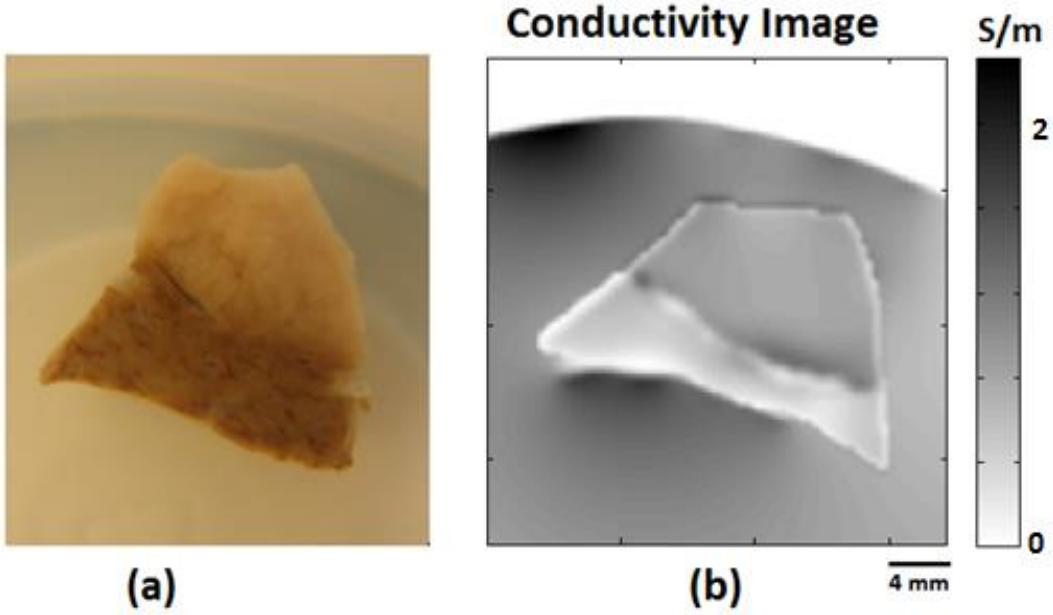

Fig. 37, (a) Photo of the imaged sample with naturally formed cancer-tissue interface (b) the reconstructed MAT-MI image

4.5 Discussion and conclusion

We have applied the vector beamformation algorithm to MAT-MI and from the reconstructed vector sources estimated the conductivity of the object. As seen in the computer simulations and phantom experiments, the conductivity value is reliably estimated in regions of uniform conductivity, and in regions around the boundaries with the current implementation of image reconstruction, the conductivity distribution is estimated by extrapolating the values from the surrounding uniform conductivity regions. In order to improve the accuracy of the reconstruction in regions of variable conductivity, the dependence of the vector source on conductivity gradient and the electric potential would have to be taken into account. The electric potential is a term that depends on the magnetic stimulation and the conductivity distribution of the object. A-priori knowledge

of this term is not possible for all objects, so an iterative reconstruction algorithm (Woo and Seo 2008) would have to be implemented. Conductivity anisotropy of biological tissue is another factor that would have to be taken into account for accurate imaging (Brinker and Roth 2008). In this case, a multi-excitation method (Seo *et al* 2004, Li and He 2010) can be used to estimate the directionally dependent components of conductivity.

The frequency bandwidth of the imaging system determines the spatial resolution of the reconstructed vector source distribution, and the spatial resolution can be estimated from the full width half maximum (FWHM) of the imaging system which determines the smallest size of the object that can be reliably imaged with system. At 500 kHz center frequency which is also the operating frequency of our current imaging system objects with size greater than 2 mm can be reliably imaged as seen in the imaging result.

In the simulation and experiment study, the objects imaged had a short uniform profile along the vertical Z direction. The applied magnetic fields and the spatial response of the ultrasound receiver were also uniform along the Z direction. To image under such simplified profiles a circular scanning aperture placed on the horizontal center plane is sufficient for the reconstruction of the cross section profile of the object. However, the proposed reconstruction algorithm can also be applied for 3D MAT-MI imaging using a 3D acoustic receiver aperture (Xia *et al* 2009). This setup can be used to image the distribution of MAT-MI vector sources in the object and the conductivity can then be estimated using the proposed method.

The acoustic homogeneity assumption used in the theoretical derivation in this study restricts the proposed imaging method to primarily soft tissue imaging. The acoustic heterogeneity of soft tissue is less than 10% and its effect can be considered to be negligible for MAT-MI (Xu and He 2005).

In this study, we have observed technical challenges when conducting MAT-MI experiments in an MRI system environment. The long coil cable (7 meter) with redundant capacitance and inductance will bring significant ringing and noise to the system due to the strong differential effects produced by $d\boldsymbol{B_1}/dt$ inducing eddy currents, and the energy loss in this cable is also not negligible, and the long cable for ultrasound detection picks up more environmental noise which pollutes the MAT-MI signals. In addition, the power line noise in MR center cannot be ignored and will be picked up by our MAT-MI hardware system, which may degrade the final image quality. So to fully realize the benefits of using a higher strength static magnetic field in MAT-MI, careful instrumentation would have to be developed to avoid these additional noise sources.

In conclusion, the results presented in this study indicate that the vector reconstruction algorithm with MAT-MI imaging experiments is able to distinguish the small electrical conductivity contrast in biological tissues with a spatial resolution at millimeter level.

Chapter 5

Conclusions and Future Work

5.1 Conclusions

Electrical conductivity imaging of biological tissue is under active research in recent years owing to studies indicating that electrical properties are indicators of underlying physiological and pathological conditions in biological tissue. In this dissertation, we have conducted research on magnetoacoustic tomography with magnetic induction which is a hybrid bioimpedance imaging method for high resolution imaging. Acoustic waves are generated in MAT-MI by use of magnetic fields which can readily be applied to underlying tissue and the ultrasound imaging used for the reconstruction results in high resolution.

The induced Lorentz force due to the magnetic fields gives rise to the acoustic source and in an object with variable conductivity this source is seen to be very strong at the conductivity boundaries where the Lorentz force changes rapidly from the change in conductivity. So, using the traditional ultrasound acoustic pressure source imaging the strong boundary sources can be reconstructed which reflect the structure of the underlying tissue. In MAT-MI a reliable imaging of the acoustic source distribution from the measured transducer signal is desired. Based on the forward modeling of the signal received at the transducer, two scanning setups with corresponding reconstruction algorithm is implemented for MAT-MI. To receive improved signal at the ultrasound transducer a shorter scanning radius with a larger transducer can be used. However, the electromagnetic interference (EMI) due to the pulsed magnetic field limits the shortness

of the scanning distance and the type of transducer. In order to obtain a reliable MAT-MI signal from tissue we have used a high power magnetic pulser and further developed a system to use the strong static magnetic field of a MRI system. With this system we are able to record the MAT-MI signals which reflect the tissue boundaries in a single transducer channel. Further, we have performed in-vivo experiments of hind limb tumors in a mouse model. The experiment reconstructions demonstrate that the tissue boundaries are imaged when reconstructing the acoustic source distribution in MAT-MI.

In order to reconstruct the complete conductivity distribution, using the available ultrasound imaging, we have used vector source reconstruction. The vector source field which is a component of the induced eddy current, unlike the boundary signal dominant scalar acoustic field is, uniformly present throughout the conductive object and such a field requires lesser frequency bandwidth to be reliably estimated. We have applied the reconstruction to MAT-MI simulation and phantom experiments with limited bandwidth acoustic measurement setup to test its performance. Further, we use numerical simulations to determine the point spread function (PSF) of the imaging system and measure the full width half maximum (FWHM) of the PSF, which is an estimation of the resolution in the image reconstruction. It is shown in these experiments that reliable conductivity estimation at high resolution, comparable to ultrasound setup, is possible with the proposed reconstruction method under limited bandwidth acoustic measurements and using a single magnetic excitation. This allows for practical implementation of the MAT-MI approach for human imaging applications for differentiation of tissue types based on conductivity distribution, which has potential application for cancer imaging.

5.2 Future Work

As seen from the promising results here MAT-MI is capable of high resolution biological tissue impedance imaging. However improvement to the implementation of the MAT-MI method is possible for improved applicability to human imaging. In our experiments we have used a single ultrasound transducer and mechanical rotation is used to obtain the various data used in the tomographic imaging. Instead ultrasound transducer arrays with multiple elements can be used for parallel data collection. In addition the use of averaging to improve the SNR with a slow repetition (≈7 Hz) high power magnetic pulser leads to slower imaging times. The current magnetic pulser design consists of a single coil supplied by a high power amplifier which leads to a high impedance load requiring large power to generate the magnetic fields. Instead coil arrays with smaller coils can be used to more efficiently generate similar fields as the larger coil. The magnetic excitation generated by the coil also induces significant electromagnetic interference (EMI) at the transducer. To reduce the effect of the EMI a stable coil driver with a short turn-off transient is desired. The transducer also need to have good EM shielding to suppress this interference and it is placed at a certain distance away from the imaging region of interest such that by the time the acoustic signal from this region arrives at the transducer the EMI fades away. To avoid the effect of EMI in MAT-MI an optical ultrasound transducer as proposed in (Wen *et al* 1998) can be used. Further, the current imaging systems operate at 500 kHz which gives a resolution of around 2mm and also limits the possible Z resolution with circular scan MAT-MI imaging. This can be

much improved with the use of higher imaging frequencies comparable to commercial ultrasound systems to better image complex tissue structures clearly.

The MAT-MI imaging using the strong static field of the MRI scanner gives good quality ultrasound signal. However, technical challenges exist when conducting MAT-MI experiments in a high field MRI system environment which may degrade the final image quality. So to fully realize the benefits of using a higher strength static magnetic field in MAT-MI, careful instrumentation would have to be developed to avoid these additional noise sources. Instead as MAT-MI does not require an uniform static field for imaging such strong magnetic fields can be generated by smaller superconducting magnets over the region of interest for human imaging. Conductivity anisotropy of biological tissue is another factor that would have to be taken into account for accurate imaging. In this case a multi-excitation method as proposed in (Seo *et al* 2004, Li and He 2010) can be used to estimate the directionally dependent components of conductivity. The acoustic homogeneity assumption used in the theoretical derivation restricts the proposed imaging method to primarily soft tissue imaging. The acoustic heterogeneity of soft tissue is less than 10 % and its effect can be considered to be negligible for MAT-MI (Xu and He 2005). However improved accuracy with MAT-MI is possible with accounting for these variations in biological tissue parameters.

Literature Cited

Ammari, H, Capdeboscq Y A ,Kang, H, Kozhemyak, A 2009 Mathematical models and reconstruction methods in magneto-acoustic imaging *Euro J. Appl. Math.* **20** 303–317

Awada, K A, Jackson, D R, Baumann, S B, Williams, J T, Wilton, D R, Fink, P W and Prasky, B R 1998 Effect of conductivity uncertainties and modeling errors on EEG source localization using a 2-D model *IEEE Trans. Biomed. Eng.* **45** 9 1135-45

Bache, R J, Harley A, Greenfield J C 1969 Evaluation of thoracic impedance plethysmography as an indicator of stroke volume in man *Am. J. Med. Sci.* **258** 8 100-13

Bagshaw, A P, Liston, A D, Bayford, R H, Tizzard, A, Gibson, A P, Tidswell, A T, Sparkes, M K, Dehghani, H, Binnie, C D and Holder, D S 2003 Electrical impedance tomography of human brain function using reconstruction algorithms based on the finite element method *Neuroimage* **20** 2 752-64

Baker, L E 1989 Principles of the impedance technique *IEEE Eng. Med. Biol.* **8** 1 11-5

Baker, L E and Geddes, L A 1970 The measurement of respiratory volumes in animals and man with use of electrical impedance *Annals of the New York Academy of Sciences* **170** 667–688

Barber, D C and Brown, B H 1984 Applied Potential Tomography *Journal of Physics E: Scientific Instruments,* **17**, 9, 723-33

Beetner, D G, Kapoor, S, Manjunath, S, Zhou, X and Stoecker, W V 2003 Differentiation among basal cell carcinoma, benign lesions, and normal skin using electric impedance *IEEE Trans. Biomed. Eng.* **50** 8 1020-5

Birgul, O, Eyuboglu, B M and Ider, Y Z 2003 Current constrained voltage scaled reconstruction (CCVSR) algorithm for MR-EIT and its performance with different probing current patterns *Phys. Med. Biol.* **48** 5 653-71

Birgul, O, Hamamura, M J, Muftuler, L T and Nalcioglu, O 2006 Contrast and spatial resolution in MREIT using low amplitude current *Phys. Med. Biol.* **51** 19 5035-49

Boverman, G, Kao, T J, Kulkarni, R, Kim, B S, Isaacson, D, Saulnier, G J and Newell, J C 2008 Robust linearized image reconstruction for multifrequency EIT of the breast *IEEE Trans. Med. Imaging* **27** 10 1439-48

Brinker, K and Roth, B J 2008 The effect of electrical anisotropy during magnetoacoustic tomography with magnetic induction *IEEE Trans. Biomed. Eng*. **55** 5 1637-9

Brown, B H 2003 Electrical impedance tomography (EIT): a review *J. Med. Eng. Technol.* **273** 97-108

Brown, B H, Barber, D C and Seagar, A D 1985 Applied potential tomography: possible clinical applications *Clin. Phys. Physiol. Meas.* **6** 2 109-21

Carter, H B 2004 Prostate cancers in men with low PSA levels — must we find them? *N. Engl. J. Med.* 350 22 2292-2294

Carter, C L, Allen, C, Hensen, D E 1989 Relation of tumor size, lymph node status, and survival in 24,740 breast cancer cases *Cancer* **63** 181-187

Cinca, J, Warren, M, Carreno, A, Tresanchez, M, Armadans, L, Gomez, P and SolerSoler, J 1997 Changes in myocardial electrical impedance induced by coronary artery occlusion in pigs with and without preconditioning: correlation with local ST segment potential and ventricular arrhythmias *Circulation* **96** 9 3079-86

Duck, F A 1990 *Physical Properties of Tissue* (London, U.K.: Academic)

Foster, K R and Schwan, H P 1989 Dielectric properties of tissues and biological materials: a critical review *Crit. Rev. Biomed. Eng.* **17** 1 25-104

Gabriel, C, Gabriel, S and Corthout, E 1996a The dielectric properties of biological tissues: I. Literature survey *Phys. Med. Biol.* **41** 11 2231-49

Gabriel, S, Lau, R W and Gabriel, C 1996b The dielectric properties of biological tissues: II. Measurements in the frequency range 10 Hz to 20GHz *Phys. Med. Biol.* **41** 11 2251-69

Gabriel, S, Lau, R W and Gabriel, C 1996c The dielectric properties of biological tissues: III. Parametric models for the dielectric spectrum of tissues *Phys. Med. Biol.* **41** 11 2271-93

Gao, N and He, B 2008 Noninvasive imaging of bioimpedance distribution by means of current reconstruction magnetic resonance electrical impedance tomography *IEEE Trans. Biomed. Eng.* **55** 5 1530-8

Geddes, L A and Baker, L E 1967 The specific resistance of biological material--a compendium of data for the biomedical engineer and physiologist *Med. Biol. Eng.* **5** 3 271-93

Gilad, O, Ghosh, A, Oh, D and Holder, D S 2009a A method for recording resistance changes non-invasively during neuronal depolarization with a view to imaging brain activity with electrical impedance tomography *J. Neurosci. Methods* **180** 1 87-96

Gilad, O, Horesh, L and Holder, D S 2009b A modelling study to inform specification and optimal electrode placement for imaging of neuronal depolarization during visual

evoked responses by electrical and magnetic detection impedance tomography *Physiol. Meas.* **30** 6 S201-24

Griffiths, H, Stewart, W R and Gough, W 1999 Magnetic induction tomography. A measuring system for biological tissues *Ann. N. Y. Acad. Sci.* **873** 335-45

Gursoy, D and Scharfetter, H 2009a Optimum receiver array design for magnetic induction tomography *IEEE Trans. Biomed. Eng.* **56** 5 1435-41

Gursoy, D and Scharfetter, H 2009b Reconstruction artefacts in magnetic induction tomography due to patient's movement during data acquisition *Physiol. Meas.* **30** 6 S165-74

Haemmerich, D, Schutt, D J, Wright, A W, Webster, J G and Mahvi, D M 2009 Electrical conductivity measurement of excised human metastatic liver tumours before and after thermal ablation *Physiol. Meas.* **30** 5 459-66

Haemmerich, D, Staelin, S T, Tsai, J Z, Tungjitkusolmun, S, Mahvi, D M and Webster, J G 2003 In vivo electrical conductivity of hepatic tumours *Physiol. Meas.* **24** 2 251-60

Haider, S, Hrbek, A and Xu, Y 2008 Magneto-acousto-electrical tomography: a potential method for imaging current density and electrical impedance *Physiol. Meas.* **29** 6 S41-50

Halter, R J, Schned, A, Heaney, J, Hartov, A and Paulsen, K D 2009 Electrical properties of prostatic tissues: I. Single frequency admittivity properties *J. Urol.* **182** 4 1600-7

Hamamura, M J and Muftuler, L T 2008 Fast imaging for magnetic resonance electrical impedance tomography *Magn. Reson. Imaging* **26** 6 739-45

Hamamura, M J, Muftuler, L T, Birgul, O and Nalcioglu, O 2006 Measurement of ion diffusion using magnetic resonance electrical impedance tomography *Phys. Med. Biol.* **51** 11 2753-62

Hampshire, A R, Smallwood, R H, Brown, B H and Primhak, R A 1995 Multifrequency and parametric EIT images of neonatal lungs *Physiol. Meas.* **16** 3 Suppl A A175-89

Hansen, P C 1994 Regularization Tools: A Matlab package for analysis and solution of discrete ill-posed problem *Numerical Algorithms* **6** 1-35

Hasanov, K F, Ma, A W, Nachman, A I and Joy, M L 2008 Current density impedance imaging *IEEE Trans. Med. Imaging* **27** 9 1301-9

Haueisen, J, Ramon, C, Eiselt, M, Brauer, H and Nowak, H 1997 Influence of tissue resistivities on neuromagnetic fields and electric potentials studied with a finite element model of the head *IEEE Trans. Biomed. Eng.* **44** 8 727-35

He, B 2005 High-resolution Functional Source and Impedance Imaging *Conf. Proc. IEEE Eng. Med. Biol. Soc.* **4** 4178-82

He, B ed 2004 *Modeling and Imaging of Bioelectrical Activity – Principles and Applications* (Kluwer Academic Publishers)

Holder, D S 2002 Editorial: Biomedical applications of electrical impedance tomography *Physiol. Meas.* **23** 1 3

Holder, D S, Rao, A and Hanquan, Y 1996 Imaging of physiologically evoked responses by electrical impedance tomography with cortical electrodes in the anaesthetized rabbit *Physiol. Meas.* **17 Suppl 4A** A179-86

Horoszewicz, J S, Leong, S S, Kawinski, E, Karr, J P, Rosenthal, H, Chu, T M, Mirand, E A and Murphy, G P 1983 LNCaP model of human prostatic carcinoma. *Cancer. Res.* **43** 4 1809–18.

Hu, G, Li, X and He, B 2010 Imaging biological tissues with electrical conductivity contrast below 1 S m-1 by means of magnetoacoustic tomography with magnetic induction *Apply. Phys. Lett.* **97** 103705

Hu, G, Cressman, E, He, B 2011 Magnetoacoustic imaging of human liver tumor with magnetic induction *Apply. Phys. Lett.* **98** 23703

Hu, G and He B 2011 Magnetoacoustic imaging of electrical conductivity of biological tissues with magnetic induction at a spatial resolution better than 2 mm *PLoS ONE* **6**, e23421

Ider, Y Z and Onart, S 2004 Algebraic reconstruction for 3D magnetic resonance electrical impedance tomography (MREIT) using one component of magnetic flux density *Physiol. Meas*. **25** 1 281-94

Ider, Y Z, Onart, S and Lionheart, W R 2003 Uniqueness and reconstruction in magnetic resonance-electrical impedance tomography (MR-EIT) *Physiol. Meas.* **24** 2 591-604

Islam, M R and Towe, B C 1988 Bioelectric current image reconstruction from magnetoacoustic measurements *IEEE Trans. Med. Imaging* **7** 4 386-91

Jensen, J A and Svendsen, N B 1992 Calculation of pressure fields from arbitrarily shaped, apodized, and excited ultrasound transducers *IEEE Trans UltrasonFerroelectrics and Freq Control* **3** 9 262-267

Jeon, K, Minhas, A S, Kim, Y T, Jeong, W C, Kim, H J, Kang, B T, Park, H M, Lee, C O, Seo, J K and Woo, E J 2009 MREIT conductivity imaging of the postmortem canine abdomen using CoReHA *Physiol. Meas.* **30** 9 957-66

Jin, J M ed 2002 *The Finite Element Method in Electromagnetics* (New York: Wiley)

Jorgenson, D B, Schimpf, P H, Shen, I, Johnson, G, Bardy, G H, Haynor, D R and Kim, Y 1995 Predicting cardiothoracic voltages during high energy shocks: methodology and comparison of experimental to finite element model data *IEEE Trans. Biomed. Eng.* **42** 6 559-71

Joseph, D D 2006 Helmholtz decomposition coupling rotational to irrotational flow of a viscous fluid *Proceedings of the National Academy of Sciences of the United States of* America **10** 3 14272-7

Jossinet, J 1998 The impedivity of freshly excised human breast tissue *Physiol. Meas.* **19** 1 61-75

Jossinet, J 1996 Variability of impedivity in normal and pathological breast tissue *Med. Biol. Eng. Comput.* **34** 5 346-50

Jossinet, J, Marry, E and Matias, A 2002 Electrical impedance endotomography *Phys. Med. Biol.* **47** 13 2189-202

Jossinet, J and Schmitt, M 1999 A review of parameters for the bioelectrical characterization of breast tissue *Ann. N. Y. Acad. Sci.* **873** 30-41

Joy, M, Scott, G and Henkelman, M 1989 In vivo detection of applied electric currents by magnetic resonance imaging *Magn. Reson. Imaging* **7** 1 89-94

Joy, M L, Lebedev, V P and Gati, J S 1999 Imaging of current density and current pathways in rabbit brain during transcranial electrostimulation *IEEE Trans. Biomed. Eng.* **46** 9 1139-49

Karbeyaz, B U and Gencer, N G 2003 Electrical conductivity imaging via contactless measurements: an experimental study *IEEE Trans. Med. Imaging* **22** 5 627-35

Katscher, U, Voigt, T and Findeklee, C 2009a Electrical conductivity imaging using magnetic resonance tomography *Conf. Proc. IEEE Eng. Med. Biol. Soc.* **2009** 3162-4

Katscher, U, Voigt, T, Findeklee, C, Vernickel, P, Nehrke, K and Dossel, O 2009b Determination of electric conductivity and local SAR via B1 mapping *IEEE Trans. Med. Imaging* **28** 9 1365-74

Kerne, T E, Hartov, A, Soho, S K, Poplack, S P and Paulsen, K D 2002 Imaging the breast with EIS: an initial study of exam consistency *Physiol. Meas.* **23** 1 221-36

Kerner, T E, Paulsen, K D, Hartov, A, Soho, S K and Poplack, S P 2002 Electrical impedance spectroscopy of the breast: clinical imaging results in 26 subjects *IEEE Trans. Med. Imaging* **21** 6 638-45

Khang, H S, Lee, B I, Oh, S H, Woo, E J, Lee, S Y, Cho, M H, Kwon, O, Yoon, J R and Seo, J K 2002 J-substitution algorithm in magnetic resonance electrical impedance tomography (MREIT): phantom experiments for static resistivity images *IEEE Trans. Med. Imaging* **21** 6 695-702

Kim, H J, Kim, Y T, Minhas, A S, Jeong, W C, Woo, EJ, Seo, J K and Kwon, O J 2009 In vivo high-resolution conductivity imaging of the human leg using MREIT: the first human experiment *IEEE Trans. Med. Imaging* **28** 11 1681-7

Kim, H J, Lee, B I, Cho, Y, Kim, Y T, Kang, B T, Park, H M, Lee, S Y, Seo, J K and Woo, E J 2007 Conductivity imaging of canine brain using a 3 T MREIT system: postmortem experiments *Physiol. Meas.* **28** 11 1341-53

Klepfer, R N, Johnson, C R and Macleod, R S 1997 The effects of inhomogeneities and anisotropies on electrocardiographic fields: a 3-D finite-element study *IEEE Trans. Biomed. Eng*. **44** 8 706-19

Klivington, K A and Galambos, R 1968 Rapid resistance shifts in cat cortex during click evoked responses *J. Neurophysiol.* **31** 4 565-73

Klivington, K A and Galambos, R 1967 Resistance shifts accompanying the evoked cortical response in the cat *Science* **157** 3785 211-3

Korjenevsky, A, Cherepenin, V and Sapetsky, S 2000 Magnetic induction tomography: experimental realization *Physiol. Meas.* **21** 1 89-94

Kubicek, W G, From, A H, Patterson, R P, Witsoe, D A, Castaneda, A, Lillehei, R C and Ersek, R 1970 Impedance cardiography as a noninvasive means to monitor cardiac function *J. Assoc. Adv. Med. Instrum.* **4** 2 79-84

Kwon, O, Woo, E J, Yoon, J R and Seo, J K 2002 Magnetic resonance electrical impedance tomography (MREIT): simulation study of J-substitution algorithm *IEEE Trans. Biomed. Eng.* **49** 2 160-7

Kwon, O I, Lee, B I, Nam, H S and Park, C 2007 Noise analysis and MR pulse sequence optimization in MREIT using an injected current nonlinear encoding (ICNE) method *Physiol. Meas.* **28** 11 1391-404

Lai, Y, Van Drongelen, W, Ding, L, Hecox, K E, Towle, V L, Frim, D M and He, B 2005 Estimation of in vivo human brain-to-skull conductivity ratio from simultaneous extra- and intra-cranial electrical potential recordings *Clin. Neurophysiol.* **116** 2 456-65

Lee, B I, Oh, S H, Woo, E J, Lee, S Y, Cho, M H, Kwon, O, Seo, J K, Lee, J Y and Baek, W S 2003 Three-dimensional forward solver and its performance analysis for magnetic resonance electrical impedance tomography (MREIT) using recessed electrodes *Phys. Med. Biol.* 48 **13** 1971-86

Lee, B 1999 Bioimpedance: novel use of a minimally invasive technique for cancer localization in the intact prostate *Prostate* **39** 213-8

Lee, B I, Park, C, Pyo, H C, Kwon, O and Woo, E J 2007 Optimization of current injection pulse width in MREIT *Physiol. Meas.* **28** 1 N1-7

Lee, S H, Seo, J K, Park, C, Lee, B I, Woo, E J, Lee, S Y, Kwon, O and Hahn, J 2006 Conductivity image reconstruction from defective data in MREIT: numerical simulation and animal experiment *IEEE Trans. Med. Imaging* **25** 2 168-76

Li, X and He, B 2010a Multi-excitation magnetoacoustic tomography with magnetic induction (MAT-MI) *J. Phys.: Conf. Ser.* **224** 012035

Li, X and He, B 2010b Multi-Excitation Magnetoacoustic Tomography with Magnetic Induction for Bioimpedance Imaging *IEEE Transactions on Medical Imaging* in press

Li, X and He, B 2009 Magnetoacoustic tomography with magnetic induction (MAT-MI) for electrical conductivity imaging *Conf. Proc. IEEE Eng. Med. Biol. Soc.* **2009** 3173-6

Li, X, Li, X, Zhu, S and He, B 2009 Solving the forward problem of magnetoacoustic tomography with magnetic induction by means of the finite element method *Phys. Med. Biol.* **54** 9 2667-82

Li, X, Mariappan, L and He, B 2010 Three-dimensional Multi-Excitation Magnetoacoustic Tomography with Magnetic Induction *J. Appl. Phys.* submitted

Li, X, Xia, R and He, B 2008 Acoustic vector tomography and its application to magnetoacoustic tomography with magnetic induction (MAT-MI) *Conf. Proc. IEEE Eng. Med. Biol. Soc.* **2008** 5834-6

Li, X, Xu, Y and He, B 2007 Imaging electrical impedance from acoustic measurements by means of magnetoacoustic tomography with magnetic induction (MAT-MI) *IEEE Trans. Biomed. Eng.* **54** 2 323-30

Li, X, Xu, Y and He, B 2006 Magnetoacoustic tomography with magnetic induction for imaging electrical impedance of biological tissue *J. Appl. Phys.* **99** 066112

Liao, C K, Li, M L and Li, P C 2004 Optoacoustic imaging with synthetic aperture focusing and coherence weighting *Opt. Lett*. **29** 2506–8

Ma, Q and He, B 2007 Investigation on magnetoacoustic signal generation with magnetic induction and its application to electrical conductivity reconstruction *Phys. Med. Biol.* **52** 16 5085-99

Mariappan, L, Li, X and He, B 2011 B-scan based acoustic source reconstruction for magnetoacoustic tomography with magnetic induction (MAT-MI) *IEEE Trans. Biomed. Eng.* **5** 8 713-20

Mariappan, L and He, B 2013 Magneto acoustic tomography with magnetic induction: bioimpedance reconstruction through vector source imaging *IEEE Trans. Med. Imaging* **3** 2 619-27

Malmivuo, J and Plonsey, R ed 1995 *Bioelectromagnetism* (New York: Oxford University Press)

McEwan, A, Romsauerova, A, Yerworth, R, Horesh, L, Bayford, R and Holder, D S 2006 Design and calibration of a compact multi-frequency EIT system for acute stroke imaging *Physiol. Meas.* **27** 5 S199-210

Meaney, P M, Fanning, M W, Li, D, Poplack, S P and Paulsen, K D 2000 A clinical prototype for active microwave imaging of the breast *IEEE Trans. Microwave Theory Tech.* **48** 11 1841-53

Merwa, R, Hollaus, K, Brunner, P and Scharfetter, H 2005 Solution of the inverse problem of magnetic induction tomography (MIT) *Physiol. Meas.* **26** 2 S241-50

Metherall, P, Barber, D C, Smallwood, R H and Brown, B H 1996 Three-dimensional electrical impedance tomography *Nature* **380** 6574 509-12

Mishra, V, Bouayad, H, Schned, A, Heaney, J and Halter, R J 2012 Electrical impedance spectroscopy for prostate cancer diagnosis *Conf. Proc. IEEE Eng. Med. Biol. Soc.* 3258-61

Montalibet, A, Jossinet, J and Matias, A 2001a Scanning electric conductivity gradients with ultrasonically-induced Lorentz force *Ultrason. Imaging* **23** 2 117-32

Montalibet, A, Jossinet, J, Matias, A and Cathignol, D 2001b Electric current generated by ultrasonically induced Lorentz force in biological media *Med. Biol. Eng. Comput.* **39** 1 15-20

Morimoto, T, Kinouchi, Y, Iritani, T, Kimura, S, Konishi, Y, Mitsuyama, N, Komaki, K and Monden, Y 1990 Measurement of the electrical bio-impedance of breast tumors *Eur. Surg. Res.* **22** 2 86-92

Morse, P M and Ingard, K U ed 1968 *Theoretical Acoustics* (New York: McGraw-Hill)

Muftuler, L T, Chen, G, Hamamura, M J and Ha, S H 2009 MREIT with SENSE acceleration using a dedicated RF coil design *Physiol. Meas.* **30** 9 913-29

Muftuler, L T, Hamamura, M, Birgul, O and Nalcioglu, O 2004 Resolution and contrast in magnetic resonance electrical impedance tomography (MREIT) and its application to cancer imaging *Technol. Cancer. Res. Treat.* **3** 6 599-609

Muftuler, L T, Hamamura, M J, Birgul, O and Nalcioglu, O 2006 In vivo MRI electrical impedance tomography (MREIT) of tumors *Technol. Cancer. Res. Treat*. **5** 4 381-7

Nam, H S and Kwon, O I 2010 Axial anisotropic conductivity imaging based on projected current density in MREIT *IEEE Trans. Med. Imaging* **29** 3 781-9

Nam, H S, Park, C and Kwon, O I 2008 Non-iterative conductivity reconstruction algorithm using projected current density in MREIT *Phys. Med. Biol.* **53** 23 6947-61

Norton, S J and Linzer, M 1981 Ultrasonic reflectivity imaging in three dimensions: exact inverse scattering solutions for plane, cylindrical, and spherical apertures *IEEE Trans. Biomed. Eng.* **28** 2 202-20

Oh, S H, Han, J Y, Lee, S Y, Cho, M H, Lee, B I and Woo, E J 2003 Electrical conductivity imaging by magnetic resonance electrical impedance tomography (MREIT) *Magn. Reson. Med.* **50** 4 875-8

Oh, S H, Lee, B I, Park, T S, Lee, S Y, Woo, E J, Cho, M H, Seo, J K and Kwon, O 2004 Magnetic resonance electrical impedance tomography at 3 Tesla field strength *Magn. Reson. Med*. **51** 6 1292-6

Oh, S H, Lee, B I, Woo, E J, Lee, S Y, Cho, M H, Kwon, O and Seo, J K 2003 Conductivity and current density image reconstruction using harmonic Bz algorithm in magnetic resonance electrical impedance tomography *Phys. Med. Biol.* **48** 19 3101-16

Oh, S H, Lee, B I, Woo, E J, Lee, S Y, Kim, T S, Kwon, O and Seo, J K 2005 Electrical conductivity images of biological tissue phantoms in MREIT *Physiol. Meas.* **26** 2 S279-88

Pan, X, Zou, Y and Anastasio, M A 2003 Data redundancy and reduced-scan reconstruction in reflectivity tomography *IEEE Trans. Image Process.* **12** 7 784-95

Park, C, Lee, B I, Kwon, O and Woo, E J 2007 Measurement of induced magnetic flux density using injection current nonlinear encoding (ICNE) in MREIT *Physiol. Meas.* **28** 2 117-27

Park, C, Park, E J, Woo, E J, Kwon, O and Seo, J K 2004 Static conductivity imaging using variational gradient Bz algorithm in magnetic resonance electrical impedance tomography *Physiol. Meas*. **25** 1 257-69

Patriciu, A, Yoshida, K, Struijk, J J, DeMonte, T P, Joy, M L and Stodkilde-Jorgensen, H 2005 Current density imaging and electrically induced skin burns under surface electrodes *IEEE Trans. Biomed. Eng.* **52** 12 2024-31

Paulson, K S, Pidcock, M K and McLeod, C N 2004 A probe for organ impedance measurement *IEEE Trans. Biomed. Eng.* **51** 10 1838-44

Ranganathan, K and Walker, W F 2003 A novel beamformer design method for medical ultrasound. Part I: Theory *IEEE Transactions on Ultrasonics, Ferroelectrics and FreqControl* **50** 15-24

Roth, B J 2011 The role of magnetic forces in biology and medicine *Exp. Biol. Med.* **23** 6 132-7

Roth, J, Basser, P J, Wikswo Jr, J P 1994 A theoretical model for magneto-acoustic imaging of bioelectric currents *IEEE Trans. Biomed. Eng.* **41** 8 723-8

Rush, S and Driscoll, D A 1968 Current distribution in the brain from surface electrodes *Anesth. Analg.* **47** 6 717-23

Sadleir, R, Grant, S, Zhang, S U, Oh, S H, Lee, B and Woo, E J 2006 High field MREIT: setup and tissue phantom imaging at 11 T *Physiol. Meas.* **27** 5 S261-70

Sadleir, R J, Vannorsdall, T D, Schretlen, D J and Gordon, B 2010 Transcranial direct current stimulation (TDCS) in a realistic head model *Neuroimage* **51** 4 1310-8

Scharfetter, H, Lackner, H K and Rosell, J 2001 Magnetic induction tomography: hardware for multi-frequency measurements in biological tissues *Physiol. Meas.* **22** 1 131-46

Scharfetter, H, Merwa, R and Pilz, K 2005 A new type of gradiometer for the receiving circuit of magnetic induction tomography (MIT) *Physiol. Meas*. **26** 2 S307-18

Schwan, H P 1992 Linear and nonlinear electrode polarization and biological materials *Ann. Biomed. Eng.* **20** 3 269-88

Schwan, H P ed 1963 *Determination of Biological Tissues, Physical Techniques in Biological Research* (New York: Academic)

Scott, G C, Joy, M G, Armstrong, R L and Henkelman, R M 1995 Electromagnetic considerations for RF current density imaging [MRI technique] *IEEE Trans. Med. Imaging* **14** 3 515-24

Scott, G C, Joy, M G, Armstrong, R L and Henkelman, R M 1991 Measurement of nonuniform current density by magnetic resonance *IEEE Trans. Med. Imaging* **10** 3 362-74

Scott, G C, Joy, M L, Armstrong, R L and Henkelman, R M 1995 Rotating frame RF current density imaging *Magn. Reson. Med.* **33** 3 355-69

Scott, G C, Joy, M L, Armstrong, R L and Henkelman, R M 1992 RF current density imaging in homogeneous media *Magn. Reson. Med.* **28** 2 186-201

Seo, J K, Kim, S W, Kim, S, Liu, J J, Woo, E J, Jeon, K and Lee, C O 2008 Local harmonic B(z) algorithm with domain decomposition in MREIT: computer simulation study *IEEE Trans. Med. Imaging* **27** 12 1754-61

Seo, J K, Yoon, J R, Woo, E J and Kwon, O 2003 Reconstruction of conductivity and current density images using only one component of magnetic field measurements *IEEE Trans. Biomed. Eng.* **50** 9 1121-4

Solazzo, S A, Liu, Z, Lobo, S M, Ahmed, M, Hines-Peralta, A U, Lenkinski, R E and Goldberg, S N 2005 Radiofrequency ablation: importance of background tissue electrical conductivity--an agar phantom and computer modeling study *Radiology* **236** 2 495-502

Sun, X, Zhang, F, Ma, Q, Tu, J and Zhang D 2012 Acoustic dipole radiation based conductivity image reconstruction for magnetoacoustic tomography with magnetic induction *Appl. Phys. Lett.* **100** 024105

Sun, X, Fang, D, Zhang, D and Ma, Q 2013 Acoustic dipole radiation based electrical impedance contrast imaging approach of magnetoacoustic tomography with magnetic induction *Med. Phys.* **40** 052902

Surowiec, A J, Stuchly, S S, Barr, J B and Swarup, A 1988 Dielectric properties of breast carcinoma and the surrounding tissues *IEEE Trans. Biomed. Eng.* **35** 4 257-63

Tidswell, T, Gibson, A, Bayford, R H and Holder, D S 2001 Three-dimensional electrical impedance tomography of human brain activity *Neuroimage* **13** 2 283-94

Towe, B C and Islam, M R 1988 A magneto-acoustic method for the noninvasive measurement of bioelectric currents *IEEE Trans. Biomed. Eng.* **35** 10 892-4

Tsai, J Z, Cao, H, Tungjitkusolmun, S, Woo, E J, Vorperian, V R and Webster, J G 2000 Dependence of apparent resistance of four-electrodeprobes on insertion depth *IEEE Trans. Biomed. Eng.* **47** 1 41-8

Vaughan, T, DelaBarre, L, Snyder, C, Tian, J, Akgun, C, Shrivastava, D, Liu, W, Olson, C, Adrianv, G, Strupp, J, Andersen, P, Gopinath, A, Moortele, P, Garwood, M and Ugurbil, K 2006 9.4T human MRI: preliminary results *Magn. Reson. Med.* **5** 6 1274-82

Wan, Y and Ebbini, E S 2009 A post-beamforming 2-D pseudoinverse filter for coarsely sampled ultrasound arrays IEEE Transactions Ultrasonics, Ferroelectrics, FreqControl **56** 1888-902

Wang, D, DeMonte, T P, Ma, W, Joy, M L and Nachman, A I 2009 Multislice radiofrequency current density imaging *IEEE Trans. Med. Imaging* **28** 7 1083-92

Wang, W and Eisenberg, S R 1994 A three-dimensional finite element method for computing magnetically induced currents in tissues *Magnetics, IEEE Transactions on* **30** 6 5015-23

Wang, X, Pang, Y, Ku, G, Xie, X, Stoica, G and Wang, L V 2003 Noninvasive laser-induced photoacoustic tomography for structural and functional in vivo imaging of the brain *Nat. Biotechnol*. **21** 7 803-6

Watson, S, Morris, A, Williams, R J, Griffiths, H and Gough, W 2004 A primary field compensation scheme for planar array magnetic induction tomography *Physiol. Meas*. **25** 1 271-9

Wen, H 2000 Feasibility of biomedical applications of Hall effect imaging *Ultrason. Imaging* **22** 2 123-36

Wen, H 1999 Volumetric Hall effect tomography--a feasibility study *Ultrason. Imaging* **21** 3 186-200

Wen, H, Shah, J and Balaban, R S 1998a Hall effect imaging *IEEE Trans. Biomed. Eng.* **45** 1 119-24

Wen, H, Wiesler, D G, Tveten, A, Danver, B and Dandridge, A 1998b High sensitivity fiber optic ultrasound sensors for medical imaging applications *Ultrason. Imag*. **20** 102-112

Woo, E J, Hua, P, Webster, J G and Tompkins, W J 1992 Measuring lung resistivity using electrical impedance tomography *IEEE Trans. Biomed. Eng*. 7 756-60

Woo, E J and Seo, J K 2008 Magnetic resonance electrical impedance tomography (MREIT) for high-resolution conductivity imaging *Physiol. Meas*. **29** 10 R1-26

Xia, R, Li, X and He, B 2010 Comparison study of three different image reconstruction algorithms for MAT-MI *IEEE Trans. Biomed. Eng.* **57** 3 708-13

Xia, R, Li, X and He, B 2009 Reconstruction of vectorial acoustic sources in time domain tomography *IEEE Trans. Med. Imaging* **28** 5 669-75

Xia, R, Li, X and He, B 2007 Magnetoacoustic tomographic imaging of electrical impedance with magnetic induction *Appl. Phys. Lett*. **91** 8 83903

Xu, M and Wang, L V 2002 Time-domain reconstruction for thermoacoustic tomography in a spherical geometry *IEEE Trans. Med. Imaging* **21** 7 814-22

Xu, M, Xu, Y and Wang, L V 2003 Time-domain reconstruction algorithms and numerical simulations for thermoacoustic tomography in various geometries *IEEE Trans. Biomed. Eng*. **50** 9 1086-99

Xu, M and Wang, L H 2002 Pulsed-microwave-induced termoacoustictomography: filtered backprojection in a circular measurement configuration *Med. Phys*. **29** 1661-9

Xu, Y and He, B 2005 Magnetoacoustic tomography with magnetic induction (MAT-MI) Phys. Med. Biol. **50** 21 5175-87

Xu, Y and Wang, L V 2004 Time reversal and its application to tomography with diffracting sources *Phys. Rev. Lett*. **92** 3 033902

Xu, Y and Wang, L V 2003 Effects of acoustic heterogeneity in breast thermoacoustic tomography *IEEE Trans. Ultrason. Ferroelectr. Freq. Control* **50** 9 1134-46

Yang, Q X, Wang, J, Zhang, X, Collins, C M, Smith, M B, Liu, H, Zhu, X H, Vaughan, J T, Ugurbil, K and Chen, W 2002 Analysis of wave behavior in lossy dielectric samples at high field *Magn. Reson. Med*. **47** 5 982-9

Yerworth, R J, Bayford, R H, Brown, B, Milnes, P, Conway, M and Holder, D S 2003 Electrical impedance tomography spectroscopy (EITS) for human head imaging *Physiol. Meas*. **24** 2 477-89

Zastrow, E, Davis, S K, Lazebnik, M, Kelcz, F, Van Veen, B D and Hagness, S C 2008 Development of anatomically realistic numerical breast phantoms with accurate dielectric properties for modeling microwave interactions with the human breast *IEEE Trans. Biomed. Eng.* **55** 12 2792-800

Zhang, X, Zhu, S and He, B 2010 Imaging electric properties of biological tissues by RF field mapping in MRI *IEEE Trans. Med. Imaging* **29** 2 474-81

Zhang, X, Schmitter, S, Van de Moortele, P F, Liu, J and Hee, B 2013 From complex B_1mapping to local SAR estimation or human brain MR imaging using multi-channel transceiver coil at 7T *IEEE Trans. Med. Imaging* **32** 1058-62

Zhang, Y, Van Drongelen, W and He, B 2006 Estimation of in vivo brain-to-skull conductivity ratio in humans *Appl. Phys. Lett*. **89** 22 223903

Zhou, L, Li, X, Zhu, S and He, B 2011 Magnetoacoustic tomography with magnetic induction (MAT-MI) for breast tumor imaging: numerical modeling and simulation *Phy. Med. Biol.* **56** 7 1967-1983

Zolgharni, M, Ledger, P D, Armitage, D W, Holder, DS and Griffiths, H 2009a Imaging cerebral haemorrhage with magnetic induction tomography: numerical modelling *Physiol. Meas.* **30** 6 S187-200

Zolgharni, M, Ledger, P D and Griffiths, H 2009b Forward modelling of magnetic induction tomography: a sensitivity study for detecting haemorrhagic cerebral stroke *Med. Biol. Eng. Comput*. **47** 12 1301-13

Zou, Y and Guo, Z 2003 A review of electrical impedance techniques for breast cancer detection *Med. Eng. Phys*. **25** 2 79-90